

Doctoral theses at NTNU, 2022:109

Inger-Emma Nylund

Transmission electron microscopy of ferroic materials

ISBN 978-82-326-6617-1 (printed ver.)
ISBN 978-82-326-6720-8 (electronic ver.)
ISSN 1503-8181 (printed ver.)
ISSN 2703-8084 (electronic ver.)

Doctoral theses at NTNU, 2022:109

NTNU
Norwegian University of
Science and Technology
Thesis for the degree of
Philosophiae Doctor



Inger-Emma Nylund

Transmission electron microscopy of ferroic materials

Thesis for the degree of Philosophiae Doctor

Trondheim, April 2022

Norwegian University of Science and Technology



Norwegian University of
Science and Technology

NTNU
Norwegian University of Science and Technology

Thesis for the degree of Philosophiae Doctor

© Inger-Emma Nylund

ISBN 978-82-326-6617-1 (printed ver.)
ISBN 978-82-326-6720-8 (electronic ver.)
ISSN 1503-8181 (printed ver.)
ISSN 2703-8084 (electronic ver.)

Doctoral theses at NTNU, 2022:109



Printed by Skipnes Kommunikasjon AS

Summary

Materials science has the last few decades been advancing by an increasing insight in structure and local chemical composition at the sub-nanometre scale. In this context, the transmission electron microscope (TEM) has proved to be an indispensable tool due to its spatial resolving powers. Using electrons, rather than X-rays, to study ferroelectric materials also has the advantage of the strong interaction between the electrons and matter, which can reveal the presence of a non-centrosymmetric crystal structure, a prerequisite for ferroelectric properties. In this thesis work, three structurally complex ferroelectric materials were studied by TEM, taking advantage of the possibility to perform imaging, diffraction, and spectroscopy within the same instrument.

A thorough investigation of BaTiO₃ films deposited on (100), (110), and (111) oriented SrTiO₃ substrates constituted the first part of the thesis. This material is one of the most important ferroelectric materials used in electronics due to its excellent dielectric properties. It was demonstrated by selected area diffraction that the films grow with an epitaxial relationship to the single crystalline substrates. The films were relaxed by formation of misfit dislocations at the interface during growth, and tensile strain was introduced in the films due to the difference in thermal expansion coefficient between the film and the substrate. The Burgers vectors for the misfit dislocations at the interface were determined to be $a\langle 010 \rangle$, $a[1\bar{1}0]$ and $a[001]$, and $a\langle 110 \rangle$, for the (100), (110), and (111) films, respectively. Lastly, the abruptness of the substrate-film interface and the internal chemical homogeneity of the films were studied using electron energy-loss spectroscopy. The interdiffusion distance of Sr and Ba at the interface was determined to be 3.4, 5.3, and 5.3 nm for the (100), (110), and (111) oriented films, respectively. The films were deposited in a layered fashion, and the boundary between each layer was observed to be Ba-deficient.

The second class of materials in this study is known as tetragonal tungsten bronzes (TTB) with the general chemical formula $A_1A_2A_4C_4B_{10}O_{30}$, which allows for a magnitude of different chemical compositions with tailored functional properties.

TTBs are known to exhibit either normal or relaxor ferroelectricity, and some are used as high temperature piezoelectrics due to their high Curie temperature. Two different series of oxide TTBs were studied in this work, where cation substitution on the *A*-site was explored. Firstly, $A_4\text{Bi}_2\text{Nb}_{10}\text{O}_{30}$, $A=\text{Na}, \text{K}, \text{Rb}$ was investigated. The crystal symmetry of the two compounds $\text{K}_4\text{Bi}_2\text{Nb}_{10}\text{O}_{30}$ and $\text{Rb}_4\text{Bi}_2\text{Nb}_{10}\text{O}_{30}$ were determined via convergent-beam electron diffraction (CBED) to belong to the centrosymmetric $P4/mbm$ space group. Possible reasons for the lack of a ferroelectric phase transition for these TTBs and the role of the Bi^{3+} lone pair cation in tungsten bronzes were discussed. Secondly, a systematic study on cation intermixing between the *A1*- and *A2*-site in the series $\text{Ba}_4M_2\text{Nb}_{10}\text{O}_{30}$, $M=\text{Na}, \text{K}, \text{Rb}$ was performed by simultaneous scanning TEM (STEM) and energy-dispersive X-ray spectroscopy. Combined with X-ray diffraction (XRD) data, it was determined that a large degree of intermixing was present in $\text{Ba}_4\text{K}_2\text{Nb}_{10}\text{O}_{30}$, and that $\text{Ba}_4\text{Na}_2\text{Nb}_{10}\text{O}_{30}$ and $\text{Ba}_4\text{Rb}_2\text{Nb}_{10}\text{O}_{30}$ displayed a large degree of order or partial order with respect to occupancy on the *A1*- and *A2*-sites. This was explained by the different ionic radii of Na^+ , K^+ , and Rb^+ compared to Ba^{2+} , where Na^+ is much smaller, K^+ is of equal size, and Rb^+ is bigger than Ba^{2+} .

Investigation of the improper ferroelectric and orthorhombic $\text{Gd}_2(\text{MoO}_4)_3$ by STEM and XRD is presented in the third part of the thesis. High-quality atomically resolved images were obtained for single crystalline $\text{Gd}_2(\text{MoO}_4)_3$, but it was not possible to determine the polarization orientation of the ferroelectric domains in the material from the atomically resolved images. Furthermore, specimens for *in situ* biasing in the TEM were successfully prepared by focused ion beam. Yet, the biasing experiment turned out to be challenging because of increasing conductivity of the material during the experiment, in addition to interference by the ferroelastic properties. Finally, to get further insight in the crystal structure of $\text{Gd}_2(\text{MoO}_4)_3$, a temperature dependent XRD study from ambient to above the ferroelectric phase transition was carried out. The transition from the orthorhombic ferroelectric phase to the tetragonal paraelectric phase was observed. The ferroelastic strain was calculated based on the thermal evolution of the lattice parameters. Rietveld refinement of the temperature dependent data revealed that the displacement of cations followed different critical behavior, providing new insight into the structural changes that drive the improper ferroelectricity in $\text{Gd}_2(\text{MoO}_4)_3$.

The work presented in this thesis has demonstrated that the TEM is a very useful tool in the study of ferroic materials. Local variation in the structure and chemistry at an atomic scale were investigated in oxide films as well as

bulk materials, which would have been difficult to obtain by other experimental techniques. Determination of the centrosymmetric crystal symmetry of two compounds, previously not determined, was also demonstrated by CBED. However, when the structural variations between two domains became miniature, on the order of picometers, or when specimen damage occurred by the incident high-energy electron beam, alternative characterization techniques, such as XRD provided useful information. Furthermore, TEM complemented by XRD and electrical measurements were required to fully investigate different properties of the TTBs, demonstrating an important feature of modern materials science, that a combination of experimental techniques is essential in order to advance the field.

Preface

This thesis has been submitted to the Norwegian University of Science and Technology (NTNU) in partial fulfilment of the requirements for the degree of *Philosophiae Doctor*. The work presented in this thesis was performed in the Functional Materials and Materials Chemistry (FACET) research group at the Department of Materials Science and Engineering (IMA), NTNU, from April 2018 to April 2022. The work was supervised by Prof. Tor Grande (IMA), and co-supervised by Assoc. Prof. Per Erik Vullum (Department of Physics) and Prof. Mari-Ann Einarsrud (IMA). The work was funded by the Research Council of Norway (RCN) through the BORNIT project, grant number 275139, which was originally initiated by Dr. Maria Benelmekki as main supervisor, focusing on boron nitride thin films grown by pulsed laser deposition for advanced bio-applications. However, Maria Benelmekki left NTNU during the summer of 2018, and since she was the main expert on PLD, the project changed to accommodate the expertise present at NTNU. Tor Grande took over as main supervisor August 15th 2018. The main part of the experimental work was performed on transmission electron microscopes accessed through the *TEM Gemini Centre* at NTNU. The TEM Gemini Centre is part of the national infrastructure *Norwegian Centre for TEM* (NORTEM) which was funded by the RCN under grant number 197405. Furthermore, access to focused ion beam and additional instrumentation were provided by *NTNU NanoLab* which is part of the *Norwegian Micro- and Nano-Fabrication Facility* (NorFab), also funded by RCN through grant number 295864.

The author is the main contributor to the work presented in this thesis. Contributions from others include preparation of the studied materials. Dr. Trygve Magnus Ræder (IMA, now Department of Physics, DTU) prepared the BaTiO₃ films on the SrTiO₃ substrates, M.Sc. Caren Regine Zeiger (IMA) synthesized the bismuth containing tetragonal tungsten bronzes, and M.Sc. Nora Stalte Løndal (IMA) synthesized the barium containing tetragonal tungsten bronzes. Caren Regine Zeiger and Nora Stalte Løndal also performed the X-ray diffraction and electrical measurements on the tetragonal tungsten bronzes. The single crystalline

gadolinium molybdate was prepared by Edith Bourret and Didier Perrodin from the Lawrence Berkeley National Laboratory, USA. Furthermore, Maria Tsoutsouva (IMA, now ONERA) is acknowledged for her technical assistance with the temperature dependent X-ray diffraction study.

This thesis is based on two published papers and three manuscripts. Chapter 1-3 provides an introduction, the background, and experimental details for the work presented. A summary of the results is presented in chapter 4, and a conclusion is given in chapter 5. An overview of the papers and manuscripts included in the thesis is given on the next page

Papers and manuscripts included in the thesis

Paper 1

Epitaxial (100), (110), and (111) BaTiO₃ films on SrTiO₃ substrates - A transmission electron microscopy study

Nylund, I.-E.*, Raeder, T. M., Vullum, P. E., Grande, T.

Journal of Applied Physics **129**, 095304 (2021)

*Carried out all the TEM experiments and data analysis. Wrote the first draft of the manuscript.

Manuscript 1

Exploring the role of Bi 6s lone pair in tetragonal tungsten bronzes A₄Bi₂Nb₁₀O₃₀ (A = Na, K, Rb)

Nylund, I.-E.*, Zeiger, C. R., Peng, D., Vullum, P. E., Walker, J., Einarsrud, M.-A., Grande, T.

To be submitted

*Planned and performed the TEM work and analysed the TEM data together with D. Peng. Jointly wrote the first draft of the manuscript together with C. R. Zeiger.

Manuscript 2

Cation disorder in Ba₄M₂Nb₁₀O₃₀ (M=Na, K, Rb) tetragonal tungsten bronzes

Nylund, I.-E.*, Løndal, N. S., Walker, J., Vullum, P. E., Einarsrud, M.-A., Grande, T.

To be submitted

*Planned and performed the TEM experiments and data analysis. Jointly wrote the first draft of the manuscript together with N. S. Løndal.

Manuscript 3^a

Scanning transmission electron microscopy of the improper ferroelectric Gd₂(MoO₄)₃

Nylund, I.-E.

Paper 2

Observation of cation-specific critical behavior at the improper ferroelectric phase transition in Gd₂(MoO₄)₃

Nylund, I.-E.*, Tsoutsouva, M., Grande, T., Meier, D.

Accepted by Physical Review Materials

*Synthesised the ceramic Gd₂(MoO₄)₃. Participated in the planning and execution of the X-ray diffraction study, and performed the data analysis with contributions from Maria Tsoutsouva. Wrote the first draft of the manuscript.

^aThis manuscript is not intended for publication in its present form.

Papers omitted from the thesis

Controlled Growth of $\text{Sr}_x\text{Ba}_{1-x}\text{Nb}_2\text{O}_6$ Hopper- and Cube-Shaped Nanostructures by Hydrothermal Synthesis

Grendal, O. G., Nylund, I.-E.*, Blichfeld, A. B., Tominaka, S., Ohara, K., Selbach, S. M., Grande, T., Einarsrud, M.-A.

Chemistry – A European Journal, Wiley **26**, 9348 (2020)

*Performed the TEM work and contributed to the analysis of the TEM data.

Anisotropic in-plane dielectric and ferroelectric properties of tensile-strained BaTiO_3 films with three different crystallographic orientations

Raeder, T. M., Holstad, T. S., Nylund, I.-E.*, Einarsrud, M.-A., Glaum, J., Meier, D., Grande, T.

AIP Advances **11**, 025016 (2021)

*Performed the TEM work presented in the paper.

The Structure, Morphology, and Complex Permittivity of Epoxy Nanodielectrics with In Situ Synthesized Surface-Functionalized SiO_2

Adnan, M. M., Nylund, I.-E.*, Jaworski, A., Hvidsten, S., Ese, M.-H. G., Glaum, J., Einarsrud, M.-A.

Polymers **13**, 1469 (2021)

*Acquired the TEM images presented in the work.

Structures and Role of the Intermediate Phases on the Crystallization of BaTiO_3 from an Aqueous Synthesis Route

Bakken, K., Pedersen, V. H., Blichfeld, A. B., Nylund, I.-E.*, Tominaka, S., Ohara, K., Grande, T., Einarsrud, M.-A.

ACS Omega **6**, 9567 (2021)

*Acquired the TEM images presented in the work.

Tailoring Preferential Orientation in BaTiO_3 -based Thin Films from Aqueous Chemical Solution Deposition

Bakken, K., Blichfeld, A. B., Nylund, I.-E.*, Chernyshov, D., Glaum, J., Grande, T., Einarsrud, M.-A.

Chemistry-Methods **2**, e202200002 (2022)

*Acquired the TEM images presented in the work.

Acknowledgements

There are many people who deserve recognition for the help and support they have provided throughout my time as a PhD student. First of all I would like to thank Tor Grande. I don't think we had properly met before the day he accepted the job as my main supervisor after my time as a PhD candidate got off to a somewhat rocky start, when my former supervisor left NTNU. I really appreciate how he has taught me to believe in my own work and the steady guidance he has provided. I'm equally grateful to my co-supervisor Per Erik Vullum for being such a wonderful mentor when it comes to everything regarding TEM and FIB. His skills and enthusiasm, which he has gladly shared with me, has really played a great role for my work. This thesis wouldn't have been the same without any of them. I also want to thank Mari-Ann Einarsrud for the effort she has put in as a co-supervisor, making sure everything I have written is accurate.

I feel lucky for having been a part of the FACET research group during my time as a PhD student. I'm grateful for the collaborative environment you all have provided and all the fun we have had. I have especially enjoyed the company of all the people in K1 who love to make silly memes and have long lunches. Thanks to Ola for introducing me to the TTBs and always answering my questions about Rietveld refinement, thanks to Trygve for providing the BaTiO₃ films, and thanks to Kristine for insight into the aqueous CSD process. I learnt a lot from you and the other people in the TOPPFORSK project. And thanks to the TTTB (Tor's TTB) gang, Caren, Nora, and Ben, for giving me the opportunity to join an interesting research project and for all the fun and support you have provided during the second half of my PhD. Furthermore, I'm grateful for having had the opportunity to be an associated member of the TEM group at NTNU. I have really enjoyed our Thursday and Friday lunches over the years, where we have discussed everything and anything TEM related (and not TEM related). I want to give an extra shout-out to the engineers in the TEM group, Bjørn Gunnar Soleim, Emil Frang Christiansen, and Ragnhild Sæterli, for always keeping the instruments running and answering all my questions no matter how big or small. A special thanks to Emil for helping me with simulations and to Ding Peng for sharing his knowledge about CBED. Lastly, I want to thank my parents for their support and encouragement over the years I have spent in Trondheim, and Håvard for reminding me that I would regret it if I didn't finish what I started and that I am in fact capable of getting through a PhD.

Acronyms

ABN	$A_4\text{Bi}_2\text{Nb}_{10}\text{O}_{30}$, $A=\text{Na, K, or Rb}$
ADF	annular dark-field
APB	anti-phase boundary
BMN	$\text{Ba}_4M_2\text{Nb}_{10}\text{O}_{30}$, $M=\text{Na, K, or Rb}$
BF	bright-field
BFP	back focal plane
BKN	$\text{Ba}_4\text{K}_2\text{Nb}_{10}\text{O}_{30}$
BNN	$\text{Ba}_4\text{Na}_2\text{Nb}_{10}\text{O}_{30}$
BRN	$\text{Ba}_4\text{Rb}_2\text{Nb}_{10}\text{O}_{30}$
CBED	convergent-beam electron diffraction
CCD	charge-coupled device
CL	Cliff-Lorimer
CSD	chemical solution deposition
DF	dark-field
DFT	density functional theory
DPC	differential phase contrast
DSC	differential scanning calorimetry
EDS	energy-dispersive X-ray spectroscopy
EELS	electron energy-loss spectroscopy
FEG	field emission gun
FFT	fast Fourier transform
FIB	focused ion beam
FOLZ	first-order Laue zone
GM	Gjømmes-Moodie
HAADF-STEM	high-angle annular dark-field STEM
HOLZ	higher-order Laue zone
KBN	$\text{K}_4\text{Bi}_2\text{Nb}_{10}\text{O}_{30}$
LDA	local density approximation
PBN	$\text{Pb}_2\text{Bi}_2\text{Nb}_{10}\text{O}_{30}$
PN	$\text{Pb}_5\text{Nb}_{10}\text{O}_{30}$
RAS	reduced area scanning
RBN	$\text{Rb}_4\text{Bi}_2\text{Nb}_{10}\text{O}_{30}$

ROI region of interest
SAD selected area diffraction
SBN $(\text{Sr}_{1-x}\text{Ba}_x)_5\text{Nb}_{10}\text{O}_{30}$
SEM scanning electron microscope
STEM scanning transmission electron microscopy
TEM transmission electron microscope
TTB tetragonal tungsten bronzes
XRD X-ray diffraction
ZLP zero-loss peak
ZOLZ zeroth-order Laue zone

Contents

Summary	i
Preface	v
Acknowledgements	ix
1 Introduction	3
1.1 Motivation	3
1.2 Aim of the work	6
2 Background	7
2.1 Ferroic materials	7
2.1.1 Macroscopic characteristics	7
2.1.2 Microscopic origin of ferroelectricity	8
2.1.3 Ferroelectric domains	10
2.1.4 Thermodynamic description	12
2.1.5 Multiferroic and improper ferroelectric materials	13
2.1.6 Barium titanate	14
2.1.7 Tetragonal tungsten bronzes	16
2.1.8 Gadolinium molybdate	18
2.2 Transmission electron microscopy	21
2.2.1 Introduction	21
2.2.2 Crystallography	22
2.2.3 Instrumentation	23
2.2.4 Parallel-beam diffraction and imaging	25
2.2.5 Convergent-beam electron diffraction	29
2.2.6 Scanning transmission electron microscopy imaging	32
2.2.7 Image simulation	34
2.2.8 Energy-dispersive X-ray spectroscopy	36
2.2.9 Electron energy-loss spectroscopy	38
2.3 Focused ion beam	40
2.3.1 Basic principles	40

3	Experimental details	43
3.1	Materials	43
3.1.1	Barium titanate films on strontium titanate substrates	43
3.1.2	Bismuth containing tetragonal tungsten bronzes	43
3.1.3	Barium containing tetragonal tungsten bronzes	44
3.1.4	Gadolinium molybdate	44
3.2	Specimen preparation by focused ion beam	45
3.2.1	Instrumentation	45
3.2.2	Conventional preparation technique	45
3.2.3	Preparation of <i>in situ</i> specimen	49
3.3	Transmission electron microscopy analysis	54
3.4	X-ray diffraction	54
4	Summary of results	55
4.1	Epitaxial (100), (110), and (111) BaTiO ₃ films on SrTiO ₃ substrates	55
4.2	Filled tetragonal tungsten bronzes	59
4.3	TEM investigations and phase transition in improper ferroelectric Gd ₂ (MoO ₄) ₃	65
5	Conclusion	71
	Appendices	81
	Paper 1	83
	Manuscript 1	103
	Manuscript 2	131
	Manuscript 3	151
	Paper 2	163

Introduction

1.1 Motivation

Since its invention in the 1930s, the transmission electron microscope (TEM) has played an essential role in the field of materials science because of its unrivalled ability to study materials at the nanoscale. Within a year of the first published TEM image, the resolution of the light microscope was surpassed, and has continued to improve ever since, as shown in Figure 1.1.1 [1, 2]. The introduction of commercially available aberration-corrected microscopes more than a decade ago routinely enables atomic resolution for the TEM at frequently used high voltages of 80-300 kV. A typical example demonstrating the resolution of the TEM, is the ability to resolve the two-atom dumbbells along the [110] direction of semiconductor materials like Si, Ge, InAs, which has a spacing between 1.36 and 1.51 Å, or even the spacing between two Ga atoms in [112] oriented GaN, which is 0.63 Å [3].

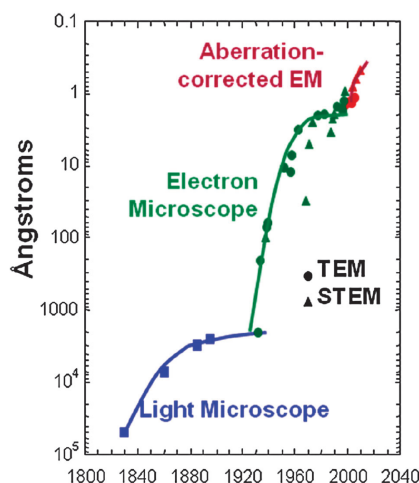


Figure 1.1.1 The evolution of the point resolution in light and electron microscopes. Republished with permission of Royal Society of Chemistry, from Recent developments and applications of electron microscopy to heterogeneous catalysis, J. C. Yang *et al.*, 41, 2012; permission conveyed through Copyright Clearance Center, Inc.

Nowadays, novel materials properties are engineered by controlling the growth at an atomic scale. The TEM enables materials scientists information at this scale, thus it is an important tool in developing new materials with novel properties, and will continue to be important in the future.

Among a wide variety of technologically important classes of functional materials that have been studied over the past decades, are ferroelectrics. Such materials are characterized by the possession of a non-zero polarization in the absence of an external electrical field. Furthermore, the polarization can be switched by the application of an electrical field. In 2021, the 100-year anniversary of the first publication on a ferroelectric material was celebrated [4]. Ferroelectric materials are also piezoelectric, and are widely used in different applications, like sensors, transducers, and actuators. Another important application of ferroelectric materials are as capacitors due to the typically high relative permittivity [5]. Many years after the first publication on ferroelectric materials, in 1969, Aizu coined the term *ferroelastic* as a mechanical stress-strain analogue to the polarization-electric field relationship in ferroelectric materials [6]. Recently, materials possessing multiple (coupled) ferroic orders have attracted great interest. These materials are known as multiferroics. In terms of the application of multiferroic materials, the idea is to control the magnetic states with an electric field, instead of a magnetic field, which can reduce waste heat and other unwanted effects. By doing so, this can lead to faster, smaller and more energy-efficient data-storage technologies. In addition, multiferroics display intriguing physical properties which are interesting from a fundamental perspective [7–9].

Polarization in ferroelectric materials exists if the crystal structure is non-centrosymmetric, making TEM a suitable tool for characterizing these materials. One of the advantages of diffraction in the TEM compared to, for example, X-ray diffraction (XRD), is that the scattering is dynamic, i.e., unless your specimen is extremely thin, multiple scattering events will occur. This provides three dimensional information and reveals lacking symmetry due to a non-centrosymmetric unit cell, as opposed to XRD, which in most cases can be described as kinematical where all crystal structures will appear to have a center of symmetry [10]. Other reasons to characterize materials with TEM is based on its unrivalled spatial resolving power, combined with the possibility of chemical mapping, and the ability to study the crystal structure by various diffraction techniques.

Examples from recent years where TEM has provided otherwise unobtainable information within the field of ferroic materials is to a great extent based on the ability to acquire images with atomic resolution. Combined with image analysis, it is possible to determine atomic shifts at the pm scale away from a centrosymmetric position, as demonstrated for the Ti-ion in BaTiO₃ by Kobayashi *et al.* [11]. The same method was applied by Yadav *et al.* who showed that polarization vortices appear in the PbTiO₃ layers in a

(SrTiO₃)₁₀/(PbTiO₃)₁₀ superlattice [12]. Building upon the same technique, and by adding analysis of the atom column intensity, Li *et al.* demonstrated how Sm doping of Pb(Mg_{1/3}–Nb_{2/3})O₃-PbTiO₃ leads to an enhanced local structural heterogeneity explaining the increased piezoelectric properties of the material [13]. Atomically resolved TEM has also aided in the clarification of the inner structure of topological defects in the improper ferroelectric Er_{1-x}Zr_xMnO₃ [14]. Another example, where diffraction obtained by a convergent beam was utilized, is by Shao and Zuo, who demonstrated that BaTiO₃ single crystal display nanoscale regions with fluctuating symmetry, whilst maintaining the macroscopic tetragonal symmetry at a larger scale [15].

In this work, TEM was utilized to study three selected ferroelectric materials systems. The first is BaTiO₃ deposited as thin films on differently oriented SrTiO₃ substrates by chemical solution deposition, the second is a range of ferroelectric tetragonal tungsten bronzes with different chemical compositions, and the last system is the improper ferroelectric and ferroelastic Gd₂(MoO₄)₃.

1.2 Aim of the work

This thesis is divided into three different case studies. Common for the three cases is that TEM is used to study ferroelectric materials.

In the first case, BaTiO₃ films deposited on (100), (110), and (111) oriented SrTiO₃ substrates, via aqueous chemical solution deposition (CSD), were studied. The BaTiO₃ films were under an in-plane tensile strain due to the difference in thermal expansion coefficient for SrTiO₃ and BaTiO₃. The degree of epitaxy and structural defects, like misfit dislocations, were characterized by a combination of electron diffraction and high-resolution scanning transmission electron microscopy (STEM) imaging. Based on this, the most frequently observed Burgers vectors for the differently oriented films were determined. Further, electron energy-loss spectroscopy (EELS) was used to study the chemical abruptness at the substrate-film interface, as well as the chemical inhomogeneity at the boundaries between the spin-coated layers of the BaTiO₃ films.

The second system studied was the tetragonal tungsten bronzes (TTB), with general chemical formula $A1_2A2_4B_{10}O_{30}$. Two different TTB series were investigated with two separate objectives. In the first project, the main objective was to determine the unknown crystal structure of K₄Bi₂Nb₁₀O₃₀ and Rb₄Bi₂Nb₁₀O₃₀, by convergent-beam electron diffraction (CBED). In the second project, the main goal was to study cation disorder in a range of tetragonal tungsten bronzes with different chemical compositions using energy-dispersive X-ray spectroscopy (EDS). The compositions of the investigated materials were Ba₄Na₂Nb₁₀O₃₀, Ba₄K₂Nb₁₀O₃₀, and Ba₄Rb₂Nb₁₀O₃₀, which differ only by the exchange of the alkali metal on the A1-site. The main research question in this project was if there is any relationship between the degree of mixing of the A1 and A2, and the ionic radius of the alkali metals.

The third case was the study of the improper ferroelectric gadolinium molybdate (Gd₂(MoO₄)₃). This is a three-dimensional ferroelectric, meaning that atoms move in all three directions, with the same order of magnitude, upon polarization reversal. The main goal in this project was to investigate if it is possible to determine the polarization direction from high-resolution STEM imaging. Furthermore, *in situ* biasing was attempted. A sample preparation method using focused ion beam (FIB) was developed for this purpose, however the *in situ* biasing in the TEM turned out to be challenging. Lastly, to gain more insight into the phase transition of the improper ferroelectric ferroelastic Gd₂(MoO₄)₃, temperature dependent XRD combined with Rietveld refinement of the diffraction data was carried out to investigate the displacement of specific cations within the unit cell through the phase transition.

Background

2.1 Ferroic materials

2.1.1 Macroscopic characteristics

Polarization (\mathbf{P}) is a material property which is defined as the dipole moment per unit volume. The total dipole moment of charge q_n at position \mathbf{r}_n , is given by [16]

$$\mathbf{p} = \sum q_n \mathbf{r}_n. \quad (2.1.1)$$

A ferroelectric material possesses a non-zero spontaneous polarization, which can be reoriented by the application of an electric field (E). This property is demonstrated by the P - E hysteresis loop shown in Figure 2.1.1. Shown in the figure is the remnant polarization (P_r) and the coercive field (E_c), which respectively describe the polarization present when no field is applied, and the field strength which must be applied to switch the polarization direction [17]. Above a certain transition temperature known as the Curie temperature or T_C , a ferroelectric material loses its spontaneous polarization and becomes paraelectric.

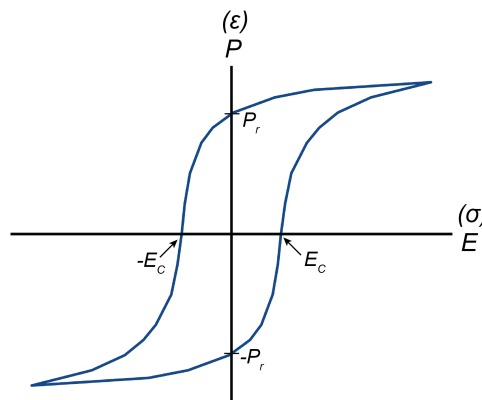


Figure 2.1.1 Ferroelectric (ferroelastic) hysteresis loop. The remnant polarization P_r and coercive field E_c are indicated.

All ferroelectric materials are simultaneously pyroelectric and piezoelectric. A pyroelectric material exhibits a spontaneous polarization which changes as a function of temperature, but the polarization orientation cannot be reoriented by the application of an electric field. In a piezoelectric material, electric charge accumulates at the surface by the application of a mechanical stress, known as the *direct piezoelectric effect*. All piezoelectric materials are also subject to the *inverse piezoelectric effect*, where a deformation of the material is caused by the application of an electric field. Finally, ferroelectric materials must be dielectric, i.e., with no free charges, in order to maintain a net polarization [18]. According to Neumann's principle [19], the symmetry of a physical property of any kind must include the point symmetry of the crystal. As a result, of the 32 crystallographic point groups which exist in three dimensions, only 20 allow piezoelectric properties, and only 10 out of the 20 provide the possibility of pyroelectric properties. Lastly, a subgroup of the pyroelectric materials also possess ferroelectric properties. Figure 2.1.2 gives an overview of the materials categorization.

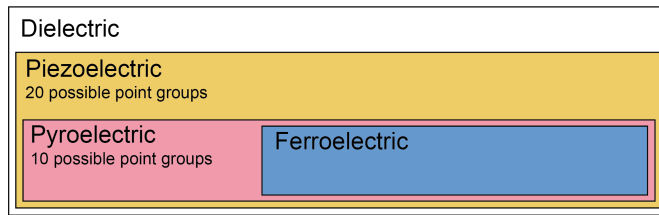


Figure 2.1.2 Categorization of dielectric, piezoelectric, pyroelectric, and ferroelectric materials.

A mechanical analogue to ferroelectric materials is ferroelastic materials. The term ferroelastic was coined by Aizu in 1969, and the property is defined such that mechanical strain (ϵ) and stress (σ) in a ferroelastic material correspond to the electric polarization and field in a ferroelectric material [6]. Similarly to the P - E hysteresis loop for a ferroelectric material, a stress-strain hysteresis loop can be drawn for ferroelastic materials, as indicated by the parameters in parenthesis in Figure 2.1.1.

2.1.2 Microscopic origin of ferroelectricity

The initial historical outline presented in this subchapter follows the historical introduction made by Lines and Glass in their monograph [17].

The first material which was discovered to be ferroelectric was Rochelle salt ($\text{NaKC}_4\text{H}_4\text{O}_6 \cdot 4\text{H}_2\text{O}$), discovered by Valasek in 1921 [4]. The first *series* of isomorphous ferroelectric materials was then made by Busch and Scherrer in 1935-1938, consisting of phosphates and arsenates. The principal example amongst these was KH_2PO_4 (KDP). Since Rochelle

salt and KDP both contain hydrogen, it was long believed that the hydrogen bonding was a likely prerequisite for ferroelectricity. In addition, Rochelle salt and KDP consist of 112 and 16 atoms per unit cell, respectively, which made it complicated to develop an atomic scale theory explaining ferroelectric properties. The discovery of ferroelectric switching in BaTiO_3 [20] together with the determination of its structure rapidly changed the conditions for the development of a microscopic theory of ferroelectricity. The first correct determination of the cubic high temperature and the room temperature tetragonal crystal structure of BaTiO_3 is attributed to Helen Megaw [21, 22]. BaTiO_3 has the perovskite structure with a simple unit cell only containing five atoms, as shown in Figure 2.1.3, where the c -axis of the tetragonal phase is the polar axis. These experimental discoveries

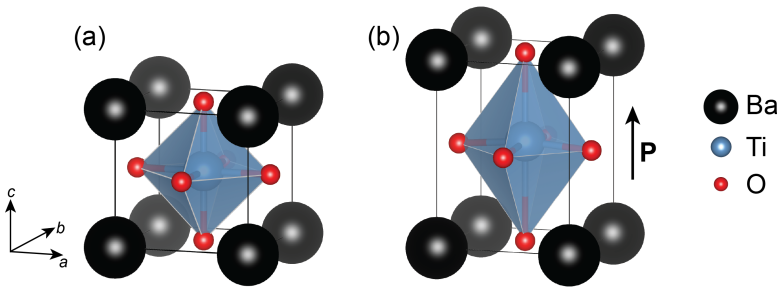


Figure 2.1.3 The perovskite structure of BaTiO_3 (a) in the prototypic cubic phase and (b) in the tetragonal phase, with a net polarization indicated. (The length of the polar axis is exaggerated for clarity.) The figure is made using Vesta [23]

in the middle of the 1940s and early 1950s lead to the development of the theories which laid the foundation for our understanding of displacive ferroelectric transitions today: In the high temperature phase, the ions responsible for creating a non-zero dipole moment perform small harmonic oscillations around their average centrosymmetric position. At the ferroelectric transition, the ions are displaced to a new average position such that a net dipole moment is created [24]. Anderson [25] and Cochran [26] are known for introducing the “soft” phonon mode to describe ferroelectric displacive transitions. Phonons describe the quantized collective vibrational motion of the crystal lattice, and in that sense the soft-mode description includes the dynamics of the entire lattice in order to describe the ferroelectric transition. At the transition, a specific phonon mode’s frequency will fall to zero. The phonon modes can be considered as the restoring forces against a set of atomic displacements, and when that restoring force vanishes, the structure will become distorted such that a net polarization can occur [27, 28]. Another important model for phase transitions, relevant for ferroelectric materials, is the order-disorder transition. In this model, the atoms controlling the symmetry at the transition perform thermally activated jumps between two or more equilibrium positions, and it is the collective distribution of the atom positions which determine the symmetry and the transition point of the material [24]. Originally, perovskite ferroelectrics were believed to belong to the class of

displacive ferroelectrics as introduced by Cochran, however, along with new and improved experimental techniques providing higher spatial and temporal resolution, transitions with a mixed nature has been discovered. For example, in a paper from 2004, Stern reconciles the seemingly contradictory order-disorder and displacive nature of the phase transition in BaTiO₃ [29]. Stern concludes that the order-disorder component of the phase transition consists of local displacements from cubic symmetry, partially losing long-range correlations, but remaining constant in magnitude across phase transitions, while the displacive component is a reorientation of the local displacements relative to the $\langle 111 \rangle$ direction as the disorder increases. Traces of the order-disorder nature of BaTiO₃ has also been observed by scanning CBED [15], although the authors propose that volumes smaller than 35 nm³ must be probed to fully clarify the microscopic origin of the ferroelectric phase transitions.

A significant contribution to the microscopic understanding of ferroelectricity was published by Cohen in 1992 [30]. Here, computational methods were employed to calculate different energy contributions from first principles using the local density approximation (LDA) within the density functional theory (DFT) framework. This was used to explain why structurally similar, but chemically different PbTiO₃ and BaTiO₃ display different ferroelectric behaviour. Essentially, the difference between the two materials can be explained by the energy overlap between Pb *6s* and O *2p* orbitals, which causes a large strain ($c/a = 1.06$) and stabilizes the tetragonal phase already at a high temperature ($T_C = 493$ °C) in PbTiO₃. Whereas the interaction between Ba and O is completely ionic, i.e., there is no orbital overlap between Ba *5p* and O *2p*. This results in multiple phase transitions at lower temperatures for BaTiO₃, with the ground state being a rhombohedral distortion below -90 °C.

2.1.3 Ferroelectric domains

Domains can form in ferroelectric materials [18]. Within one ferroelectric domain the polarization is aligned in the same direction, and in the neighbouring domain the polarization is aligned along a different direction. By applying an electric field, the polarization within the domains can be reoriented. The presence of domains at a microscopic level explains the macroscopic behaviour demonstrated by the P - E loop in Figure 2.1.1. Before applying an electric field, all domains are randomly oriented and the net polarization is zero. By applying the field, the majority of the domains will be oriented along the electric field direction, depending on the crystallographic orientation of the grains, and a maximum net polarization is reached. When the field is removed, most domains remain in their poled state, hence at zero electric field, there is a remnant polarization P_r present. If the angle between the polarization in two neighbouring domains are 90° or 180° , the boundary between them are known as 90° or 180° domain walls,

respectively. Using tetragonal BaTiO_3 as a model system (Figure 2.1.3), there are six equivalent orientations for the formation of the spontaneous polarization. Generally, the central Ti-ion can be displaced towards any of the six cube faces. This means that the direction along which the polarization will develop depends on the electrical and mechanical boundary conditions imposed on the material [18]. As can be seen in the lower part of Figure 2.1.4, a spontaneous polarization is developed along with the elongation of the c -axis at the phase transition. This polarization leads to a high surface charge, and a high depolarization field (E_d) is formed at a large energy cost. By forming multiple 180° stripe-domains, the surface charge is greatly reduced. Thus the formation of these domains are energetically favourable. The upper part of Figure 2.1.4, demonstrates schematically how the application of a mechanical stress changes the boundary conditions, and thus changes the resulting domain pattern to include 90° domain walls. Both 90° and 180° domain walls may reduce the effects of the depolarizing electric field, but only formation of 90° domain walls minimize the elastic energy [18].

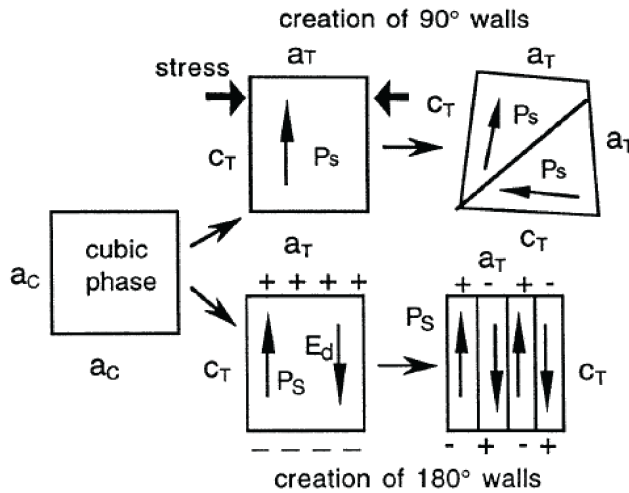


Figure 2.1.4 The formation of 90° and 180° domains in a tetragonal structure, where a_c describes the a lattice parameter of the cubic phase, and a_T and c_T describe the a and c parameters of the tetragonal phase. Republished with permission of IOP Publishing, Ltd, from Ferroelectric, dielectric and piezoelectric properties of ferroelectric thin films and ceramics, Dragan Damjanovic, 61, 1998; permission conveyed through Copyright Clearance Center, Inc.

2.1.4 Thermodynamic description

The theoretical framework which is often used to describe ferroic response anomalies due to external stimuli, such as temperature change, is termed the *thermodynamic approach*. The theory was originally developed by Landau in 1937 [31], and further applied by Ginzburg and Devonshire to describe the phase transition and properties of BaTiO₃ [32, 33]. Although the thermodynamic approach falls short of a fundamental explanation for the driving mechanism behind the evolution of polarization in ferroelectrics, it is useful due to its mathematical simplicity and ability to describe a wide range of correlated macroscopic parameters. Lines and Glass [17] and Tagantsev *et al.* [24] provide a thorough review of the theory and present important results for first- and second-order ferroelectric phase transitions. This section is based on the two monographs, and will be limited to reviewing the most important results for a first-order phase transition, since the phase transitions of most ferroelectric materials (including BaTiO₃ and Gd₂(MoO₄)₃) can be described as first-order.

A common starting point for the thermodynamic approach is to consider the thermodynamic potential which best describes the ferroelectric state below the transition temperature T_C . Normally, the most convenient potential is the elastic Gibbs function (G) which can be written in terms of deviation from the prototype paraelectric state. It can be expressed as

$$G = \frac{\alpha}{2}P_z^2 - \frac{\beta}{4}P_z^4 + \frac{\gamma}{6}P_z^6, \quad (2.1.2)$$

where the coefficients $\alpha, \beta, \gamma > 0$, and the β term is negative to describe a first-order transition. Furthermore, it is assumed the polarization P_z is only directed along the z -axis of the crystal. Equation (2.1.2) describes a *proper* ferroelectric, where the polarization is used as the order parameter. In addition, all stresses are zero and the paraelectric phase is centrosymmetric. In the simplest description, α is the only temperature dependent coefficient, which can be written on the Curie-Weiss form as

$$\alpha = \alpha_0(T - T_0), \quad \alpha_0 > 0. \quad (2.1.3)$$

Figure 2.1.5 displays the qualitative behaviour of G versus P for different temperatures. The figure illustrates how local minima are developed before reaching T_C from above, and that multiple local minima persists below T_C . This demonstrates that thermal hysteresis can be present in materials of first-order and that multiple phases can coexist. Lastly, at $T \gg T_C$ there is only one local minima at $P = 0$, and for $T \ll T_C$, global minima are located at $\pm P$. This phenomenological approach can be further developed to describe other cases, involving other external stimuli like application of stress or electric field.

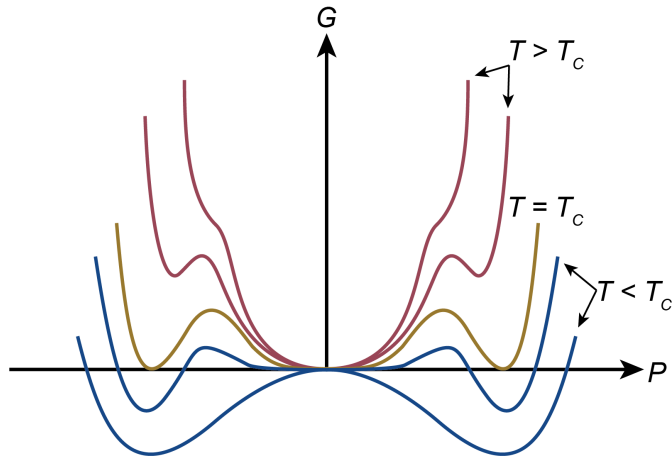


Figure 2.1.5 Qualitative behaviour of G as a function of P at different temperatures around T_C . The figure is inspired by [24].

2.1.5 Multiferroic and improper ferroelectric materials

As the field of ferroelectric, ferromagnetic, and ferroelastic materials science has developed, so has the terms or nomenclature which is used to describe them. Today, the term multiferroic usually refers to a material which has both a ferroelectric and ferromagnetic ordering. Ideally, these properties should be coupled and coexist at room temperature, since the control of magnetic domains via electric field has huge technological potential in nanoelectronic devices which could potentially use considerably less energy than what is currently on the market [7]. However, today's technologically important ferroelectric materials crystallize in the perovskite structure. In this structure ferroelectric and ferromagnetic properties contradict each other since ferroelectricity in general require an empty d -orbital, whereas magnetic ordering requires half filled d -orbitals [34]. The main focus for the past years has thus been to search for different materials where ferroelectricity and ferromagnetism can coexist. This has brought much attention to *improper* ferroelectric materials, which are defined as materials where the order parameter describing the phase transition is not the polarization. An example of an improper ferroelectric material is the rare-earth manganite ($RMnO_3$), which is a so-called geometric ferroelectric material, meaning that a structural distortion at the phase transition (which is used as the order parameter), results in a net polarization below T_c [7]. $Gd_2(MoO_4)_3$ is another example of an improper ferroelectric which will be described in further detail in Section 2.1.8.

2.1.6 Barium titanate

BaTiO_3 is known as a prototypical lead-free proper ferroelectric material, which crystallizes in the perovskite structure (Figure 2.1.3). It is cubic above T_C , and by cooling from the cubic phase, it goes through three phase transitions. At the first transition around 120°C , it becomes tetragonal with the remnant polarization along the c -axis. At -5°C , it becomes orthorhombic with polarization along the face diagonal, and lastly, below -90°C , BaTiO_3 transforms to a rhombohedral structure where the polarization is now along the body diagonal [35].

In terms of applications, the piezoelectric properties of BaTiO_3 is greatly surpassed by $\text{Pb}(\text{Zr}_x\text{Ti}_{1-x})\text{O}_3$, which has a larger piezoelectric coupling and a higher operating temperature than BaTiO_3 [36]. However, BaTiO_3 has a high permittivity, which is an important property for capacitors. In fact, BaTiO_3 based ceramics account for the bulk of all capacitors used in electronics (billions per year) [5]. The permittivity of single domain BaTiO_3 is given as a function of temperature in Figure 2.1.6, which shows that the permittivity is highly anisotropic, with a value ~ 20 times larger perpendicular to the polar axis compared to along the polar axis at room temperature [37].

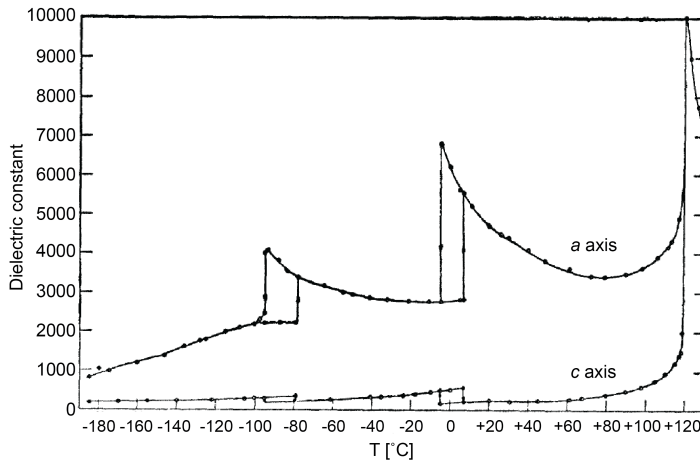


Figure 2.1.6 The permittivity of BaTiO_3 as a function of temperature. The permittivity is measured along two different axes, perpendicular to the polarization direction (a axis) and parallel to the polarization direction (c axis). Reprinted with permission from W. J. Merz, Phys. Rev., 75, 687-687, 1949. Copyright 1949 by the American Physical Society.

The properties of BaTiO_3 thin films can deviate significantly from bulk BaTiO_3 due to strain. When strain is introduced on purpose, in order to change or enhance properties, it is known as strain engineering. Strain can be introduced via two different mechanisms, as depicted in Figure 2.1.7(a) and (c). The most common way to strain a ferroelectric

material is to grow coherent epitaxial thin films on a substrate with a slightly different lattice parameter, forcing the in-plane lattice parameter of the film to obtain the same in-plane lattice parameter as the substrate, as shown in Figure 2.1.7(a). Most commonly, a substrate with a smaller lattice parameter is used, such that the ferroelectric film is under compressive strain resulting in an expansion of the c -axis out-of-plane. An example of such strain engineering was performed by Choi *et al.* [38], where the ferroelectric transition temperature of a BaTiO_3 film grown on a DyScO_3 substrate was demonstrated to increase by almost 500 °C, and the remnant polarization was shown to be at least 250 % higher than in bulk single crystal. At a certain critical thickness, coherent epitaxy is no longer possible and misfit dislocations are introduced as shown in Figure 2.1.7(b). At this stage, the film is known to be relaxed. The critical thickness to which a film can be grown coherently epitaxial is inversely proportional to the lattice mismatch between the substrate and the film [39]. In the case of a BaTiO_3 film on a SrTiO_3 substrate, which has a lattice mismatch of about 2 %, the critical thickness is determined to be 5 nm or less [40]. If a film is grown at a high temperature and thicker than the critical thickness, such that edge dislocations are introduced and the film is relaxed, a tensile strain can be introduced in the film if the thermal expansion coefficient of the film is larger than the thermal expansion of the substrate. This is shown to occur in an 180 nm thick BaTiO_3 film on a SrTiO_3 substrate [41]. The effect is known as thermal strain and it is illustrated schematically in Figure 2.1.7(c).

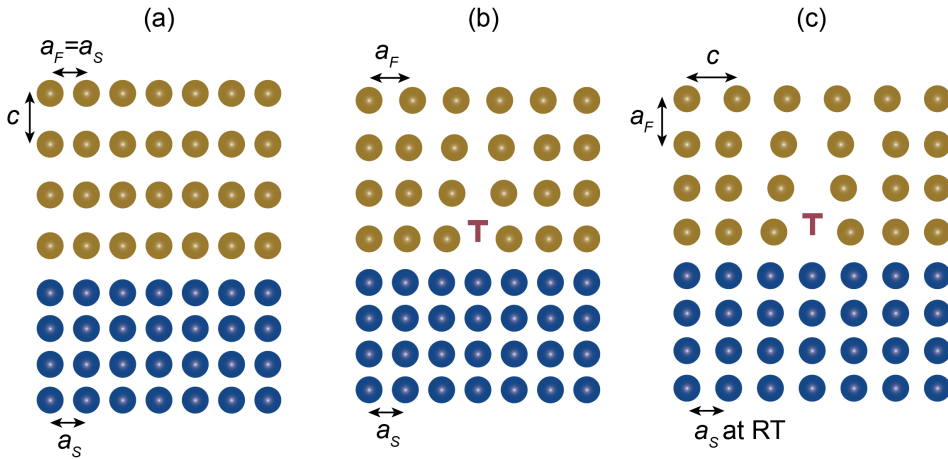


Figure 2.1.7 Schematic of different modes of epitaxial growth of a film on a substrate. (a) Coherent epitaxial growth. (b) Relaxed epitaxial growth. (c) Relaxed epitaxial growth at a high growth temperature, followed by the introduction of thermal strain during cooling to room temperature (RT).

2.1.7 Tetragonal tungsten bronzes

The second largest group of oxide ferroelectrics, after the perovskites, are the tetragonal tungsten bronzes (TTB) [17]. The prototypical TTB structure is related to the perovskite structure as illustrated in Figure 2.1.8 [42]. The network of BO_6 octahedra in the perovskite structure is shown in Figure 2.1.8(a), and the TTB structure is obtained by a 45° rotation of the four central octahedra indicated by the pink color. The TTB structure is shown in Figure 2.1.8(b), projected along the c -axis. A dashed line marks the aristotype unit cell which belongs to the $P4/mbm$ space group with lattice parameters $a = b = \sqrt{10}a_P$ and $c = a_P$, where $a_P \sim 4\text{\AA}$ is the typical unit cell lattice parameter of the perovskite structure [43].

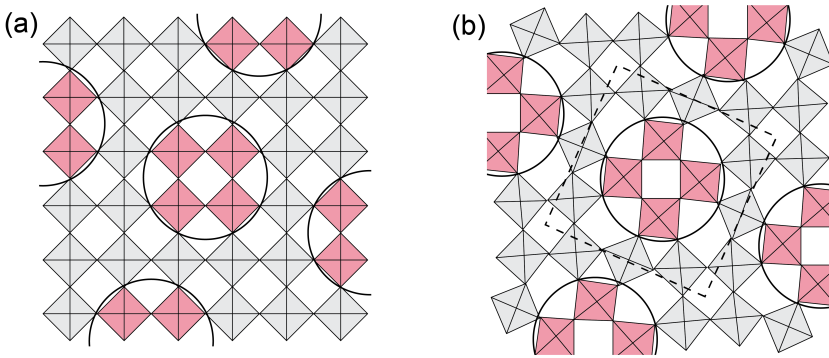


Figure 2.1.8 Sketch showing the structural relationship between the perovskite structure (a) and TTB structure (b) viewed along the c -axis.

The general chemical formula for the TTBs relates to the different types of sites that are available for cation occupation. The TTB unit cell, shown in Figure 2.1.9, consists of two square $A1$ sites, four pentagonal $A2$ sites, and four triangular C sites, in addition to a network of ten corner-sharing BO_6 octahedra, resulting in the general formula $A1_2A2_4C_4B_{10}O_{30}$ [44, 45].

The TTB structure is interesting from a materials engineering point of view, as it is versatile in terms of chemical composition and structural variations. Furthermore, the structure allows for a wide degree of filling, known as *empty*, *unfilled*, *filled*, and *stuffed*, referring to the degree of filling on the A - and C -sites of the structure [46]. *Empty* TTBs are characterized by empty C -sites and less than five out of six A -sites being occupied, *unfilled* TTBs have less than six cations at the A -sites and unoccupied C -sites, *filled* TTBs have all A -sites completely occupied and empty C -sites, whereas *stuffed* TTBs have fully occupied A -sites in addition to some or all C -sites occupied [44]. Only *filled* TTBs with $B = \text{Nb}$ were considered in this work, i.e. they have the general chemical formula $A1_2A2_4\text{Nb}_{10}O_{30}$. Note that the general formula is usually presented “in order”,

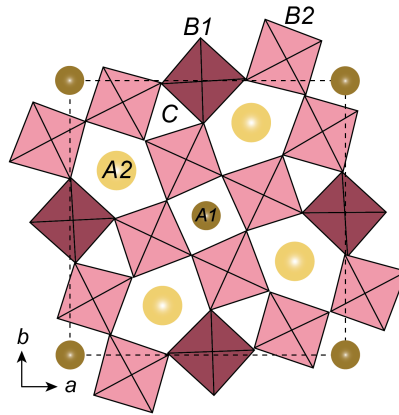


Figure 2.1.9 Schematic of the TTB structure viewed along the c -axis. The BO_6 octahedra are shown in red and pink and marked $B1$ and $B2$, respectively, reflecting the different site symmetry of the B -cation sites. The square $A1$ and pentagonal $A2$ tunnels are shown. The trigonal tunnels, marked C , are usually empty.

where $A1$ comes first, and then $A2$, whereas specific compositions are usually presented such that $A1$ and $A2$ have switched places, as in $Ba_4Na_2Nb_{10}O_{30}$, where $A2 = Ba$ and $A1 = Na$.

The TTBs have been studied for many decades, yet a complete comprehension of the properties and structure is still lacking. Unlike ferroelectrics with the perovskite structure, which are fairly well understood, the larger unit cell of the TTBs renders a plethora of possible chemical compositions to study experimentally. The large unit cell, containing 46 atoms, also makes it much more computationally heavy to study using *ab initio* methods, causing a slower progression in understanding the structure and properties from a theoretical point of view [47–49]

In addition to showing pure ferroelectric behaviour, many TTBs demonstrate a relaxor ferroelectric behaviour, like $(Sr_{1-x}Ba_x)_5Nb_{10}O_{30}$ (SBN) with $x < 0.5$ [46]. Relaxor ferroelectrics are characterized by a frequency dispersion in the electric permittivity as a function of temperature. This behaviour is not fully understood, but is believed to be connected to polar nanoregions present in the materials [50]. An attempt to categorize the TTBs depending on the different $A1$ and $A2$ cation sizes was made by Zhu *et al.* [46]. The figure summarizing the findings of this work is shown in Figure 2.1.10, where two different regimes facilitate normal ferroelectricity. First, a large average A -site ionic radii will stretch the O - B - O bond length, which enhances polarizability and promote long range ferroelectric coupling. On the other hand, a low $A1$ tolerance factor (i.e. the radius of $A1$ is small compared to the radius of B) drives the transition from incommensurate to commensurate, which is also associated with normal ferroelectricity. In between these

two competing driving forces, relaxor behavior dominates. This analysis is based solely on cation sizes, however it has also been demonstrated that the stereochemically active lone pair in Pb is important to stabilize the large in-plane polarization in $\text{Pb}_5\text{Nb}_{10}\text{O}_{30}$ (PN) [48], indicating that not only cation size, but also the type of cation can play an important role in the structure-property relations in the TTBs.

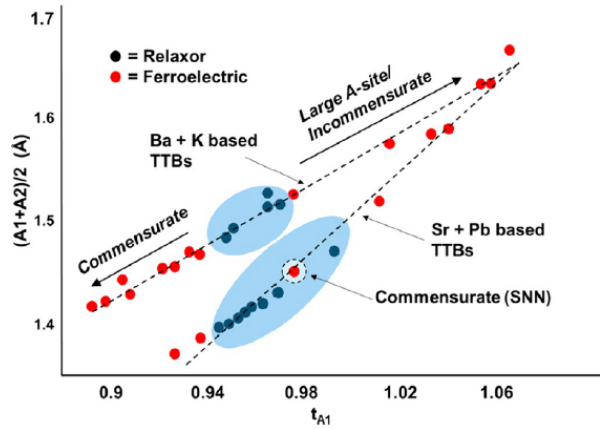


Figure 2.1.10 Two different regimes, based on the size of the A cations in the TTB structure, promote normal ferroelectricity. Between, relaxor ferroelectric behaviour dominates. Reprinted with permission from X. Zhu *et al.*, Chem. Mater. 27, 3250-3261, 2015. Copyright 2015 American Chemical Society.

It is also evident in Figure 2.1.10 that several TTBs exhibit an incommensurately modulated structure. The incommensurate modulations can manifest itself as an octahedral tilting with a periodicity which cannot be expressed as an integer times the lattice constants as in SBN [51]. Or, as evidenced by anomalous XRD experiments performed on $\text{Pb}_2\text{Bi}_2\text{Nb}_{10}\text{O}_{30}$ (PBN), incommensurate modulations can also be driven and dominated by A -site cations which are displaced compared to a specific lattice site [52].

2.1.8 Gadolinium molybdate

At room temperature, gadolinium molybdate ($\text{Gd}_2(\text{MoO}_4)_3$) is an improper ferroelectric and ferroelastic, which belongs to the orthorhombic $Pba2$ space group, also known as the β' -phase. At the Curie temperature of 159 °C, $\text{Gd}_2(\text{MoO}_4)_3$ transforms into the tetragonal β -phase, which belongs to the $P\bar{4}2_1m$ space group [53, 54]. Thermodynamically, these phases are only metastable below 857 °C [55], however, below 600 °C, $\text{Gd}_2(\text{MoO}_4)_3$ transforms imperceptibly slow from the metastable β -phase to the thermodynamically stable α -phase [17]. At the phase transition from the paraelectric and paraelastic $P\bar{4}2_1m$

phase to the ferroelectric and ferroelastic $Pba2$ phase, the unit cell volume doubles. At the transition, the c -axis remains the same, while the a and b axes are rotated 45° around the c -axis. A simple schematic of the transformation is presented in Figure 2.1.11(a). Mathematically, the transformation from the relative atom position $\mathbf{r} = \mathbf{x} + \mathbf{y} + \mathbf{z}$ in the $C\bar{4}2_1$ phase to the relative position $\mathbf{r}' = \mathbf{x}' + \mathbf{y}' + \mathbf{z}'$ in the $P\bar{4}2_1m$ phase, is described by a rotation matrix \mathbf{R} and a unit cell center shift \mathbf{t} , where:

$$\mathbf{R} = \begin{bmatrix} 1 & 1 & 0 \\ -1 & 1 & 0 \\ 0 & 0 & 1 \end{bmatrix}, \quad (2.1.4)$$

and

$$\mathbf{t} = [0, 1/2, 0], \quad (2.1.5)$$

such that

$$\mathbf{r}' = \mathbf{R}\mathbf{r} + \mathbf{t}. \quad (2.1.6)$$

Because of the unit cell doubling, Jeitschko [54] introduced the non-standard space group $C\bar{4}2_1$ for the paraelectric phase, which has the same unit cell volume and origin as $Pba2$ to facilitate easy comparison of the two phases across the phase transition. The unit cell of $\text{Gd}_2(\text{MoO}_4)_3$ in the ferroelectric and paraelectric phases are shown in Figure 2.1.11(b) and (c), respectively. In the ferroelectric state the lattice parameters of $\text{Gd}_2(\text{MoO}_4)_3$ are [54]:

$$a = 10.39, b = 10.42, \text{ and } c = 10.70 \text{ \AA}.$$

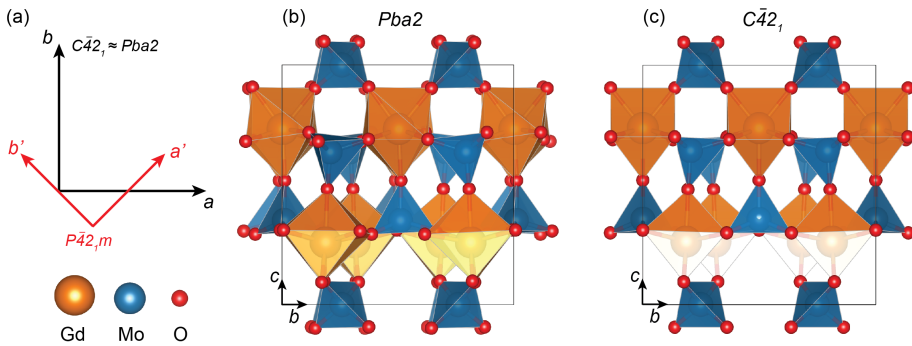


Figure 2.1.11 The $\text{Gd}_2(\text{MoO}_4)_3$ structure. (a) indicates the relationship between the prototypic $P42_1m$ and ferroic $Pba2$ space groups. (b) and (c) shows the atomic structure of $\text{Gd}_2(\text{MoO}_4)_3$ viewed along the a -axis in the ferroic and prototypic state, respectively. (b) and (c) are made using Vesta [23] with parameters from [56].

In going from the prototypical structure $P\bar{4}2_1m$ to the ferroelectric structure $Pba2$, the $\bar{4}$ operation in the prototypical space group is lost, resulting in four different possible

orientation states which are denoted: A , A' , B , and B' . A and A' , and B and B' represent phases with opposite polarization orientation, respectively. At an atomic scale A and A' (and B and B') are separated by an anti-phase boundary (APB), where the lattice is displaced by $\frac{1}{2}(a + b)$ across the boundary. This means that two types of boundaries exist in $\text{Gd}_2(\text{MoO}_4)_3$, namely domain walls and APBs. By symmetry considerations, this can occur in $\text{Gd}_2(\text{MoO}_4)_3$, since the transition from the prototypical to the ferroic point group $\bar{4}mm \rightarrow 2mm$ involves the replacement of $\bar{4}$ with 2. Further considering the space-group translational symmetry of $\text{Gd}_2(\text{MoO}_4)_3$, the 2 operation takes a different location in the ferroelectric state than the former $\bar{4}$ in the paraelectric state. Thus A , A' , B , and B' exist as separate states in $\text{Gd}_2(\text{MoO}_4)_3$ [57].

$\text{Gd}_2(\text{MoO}_4)_3$ is a three-dimensional uniaxial ferroelectric, with c as the polar axis. Figure 2.1.12 shows the atomic structure for the two different polarization states. The structure is viewed along different axes to illustrate the two different polarizations, however, the polarization reversal can also be described in terms of an exchange of the a - and b -axis and switch of the direction of the c -axis [57, 58]. Characteristic for a three-dimensional ferroelectric is that all the atoms are shifted by the same order of magnitude in all directions upon polarization reversal [17]. Keve *et al.* have measured the shifts of all atoms at polarization reversal, and the magnitude of the largest cation shift is about 13 pm, whereas the oxygen which shifts the most move about 49 pm [53].

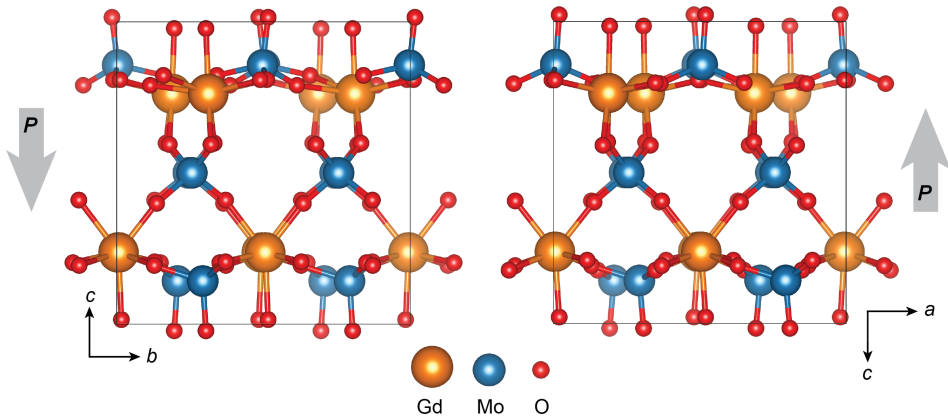


Figure 2.1.12 Atomic structure of the two polarization orientations in $\text{Gd}_2(\text{MoO}_4)_3$. The largest cation shift is about 13 pm.

2.2 Transmission electron microscopy

2.2.1 Introduction

As the name suggests, the transmission electron microscope (TEM) is a microscope which utilizes electrons as the illumination source, whereby a thin electron transparent specimen is studied by transmitting the electrons through the specimen. Since its invention, the TEM has developed to become a versatile tool for studying materials at the nanoscale. Modern TEMs have a flexible lens system which provides the opportunity to illuminate the specimen with a range of beam convergence angles. In addition, the beam can be raster scanned across the specimen, with or without a simultaneous beam tilt. Furthermore, spectroscopic data can also be acquired while scanning the beam across the sample. The most common spectroscopic techniques used in the TEM are EDS and EELS. There are multiple ways of acquiring the signal created by the electrons which have passed through the specimen. Charge-coupled device (CCD) cameras have long been the method of choice for digital acquisition of images and diffraction patterns. In addition, circular or annular-shaped scintillator detectors are used in STEM image acquisition. However, there is now a small revolution happening in the way electrons are acquired in the TEM, with the advent of direct electron detectors, which allows for much faster acquisition and read-out times, improved detector quantum efficiency, and lower noise levels [59, 60]. For now, these detectors are expensive and possess limited resolution, typically 256×256 pixels compared to CCD cameras, which typically have 2048×2048 pixels. However, they have already facilitated a range of new possibilities, and will play an important role in the future of TEM.

In this chapter, an overview of the TEM instrumentation and the techniques which have been utilized during the work with this thesis will be provided. Different techniques in the TEM can be distinguished by the use of a parallel or a convergent beam [61]. Here the parallel-beam techniques will be presented first, then different techniques utilizing a convergent beam will be explained. The overview will generally be based on the monographs by Williams and Carter [1], and Zuo and Spence [10] with reference to other works where it is relevant. To fully describe the interaction between the electron beam and the specimen, the theoretical framework known as dynamical diffraction theory must be applied, because the electron scattering in TEM is generally dynamic, meaning that multiple scattering events occur. The dynamic diffraction theory is based on solving the time-independent Schrödinger equation for an electron wave interacting with the potential from the crystal lattice of the specimen. Dynamical theory is outlined in the work by Zuo and Spence [10] and reviewed in for example *The scattering of fast electrons by crystals* by C. J. Humphreys [62]. The overview presented here will mainly provide a conceptual description based on the kinematical approximation.

2.2.2 Crystallography

Before the TEM instrumentation and techniques are described in further detail, a brief introduction to crystallography is given, to define a few important parameters related to how crystalline materials are described. The monograph by Williams and Carter [1], and by Kittel [16] are used as references in this section.

Crystalline solids consist of an arrangement of atoms repeating periodically in space. They can be described as consisting of a lattice and a basis where the lattice can be defined in terms of three primitive unit cell vectors \mathbf{a} , \mathbf{b} , and \mathbf{c} in real space as

$$\mathbf{r} = n_1\mathbf{a} + n_2\mathbf{b} + n_3\mathbf{c}, \quad (2.2.1)$$

where n_1 , n_2 , and n_3 are all integers. Any translation along an integer number of the unit cell vectors describe all possible lattice points. The basis can consist of a single atom at each lattice site, or multiple atoms at certain positions \mathbf{r}_i relative to each lattice point such that

$$\mathbf{r}_i = x_i\mathbf{a} + y_i\mathbf{b} + z_i\mathbf{c}. \quad (2.2.2)$$

Here, the unit cell origin may be arranged such that $0 \leq x_i, y_i, z_i \leq 1$.

The reciprocal lattice vector \mathbf{g}_{hkl} can be defined as

$$\mathbf{g}_{hkl} = h\mathbf{a}^* + k\mathbf{b}^* + l\mathbf{c}^*, \quad (2.2.3)$$

where the reciprocal lattice vectors \mathbf{a}^* , \mathbf{b}^* , and \mathbf{c}^* are given by

$$\mathbf{a}^* = \frac{\mathbf{b} \times \mathbf{c}}{V}, \quad \mathbf{b}^* = \frac{\mathbf{c} \times \mathbf{a}}{V}, \quad \text{and} \quad \mathbf{c}^* = \frac{\mathbf{a} \times \mathbf{b}}{V}, \quad (2.2.4)$$

where $V = \mathbf{a} \cdot (\mathbf{b} \times \mathbf{c}) = \mathbf{b} \cdot (\mathbf{c} \times \mathbf{a}) = \mathbf{c} \cdot (\mathbf{a} \times \mathbf{b})$ is the volume of the unit cell. The integers h , k , and l are the Miller indices which describe the lattice plane (hkl). They are defined such that the plane (hkl) cuts the \mathbf{a} , \mathbf{b} , and \mathbf{c} axes at $1/h$, $1/k$, and $1/l$, respectively. The real space lattice plane distance d_{hkl} is connected to the reciprocal lattice spacing $g_{hkl} = |\mathbf{g}_{hkl}|$ through

$$d_{hkl} = \frac{1}{g_{hkl}}. \quad (2.2.5)$$

The shape of a unit cell is based on the length of the unit cell vectors and the angles between them. Since a unit cell is defined such that it can fill space, 7 unique crystal systems can be defined. In addition, lattice points can be arranged at different sites in the different crystal systems. This gives rise to the 14 different Bravais lattices. They are denoted P , I , F , and C , which describe the primitive, body-centred, face-centred, and base-centred unit cells. Crystal structures can be defined in terms of the symmetry

elements which can be applied to the structure. A structure can be said to possess a certain symmetry element if the symmetry operation can be applied to the structure and the structure is invariant under the transformation. There are different types of symmetry operations. The first type considers *point* symmetry and includes the mirror, rotation, and inversion symmetry operations. The second type additionally considers *space* symmetry and includes the translational symmetry operations glide planes and screw axes, which respectively describe symmetry operations consisting of a mirror combined with translation, and a rotation combined with translation. Crystal symmetry and structure determination will be discussed further in Section 2.2.5.

2.2.3 Instrumentation

A schematic overview of a TEM instrument is shown in Figure 2.2.1. The TEM can be said to consist of three main parts: The illumination system, the objective lens and stage, and the projection system. The illumination system consists of the electron gun, the condenser lenses, and the condenser aperture. Two main types of electron sources are used in the electron gun, either a thermionic source or a field emission source. The thermionic source is usually made from a LaB₆ crystal, and electrons are emitted by heating the source to about 1700 K, thereby overcoming the work function. The field emission sources are made from thin and sharp tungsten needles, where electrons are emitted by applying a large potential. The field emission gun (FEG) must operate at higher vacuum ($10^{-6} - 10^{-9}$ Pa) than the thermionic sources (10^{-4} Pa), however it provides a more monochrome beam with a higher brightness. The role of the condenser lenses is to direct the electrons from the gun to the specimen. Two main modes exist: Parallel- or convergent-beam illumination. The different modes will be described further in Section 2.2.4, Section 2.2.5, and Section 2.2.6. The condenser aperture is used to control the beam semi-convergence angle when a convergent probe is used, or to block electrons far from the optical axis when a parallel beam is used. The most prominent lens aberrations in TEM, spherical aberrations and chromatic aberrations, increase as a function of distance from the optical axis, thus the electrons which suffer from the worst aberrations can be blocked by the use of a smaller condenser aperture. A set of deflector coils are positioned before the objective lens and stage. These can for example be used to raster scan the electron beam for STEM imaging.

The objective lens is the most important lens in the TEM since it forms the images and diffraction patterns that are magnified by the other lenses. Nowadays, the objective lens is usually split into two polepieces, where the specimen is inserted between the polepieces, as shown in Figure 2.2.1. The split polepiece configuration makes the objective lens versatile, and allows for the insertion of the EDS detector in-between the polepieces as indicated in Figure 2.2.1. Positioning the EDS detector in-between the polepieces provides the

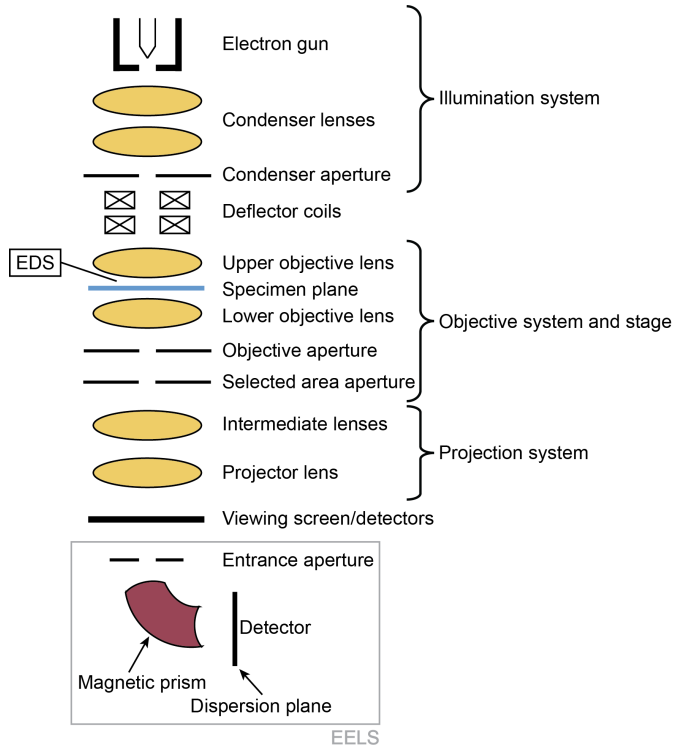


Figure 2.2.1 Simplified overview of the TEM. From the top it consists of the illumination system, the objective lenses and specimen stage, and lastly the projector system. Also shown is the deflector coils, the EDS detector which is inserted between the objective lenses, and at the bottom the viewing screen and detectors. Additionally, the EELS can be fitted to the bottom of the microscope.

shortest possible distance from the specimen to the detector thus maximizing the number of detected X-rays, since the solid angle covered by the EDS detector becomes as large as possible. The last part of the objective system is the objective aperture, which is inserted into the back focal plane (BFP) of the lower objective lens. The selected area aperture is positioned in a conjugate image plane, such that diffraction patterns can be formed from a selected area of the specimen. Both the BFP and image plane are shown in Figure 2.2.2. The projection system in a modern TEM consists of three intermediate lenses and a projector lens. The first intermediate lens enables the switch from imaging to diffraction (illustrated in Figure 2.2.2), and the rest of the system enables a wide range of magnifications or camera lengths in image mode or diffraction mode, respectively. After the projector lens, there is a viewing screen and different cameras, which are used to acquire the images or diffraction patterns. As can be seen in Figure 2.2.1, the EELS is fitted at the bottom of the microscope column. The EELS consists of an entrance aperture, a magnetic prism which disperses the electrons depending on their energy and

a detector. The technique will be described in further detail in Section 2.2.9.

The lenses in the TEM are usually electromagnetic lenses, fixed at certain positions, but it is possible to change their strength. The electromagnetic lenses are inherently difficult to make perfect, thus they suffer from different aberrations. In addition, astigmatism will occur when the electrons which are travelling down the column experience a non-uniform magnetic field. This can be caused by imperfections in the lenses, or miscentered or dirty apertures. Astigmatism is easy to correct and all TEMs are therefore equipped with condenser-, objective- and intermediate-lens stigmators. Due to the imperfect lenses, the resolution in the TEM is not limited by the wavelength of the electrons, but rather the aberrations. Erni provides a thorough introduction to aberrations in the TEM in his monograph [63]. The most detrimental aberration is the spherical aberrations, where electrons far from the optical axes are bent more than electrons close to the optical axis. The result of this aberration is that a point source is imaged as a disk with finite size, thus limiting the ability to magnify details because they are degraded by the imaging process. The basic working principle of spherical aberration correctors is to use a set of lenses which spread the off-axis electrons such that they re-converge to a point rather than a disk. There are two different commercial spherical aberration corrector systems available, one is based on multiple quadrupole and octupole lenses [64], and the other system is based on a combination of hexapole and other transfer lenses [65].

2.2.4 Parallel-beam diffraction and imaging

In the TEM, selected area diffraction (SAD) refers to a technique where the specimen is illuminated by a parallel beam, and the selected area aperture is inserted into the image plane as shown in Figure 2.2.2. This has the effect of stopping all beams from reaching the detector except for those which travel through the aperture. Thus, only diffraction information from a specific area of the specimen is obtained. Imaging with a parallel beam at low to medium magnifications is typically done by so-called bright-field (BF) or dark-field (DF) imaging, which will be described in further detail at the end of this section. It is the first intermediate lens of the TEM which is used to change between the diffraction and imaging mode, as shown in Figure 2.2.2 where the solid lines indicate the ray path of the image mode and the dashed lines indicate the ray path of the diffraction mode.

The relationship between the diffracted intensity of the electron beam and the crystal structure of the specimen can be described by Bragg's law or the Laue condition [1]. In 1925, Louis de Broglie had already theorized that electrons demonstrate a wave-like nature and that they exhibit a wave-particle duality. A particle's wavelength λ is given by $\lambda = h/p$, where h is Planck's constant and p is the momentum of the particle. Taking

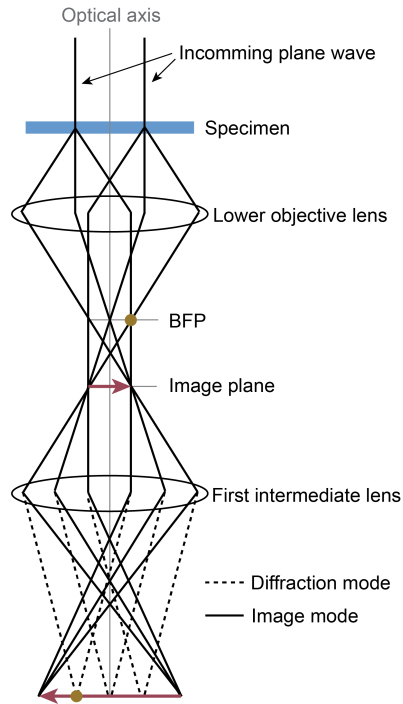


Figure 2.2.2 Ray diagram for parallel-beam illumination. The BFP and image plane are indicated in the figure. The brown spot in the BFP demonstrates that beams scattered to the same angle by the specimen converge to the same position in the BFP. The strength of the first intermediate lens can be adjusted to display an image (solid line and red arrow) or a diffraction pattern (dashed line and brown spot) on the viewing screen/detector.

relativistic effects into account, an electron accelerated at 200 kV has a wavelength of 0.025 Å. Figure 2.2.3(a) demonstrates how Bragg's law describes diffraction. A plane wave incident on a crystal lattice at an angle θ , behaves as if it is reflected off adjacent planes, separated by a distance d . Constructive interference will occur, and give rise to diffracted intensity on a detector, wherever the difference in path length equals an integer times the wave length, as described by Bragg's law:

$$n\lambda = 2d\sin\theta. \quad (2.2.6)$$

The right hand side of the equation describes the path difference indicated by the line segment ABC in Figure 2.2.3(a). Equation (2.2.6) provides a simple and useful description of diffraction, however, since it is demonstrated for reflection, as opposed to transmission, another condition known as the Laue condition is also commonly used to describe diffraction in the TEM. Bragg's law can be derived as a special case of the Laue condition. Figure 2.2.3(b) gives a schematic overview of the Laue condition, where the

incident \mathbf{k}_i and diffracted \mathbf{k}_d wave vectors for an elastic scattering event are shown. The change in direction due to the scattering is $\Delta\mathbf{k} = \mathbf{k}_d - \mathbf{k}_i$. The Laue condition states that constructive interference will occur when

$$\Delta\mathbf{k} = \mathbf{g}_{hkl}. \quad (2.2.7)$$

The Ewald sphere gives a visual demonstration of when the Laue condition is fulfilled. Whenever the Ewald sphere intersects a reciprocal lattice point, the Laue condition is fulfilled. The length of the wave vectors are given by $|\mathbf{k}_d| = |\mathbf{k}_i| = |\mathbf{k}| = 1/\lambda$, and since λ is very small in electron diffraction, the Ewald sphere is very large and can be considered as a plane over local regions. Furthermore, since TEM specimens are thin, the reciprocal lattice points are elongated along the direction parallel to the beam direction, giving them a rod shape and the nickname *relrods* (short for reciprocal lattice rods). Because of these effects, diffraction conditions will be fulfilled over an extended area in reciprocal space, giving rise to a two-dimensional electron diffraction spot pattern on the detector. The Ewald sphere is usually drawn, such that \mathbf{k}_i points at the 000 reciprocal lattice point. The plane containing this point is known as the zeroth-order Laue zone (ZOLZ). The planes which are parallel to the ZOLZ, but does not contain 000 are known as higher-order Laue zone (HOLZ). Diffraction resulting from \mathbf{k}_d intersecting the HOLZ provides information on the crystal structure in a direction parallel to the incoming electron beam.

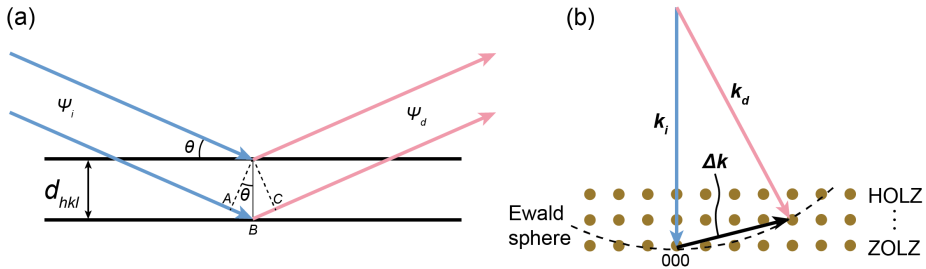


Figure 2.2.3 (a) Schematic description of Bragg's law for an incident wave Ψ_i , which is reflected off adjacent crystal lattice planes and changes direction to Ψ_d in an elastic scattering event. The distance between the lattice planes is d_{hkl} , the wave is incident at the lattice planes by an angle θ , and a path difference of length ABC is indicated. (b) Schematic description of the Laue condition, imposed on a set of reciprocal lattice points, with parts of the Ewald sphere shown with a dashed line. Also indicated are the ZOLZ and HOLZ.

A simple cubic lattice will give rise to diffracted intensity for all hkl values of \mathbf{g}_{hkl} , however more complicated crystal structures give rise to selection rules which can be calculated by utilizing the structure factor F_{hkl} . Firstly, in the kinematical approximation, the intensity

(I) in a diffraction pattern is given by:

$$I = |F_{hkl}|^2, \quad (2.2.8)$$

where F_{hkl} is given by:

$$F_{hkl} = \sum_j f_j e^{-2\pi i(hx_j + ky_j + lz_j)}. \quad (2.2.9)$$

The sum extends over all the atoms in a primitive unit cell and f_j is the atomic scattering factor for the atoms of type j .

Table 2.2.1: The atomic positions of the different elements in the perovskite unit cell.

Species	Position in unit cell
A	$(0, 0, 0)$
B	$(\frac{1}{2}, \frac{1}{2}, \frac{1}{2})$
O	$(\frac{1}{2}, \frac{1}{2}, 0), (\frac{1}{2}, 0, \frac{1}{2}), (0, \frac{1}{2}, \frac{1}{2})$

Using a cubic perovskite with the general formula ABO_3 and atom positions given in Table 2.2.1 as an example, the structure factor is

$$F_{hkl} = f_A + f_B e^{-i\pi(h+k+l)} + f_O [e^{-i\pi(h+k)} + e^{-i\pi(h+l)} + e^{-i\pi(k+l)}]. \quad (2.2.10)$$

Assuming that $f_O \ll f_A, f_B$, since oxygen scatters electrons much more weakly than typical A and B constituents in a perovskite, the structure factor can be approximated to

$$F_{hkl} = \begin{cases} f_A - f_B, & h + k + l = 2n + 1, \\ f_A + f_B, & h + k + l = 2n. \end{cases} \quad (2.2.11)$$

This equation explains why all diffraction spots from $SrTiO_3$ with $h + k + l = 2n + 1$ are very weak, as $f_{Sr} \sim f_{Ti}$ in electron diffraction, whereas all spots are clearly visible in $BaTiO_3$, where $f_{Ba} \neq f_{Ti}$.

As previously stated, low and medium magnification imaging in the TEM is usually performed using BF or DF imaging. Here, the objective aperture is inserted into the BFP to select certain beams used for imaging. For BF imaging, the objective aperture is centred around the direct beam on the optical axis, allowing beams which have passed through the specimen without being scattered to form the image. DF imaging can be viewed as partly complementary to BF imaging, in the sense that a diffracted beam is selected using the objective aperture, and an image is produced using only the scattered electrons, e.g., the ones indicated by the brown spot in Figure 2.2.2. The names BF and

DF originate from the fact that the total intensity in the DF image is usually much lower than in the BF image, making it overall darker. There are two main contrast mechanisms governing the contrast in BF and DF images. These are known as mass-thickness and diffraction contrast, which are different types of amplitude contrast. A higher average atomic number and a larger thickness will have the same effect on the images. In case of a BF image, larger mass-thickness will cause a darker image, since more electrons are scattered away from the direct beam. Conversely, since larger mass-thickness causes more scattering, some of the scattered electrons will end up at the area in BFP which is chosen by the objective aperture and the DF will look brighter. When it comes to diffraction contrast, a specimen which is aligned with the zone axis exactly parallel to the beam direction will look darker in BF, than a specimen tilted off zone, since the specimen which is on zone fulfills Bragg's law (and the Laue condition) and scatters more electrons away from the direct beam than a specimen which is not aligned on zone. A DF image is typically made by selecting a specific Bragg reflection, meaning that all areas of the specimen which scatter highly to that reflection will "light up" in the image. This can i.e. be used to study the grain structure of a material, since only certain grains will scatter to the selected Bragg reflection.

2.2.5 Convergent-beam electron diffraction

If diffraction is performed with a convergent beam instead of a parallel one, the technique is known as convergent-beam electron diffraction (CBED). Instead of spots, disks are formed in the BFP, as shown in Figure 2.2.4(a). The radius of the disk is determined by the semi-convergence angle α of the incoming beam. The distances and angles between the disks can be determined from Bragg's law, but a correct description of the intensity is only possible using dynamical diffraction theory. One advantage of CBED compared to SAD is that the probe used to form the diffraction pattern is truly nanosized, with a diameter in the order of around 1 nm and down to possibly $< \text{\AA}$ in aberration-corrected microscopes. Whereas SAD patterns include crystallographic information from areas with diameter of a few hundred nm at the least. Furthermore, Friedel's law, which holds under kinematical diffraction states that the intensity in reflection hkl equals the intensity in reflection $\bar{h}\bar{k}\bar{l}$. This typically holds in a SAD pattern, while it does not hold for a CBED pattern. CBED can thus be used to obtain three-dimensional information, like the existence of a 3-fold rotation axis, which would look 6-fold in a SAD pattern. Additionally, CBED is very sensitive to the existence of a polar axis. This is illustrated in Figure 2.2.4(b) for BaTiO₃, where the polar axis breaks the mirror symmetry m_2 [15]. Shao and Zuo [15] also utilized scanning CBED to obtain a four-dimensional data set providing a CBED pattern for each probe position across 24×50 nm in real space. Combined with diffraction pattern simulations, the experimentally observed CBED patterns demonstrated nanoscale

symmetry fluctuations consistent with the prediction of an order-disorder transition in BaTiO_3 , while the highest observed symmetry is consistent with a displacive model of the tetragonal ferroelectric phase in BaTiO_3 . This provides further experimental observations for the coexistence of order-disorder and displacive character in BaTiO_3 , as suggested by Stern [29] and mentioned in section 2.1.2. Scanning CBED was recently also used to determine the crystal structure of a strained BaTiO_3 film, where coexistence of a tetragonal and an orthorhombic symmetry in addition to a low symmetry bridging state was resolved [66]. The authors propose that this induce a continuous polarization rotation which causes the giant temperature independent dielectric response. Since the strained film cannot be considered a polycrystal and not a single crystal, the term “transitional ferroelectric” was coined to describe the strained ferroelectric film [66]. Other information that can be obtained by CBED is thickness measurements of crystalline specimens, and structure factor determination. In addition, CBED can be used to determine the space group symmetry of a specimen.

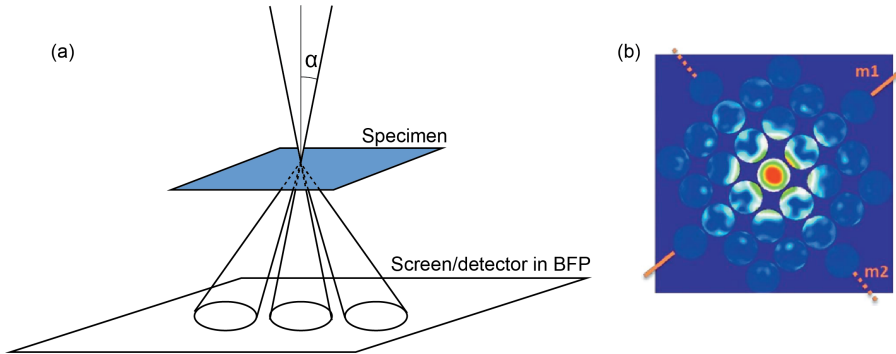


Figure 2.2.4 (a) Illustration of illumination with a convergent beam which results in diffraction disks, where α is the semi-convergence angle of the incoming beam. (b) CBED pattern from BaTiO_3 , where m_2 is broken because of the presence of a polar axis. Reproduced from [15] with permission of the International Union of Crystallography.

The procedure of structure determination is presented in the work by Eades in [67], which builds (amongst others) on ideas first formulated by Buxton *et al.* [68] and the work done by Tanaka *et al.* [69]. A description of symmetry determination by CBED is also presented in Zuo and Spence’s monograph [10], where the authors point out that in the practical approach to structure determination, something is usually known about the crystal. In addition, the procedure requires a combination of shortcuts, simple reasoning, and experience. In practice, structure determination can be done by taking CBED patterns from 3-6 major zone axes. By doing so, the symmetry elements present in these patterns can be defined and by using the tables by Tanaka [69], the point group and space group can be elucidated. The following introduction to structure determination is based on [10, 67, 69], and describes the procedure for zone axis patterns.

An important aspect of a diffraction experiment is that the symmetry of the diffraction pattern is determined by the combined symmetry of the crystal structure, the symmetry of electron diffraction itself, and the symmetry of the specimen. Even though TEM specimens are thin, their thicknesses are usually sufficiently larger than the size of a unit cell, so that effects caused by a finite specimen size can be neglected. Knowing the symmetry of the electron diffraction itself, the symmetry related to the crystal structure can be determined from the diffraction pattern. For example, a mirror plane perpendicular to the beam can be a symmetry operation of electron diffraction, because of the reciprocity theorem which states that the wave equation is invariant under the transformation $(\mathbf{r}, \mathbf{k}) \rightarrow (\mathbf{r}, -\mathbf{k})$. The symmetry of the experiment is also dependent on the direction of the crystal. Taking all these factors into account it turns out that there are 31 different possible symmetries for a diffraction experiment on a crystal. These are known as the “diffraction groups”. Depending on the orientation of the crystal, each crystal symmetry is associated with several diffraction groups.

CBED patterns can only possess two-dimensional symmetry elements, being a two-dimensional recording, however, since the 000-disk, does not necessarily contain the same symmetry as the pattern as a whole, one CBED pattern can contain two two-dimensional symmetries. CBED patterns contain information from the ZOLZ and HOLZ. If the intensity in the CBED pattern is dominated by ZOLZ reflections, the HOLZ diffraction may be neglected and the symmetry from the crystal will appear as if the crystal were a two-dimensional object and not three-dimensional one. In this case, the symmetry of the experiment is known as “projection diffraction group”. Even though a single CBED pattern can contain multiple symmetries which can provide information about the crystal symmetry, it is most convenient to obtain diffraction patterns from multiple zone axes, and use a method of elimination to determine point group based on the observed diffraction groups and projection diffraction groups. Table 11.6 in the work by Zuo and Spence [10] (which is essentially the same as Table 2 in the original work by Buxton *et al.* [68]) provides an overview of the observed two-dimensional symmetry elements in a CBED pattern, and their relation to the possible diffraction and projection diffraction groups. The point group of the crystal can be determined from the knowledge of which diffraction and projection diffraction groups are formed in the experiment.

The next step of the structure determination is to uncover the space group, of which there are 230. Essentially, the space group determination consists of deciding which of the rotation axes in the point group are screw axes in the crystal, and which of the mirror planes in the point group are glide planes in the crystal. In kinematical diffraction, screw axes and glide planes give rise to forbidden reflections, however, since the diffraction in CBED is dynamical, there can still be intensity in the disks. If a glide plane or screw axis is present in the crystal they can give rise to Gjønnes-Moodie (GM) lines [70]. The

GM lines are dark bands which extend across the entire width of the diffraction disks. Furthermore, they occur in every other disk along a row. The reason for the dynamical extinction is that two double diffraction routes exist which give rise to the intensity in the kinematically forbidden disks. The two routes have equal amplitude but opposite phase, causing the extinction. The result is intensity in the CBED disk, but at certain positions within the disk, along the symmetry lines, there is no intensity. The GM lines occur if there is a two-fold screw axis along the row of GM lines, or if there is a glide plane oriented such that it contains both the direction of the zone axis and the row of GM lines, or if both a screw axis and a glide plane, which give rise to GM lines, are present. Again, practically, CBED patterns obtained from different zone axes can be acquired and tables presented in, for example, the work by Tanaka [69] can be used to determine the space group by methods of elimination, looking at the presence of GM lines in different zone axis patterns. A diffraction pattern including the HOLZ reflection ring can also aid in the structure determination, since the unit cell centering can be determined based on how the reflections in the HOLZ line up with the ones in the ZOLZ [1].

2.2.6 Scanning transmission electron microscopy imaging

In scanning transmission electron microscopy (STEM), a convergent probe is raster scanned across the specimen. Conventionally, different detectors are used to acquire one value of intensity for each probe position, creating an image with the same dimension as the number of probe positions which were scanned. Two different detectors are shown in Figure 2.2.5, known as the BF and annular dark-field (ADF) detectors. As illustrated in Figure 2.2.5, the detectors are defined by certain collection angles. The BF detector collects the forward scattered electrons up to an angle θ_1 , whereas the ADF detector is an annular detector characterized by an inner and outer collection angle (θ_2 and θ_3).

The contrast in a BF-STEM image is similar to the one in BF-TEM. However, it is prone to scan noise and larger sample drift since STEM images require longer acquisition times because of the serial acquisition method. Hence, the technique is not the most useful. ADF-STEM, on the other hand, is very useful, especially when a large angle θ_2 is used, known as high-angle annular dark-field STEM (HAADF-STEM). In the case of HAADF-STEM, the contrast is dominated by incoherent Rutherford scattering which scales approximately with Z^2 (where Z = atomic number), meaning that the heavier the atom is, the brighter it looks in the image. More details on STEM image formation and interpretation is described, for example, by Nellist and Pennycook [71].

The introduction of aberration correctors has made sub-ångström resolution routine in both TEM and STEM, making it possible to obtain atomic resolution in most thin and crystalline specimens. Due to this development it has become of interest

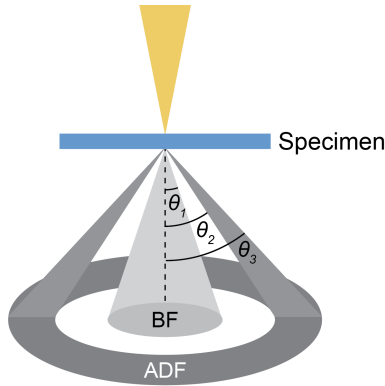


Figure 2.2.5 Schematic of the STEM setup. A convergent beam is raster scanned across the specimen and the transmitted signal is recorded on a BF and an ADF detector. The outer collection angle of the BF detector is given by θ_1 , and the inner and outer collection angles of the ADF detector are given by θ_2 and θ_3 , respectively.

to study atomic positions in high-resolution HAADF-STEM images. Yankovich *et al.* have demonstrated that it is possible to obtain the positions of heavy elements with sub-picometer precision based on non-rigid registration and averaging of an image series [72]. This method is utilized to study the local structure of multiple ferroic materials. For example, Jia *et al.* provided experimental evidence for continuous rotation of dipoles closing the flux of 180° domains in a ferroelectric perovskite thin film [73]. Furthermore, in super lattices of $\text{SrTiO}_3/\text{PbTiO}_3$ and $\text{SrRuO}_3/\text{PbTiO}_3$ topological spin structures forming vortex-antivortex structures of electrical dipoles have been observed [12, 74]. This is reminiscent of the complex topological spin structures found in ferromagnetic materials, thus a blurring of the border between emergent topologies in ferromagnetic and ferroelectric materials is demonstrated [74]. The observation of minor cation displacements have also been observed in BaTiO_3 . Despite the lower c/a ratio in BaTiO_3 ($c/a = 1.01$) compared to PbTiO_3 ($c/a = 1.06$), Kobayashi *et al.* demonstrated the presence of multiphase nanodomains in a strained BaTiO_3 film [11]. Li *et al.* studied the effect of Sm-doping in $\text{Pb}(\text{Mg}_{1/3}\text{Nb}_{2/3})\text{O}_3\text{-PbTiO}_3$, and in addition to precise determination of atomic positions, the atom column intensities were used to determine that the Sm-doping causes a structural heterogeneity which enhances the giant piezoelectric properties of the material [13]. Functional materials, like ferroelectrics, typically have a complex oxide structure, therefore it is of interest to study the O atom positions, in addition to the heavy cation positions. However, the scattering power of O is so weak compared to the cations that it is invisible in HAADF-STEM images. Acquiring so-called annular BF images, using smaller θ_2 and θ_3 angles than in HAADF-STEM images makes it possible to obtain contrast from O atom columns. In this image mode, the contrast is related to the elastic forward scattering, which in turn can cause artificial

displacements between O atom columns and cation atom columns at very small mistilt angles. The artifact is further dependent on the specimen thickness, defocus, convergence angle, and uncorrected aberration [75], so care should be taken when using this technique.

Nowadays, the development within TEM analysis is made by the introduction of novel detectors and access to the computing power to analyze the acquired data. By using a segmented STEM detector, differential phase contrast (DPC) imaging can be performed. The deflection of the electron probe caused by the specimen can be measured by investigating the difference in intensity falling on the different segments of the detector. By applying integrated DPC it has been demonstrated that it is possible to resolve H atom columns besides a Ti atom column [76]. The method was further applied to study reversible oxygen migration in a hafnia-based ferroelectric device during an *in situ* biasing experiment in the TEM [77]. As mentioned, direct electron detectors are also becoming important in TEM analysis. The technique utilizing a direct electron detector is known as four-dimensional STEM, since a four-dimensional data set is acquired, i.e., a two-dimensional diffraction pattern for each probe position (x, y) at the specimen surface. Having acquired all the electrons scattered up to a certain angle (and not only one value of intensity from the BF or ADF detector) makes it possible to extract more information than in conventional BF- or HAADF-STEM imaging. This technique has for example recently been used to image the interfacial charge distribution and ferroelectric polarization with sub-ångström resolution in a SrTiO₃/BiFeO₃ heterojunction [78].

2.2.7 Image simulation

Because of the strong interaction between the electron beam and the specimen, causing multiple scattering events to occur, there is no simple relation between the specimen structure and the image. Image simulations thus provide an important tool to extract information by comparing experimental images to simulations. Two different simulation approaches exist, the Bloch wave method and the multislice method. The monograph by Kirkland [79] provides a description of both methods. Here, only the principles of the multislice method will be presented (based on [79]), since it was the method applied in this work.

The multislice method can handle a wide range of specimens, from amorphous to crystalline materials with a large unit cell, in addition to defects and interfaces. The principle of the multislice method is to solve the Schrödinger equation by slicing the specimen into many thin layers along the beam direction, such that each layer acts as a simple phase object. Since the electrons in the beam have a high energy, and the specimen's effect on the beam electrons can be considered as a relatively minor perturbation on the electron motion, it is useful to separate the large velocity in the

z direction from other small effects due to the specimen. The full wave function ψ_f can thus be factored into two parts:

$$\psi_f(x, y, z) = \psi(x, y, z)e^{2\pi iz/\lambda}. \quad (2.2.12)$$

$\psi(x, y, z)$ varies slowly with z , and $e^{2\pi iz/\lambda}$ is a plane wave travelling in the z direction. The expression for ψ_f can then be inserted into the Schrödinger equation and solved for the slowly varying part of the wave function ψ . Furthermore, the simulation is set up such that the wave function is transmitted through a slice at position z_n along the beam direction, to which the potential of that slice is projected. The wave function is then propagated through free space a distance Δz , as indicated in Figure 2.2.6. The incoming

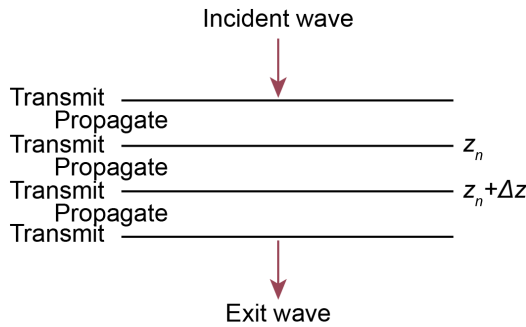


Figure 2.2.6 Schematic overview of the multislice method showing the incident wave, and the transmission and propagation operations which are performed for each slice. All the atoms within z_n to $z_n + \Delta z$ are compressed into a flat slice at z_n . After the interaction with the specimen, an exit wave is calculated. The figure is inspired by [79].

wave function ψ_0 can be a plane wave if a parallel beam mode is to be simulated, or a probe wave function for CBED and STEM simulations. If each slice is labelled $n = 0, 1, 2, \dots$, the wave function at the top of each slice is labelled $\psi_n(x, y)$, and the wave function at the top of the next slice $n + 1$ can be written in a compact form as

$$\psi_{n+1}(x, y) = p_n(x, y, \Delta z_n) \otimes [t_n(x, y)\psi_n(x, y)] + \mathcal{O}(\Delta z^2), \quad (2.2.13)$$

where $p_n(x, y, \Delta z_n)$ and $t_n(x, y)$ are the propagator and transmission function at each slice, respectively. The last term in Equation (2.2.13) is called the error term and indicates the order of magnitude of the errors caused by the approximations used. The number of slices n can be chosen to simulate a specimen of the desired thickness, in which calculations using Equation (2.2.13) is repeated n times. In a HAADF-STEM simulation, the image is constructed by integrating the intensity, given as the modulus square of the wave function, over the angular range corresponding to the annular detector.

For each slice in the multislice method, two operations must be performed. First the

multiplication with the transmission function, then the convolution with the propagator function. Since a convolution in real space is a multiplication in reciprocal or Fourier space, the fast Fourier transform (FFT) is usually applied, since it provides computational efficiency. To be able to use the FFT, the image must be discretely sampled for the wave function, which can cause problems with aliasing. A convenient way to avoid aliasing is to limit the transmission and propagation function to be zero outside $\frac{2}{3}k_{\max}$, where k_{\max} is the maximum sampling frequency in the wave function.

2.2.8 Energy-dispersive X-ray spectroscopy

Energy-dispersive X-ray spectroscopy (EDS) utilizes the X-rays created in the specimen by inelastic scattering of the electron beam. When electrons interact inelastically with the specimen, it gives rise to two types of X-ray radiation: Bremsstrahlung and characteristic X-rays. The Bremsstrahlung is created by the interaction between the beam electron and the Coulomb field surrounding the atom nucleus in the specimen, which has an effective positive charge. The beam electron is slowed down by the interaction with the nucleus and loses a certain energy ΔE . As a result, a photon with energy $\Delta E = h\nu$ is emitted, where h is Planck's constant and ν is the frequency of the photon. This interaction can give rise to X-rays with any energy up to the initial energy of the beam electron, however low energy photons (< 2 keV) are usually absorbed before they are detected. Furthermore, the Bremsstrahlung is emitted mainly in the forward scattering direction, meaning that most of it radiates downwards below the specimen. Bremsstrahlung is usually considered as unwanted background radiation in EDS analysis. Characteristic X-rays are generated via an interaction between the beam electron and the electrons in the specimen through the excitation of a core-shell specimen electron by the beam. An electron from an outer shell will then relax and fill the vacancy created by the excited electron, and a photon with energy E_γ will be emitted, where $E_\gamma = E_K - E_L$ if an electron from the L -shell filled the K -shell vacancy. The energy of the emitted photons relates to the possible electron energy levels in the specimen, which have sharply defined energies. Since inner-shell energy levels increase monotonically with the atomic number Z , detection of a photon with a specific energy can be used as an unambiguous sign of the presence of an element in the specimen. Or said in other words, the characteristic X-rays work as fingerprints for the different elements. For each element multiple transitions are possible as shown in Figure 2.2.7.

The Siegbahn designation system is used to name each X-ray line [81]. The designation system has a set of conventions, but is not 100% systematic. In general a specific X-ray is named by the element it comes from, then all transitions to the K -shell give rise to K -lines, transitions to the L -shells give rise to L -lines, and so on. To distinguish between the origin of the deexcited electron, the Greek letters α and β are added after the K, L, \dots ,

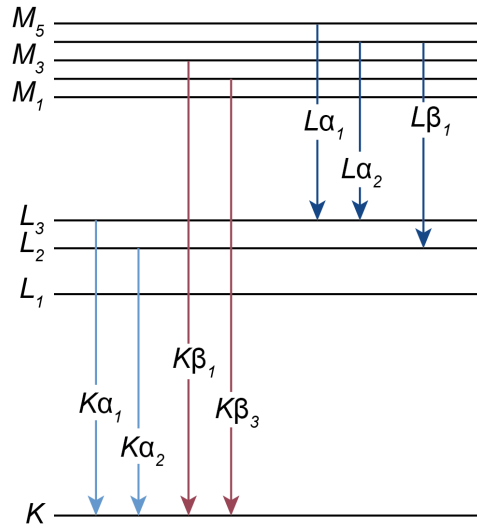


Figure 2.2.7 Illustration of the energy levels of the innermost electron shells and the nomenclature used for different characteristic X-rays based on the origin of the deexcited electron causing the characteristic X-ray. The figure is inspired by [80].

in addition to a number to denote a particular line as shown in Figure 2.2.7. The α_1 line is usually the strongest in a series, and the β_1 is usually the second strongest, except that $K\alpha_2$ is stronger than $K\beta_1$. A comprehensive list of characteristic X-rays, their names, and energies are presented in the “X-ray data booklet” from Lawrence Berkeley National Laboratory [80].

The concentration of different elements in a specimen can be determined by quantitative EDS analysis. A simple approach is suggested by Cliff and Lorimer [82]:

$$\frac{C_A}{C_B} = k_{AB} \frac{I_A}{I_B}, \quad (2.2.14)$$

where C_A and C_B are the concentrations of elements A and B , and I_A and I_B are the measured characteristic X-ray intensities originating from elements A and B , respectively. The factor k_{AB} is a sensitivity factor which depends on the specific TEM system used and the high-voltage used. Assuming that the specimen only contains elements A and B , the following relation holds:

$$C_A + C_B = 100\%. \quad (2.2.15)$$

Equation (2.2.14) and Equation (2.2.15) can thus be used to calculate the unknown concentrations. The k_{AB} -factor ignores absorption and fluorescence effects and can therefore potentially be the cause of large error in the quantification. A more sophisticated method which seeks to correct for some of the faults of the Cliff-Lorimer (CL) method is

the ζ -method described in detail by Watanabe [67]. An important part of the ζ -method is to correct locally for mass-thickness effects by measuring the exact electron dose which the specimen is irradiated by. This can be found through accurate measurements of the beam current.

Aberration correctors have played an important role in chemical mapping by both EDS and EELS, since the aberration correctors provide an ångström-sized probe with a higher current than was previously possible. In the case of chemical mapping by EDS, Lu *et al.* demonstrated atomically resolved EDS-maps from SrTiO₃, and proved that the Sm-dopant in SrTiO₃ mainly occupy the A-sites substitutionally [83]. Wenner *et al.* demonstrated atomic resolution EDS-maps of ordered precipitates in Al-alloys [84], and Iijima *et al.* studied cation ordering in Ti-Nb oxide crystals at an atomic scale using EDS [85].

2.2.9 Electron energy-loss spectroscopy

Electron energy-loss spectroscopy (EELS) is described in detail in the monograph [86] and review [87] by Egerton. EELS is a technique which can be used to determine many different properties of a specimen, ranging from plasmon spectroscopy which can provide information about mechanical and electronic properties (such as bandgap), to chemical mapping and thickness measurements. In addition, the fine structure can be used to study the electronic densities of states in a material. In this work, EELS was only used for compositional mapping, so this section will be limited to the description of elemental analysis using EELS based on the review by Egerton [87].

EELS utilizes the information obtained from measuring the energy loss of the electrons which have been transmitted through the specimen. To measure this energy loss, a magnetic prism is placed at the end of the TEM column, as shown in Figure 2.2.1. The magnetic field of the prism will change the trajectory of the electrons according to the Lorentz force, making the electrons follow a circular path with radius R depending on their speed, and therefore energy, such that

$$R = \frac{mv}{Be}, \quad (2.2.16)$$

where m , v and e are the electron relativistic mass, speed, and charge. The magnetic field B is usually in the order of 0.01 T. A typical energy resolution in EELS is around 1 eV for microscopes without an electron beam monochromator. In the microscopes without monochromators, the energy resolution depends mainly on the type of electron source, where the thermionic sources have larger energy spread than a FEG. For microscopes equipped with a monochromator, the energy resolution can vary from a few meV to 0.2 eV,

depending on the type of monochromator. Most of the electrons which are transmitted through the specimen are scattered elastically, meaning that they lose no energy. This gives rise to a very intense zero-loss peak (ZLP) in the EEL spectra. It is therefore common to acquire two EEL spectra simultaneously, known as the low-loss spectrum and the high-loss spectrum. The low-loss spectrum contains the ZLP, which has a typical width of 0.2-2 eV mainly reflecting the energy distribution in the electron source, and the plasmon peak, resulting from a plasma resonance of the valence electrons. The plasmon peak is also fairly intense, depending on the specimen thickness. The high-loss spectrum contains the ionization edges, which results from the excitation of core-shell electrons. The ionization edges have a characteristic shape, with a rapid rise followed by a more gradual fall, in addition they are often relatively low in intensity compared to the background signal. The overall intensity of the high-loss signal decays rapidly with increasing energy loss, reaching negligible levels above ~ 2 keV, which defines the commonly used energy limit of the technique. Although, there are examples of high-loss EELS in the range of 2-10 keV [88].

Like in EDS, each ionization edge in EELS occur at an energy loss that is characteristic of a particular element, thus EELS can be used to identify the elements present in the specimen. Although the angular distribution of scattering is a mixture of elastic, plasmon, and plural scattering, the areal density of an element (N atoms per unit area) can be estimated from the formula:

$$I_c(\beta, \Delta) \approx NI_1(\beta, \Delta)\sigma(\beta, \Delta). \quad (2.2.17)$$

Here, $I_c(\beta, \Delta)$ is shown in Figure 2.2.8, and is defined as the intensity over an energy range Δ beyond a threshold for the onset of the ionization edge. As can be seen in Figure 2.2.8, it is important to extrapolate and subtract the background precisely, which can be difficult if two ionization edges are separated by less than 50 eV. $I_1(\beta, \Delta)$ represents an integral of the low-loss spectrum up to an energy loss Δ , including the entire ZLP. The last term in the expression is $\sigma(\beta, \Delta)$. This is a partial cross section, calculated for core-loss scattering up to an angle β , the collection semi-angle of the spectrum, and energy range Δ beyond the threshold. For K -shells, this cross section is available from the hydrogenic model, and for other shells, Hartree-Slater calculations or experimental measurements are used. Given that the thickness, t , of the specimen is known, the concentration can be calculated via $n = N/t$. Equation (2.2.17) provides an absolute quantification, however, an elemental ratio (n_A/n_B) is often more useful, since t and I_1 then cancels out.

EDS and EELS can be viewed as two complementary techniques, especially in terms of elemental analysis. Light elements cause low electron energy-loss and hence generate signal at an energy which result in high intensity ionization edges in EEL spectra, oppositely heavier elements generate more characteristic X-rays for EDS analysis. Taking

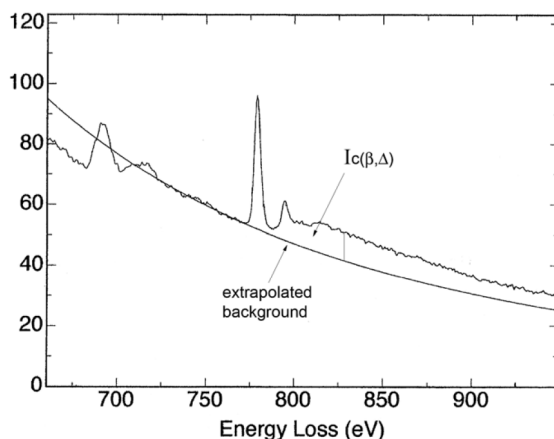


Figure 2.2.8 A high-loss spectrum showing the $I_c(\beta, \Delta)$ ionization edge, above background. Republished with permission of IOP Publishing, Ltd, from *Electron energy-loss spectroscopy in the TEM*, R. F. Egerton, 72, 1, 2008; permission conveyed through Copyright Clearance Center, Inc.

BaTiO₃ as an example, EELS is more suitable for chemical mapping, since the edges from Ba, Ti and O have intense edges at 781, 456, and 532 eV energy loss, respectively. Whereas, BaL α and TiK α suffer from severe peak overlap in EDS due to the low energy resolution of the technique, making quantitative analysis challenging.

2.3 Focused ion beam

2.3.1 Basic principles

Focused ion beam (FIB) served as an important tool for TEM specimen preparation. Here, the basic working principles of the FIB will be presented based on the monograph edited by Nan Yao [89].

The FIB, which was commercialized in the 1980s and originally geared towards the semiconductor industry, has become an important tool in many fields of nanotechnology because of its ability to manipulate and characterize many types of materials at the nanometre scale. The development of the technique was largely driven by the need to remove atoms from a lattice effectively. The FIB does this by creating a beam of high-energy ionized atoms of a relatively massive element. Typically Ga⁺ ions are used. The FIB has four basic functions: Milling, deposition, implantation, and imaging. The collision between the ions and the atoms in the sample can be elastic or inelastic. The result of the elastic collision with the sample is an excavation of the surface atoms, known as either sputtering or milling. In an inelastic collision, either secondary electrons can

be emitted from the surface or secondary ions can be created. Images can be produced by detecting these electrons or ions. To deposit material on the surface of a sample, a precursor gas containing the desired deposition material and volatile components like oxygen and hydrogen are introduced through a gas nozzle close to the surface. The gas molecules are adsorbed on the surface and decomposed into the non-volatile and volatile products by the high-energy ion beam. Secondary electrons, created by either the ion beam or the electron beam also contribute significantly to the deposition process. The non-volatile products remain bonded to the surface where the beam scanned the sample, while the volatile components leave the surface. In addition to assisting the deposition, the ion beam will cause simultaneous sputtering and implantation of the surface (protection layers created by ion beam assisted deposition therefore contain large amounts of Ga). Tuning the current used, in addition to other beam parameters like positional overlap and dwell time is therefore important to promote the desired process.

The interaction between the ion beam and sample causes many secondary processes which result in various phenomena, e.g. interdiffusion of constituent elements, amorphization, track formation, and permanent damage. To mitigate these issues, and utilize the even higher resolution capabilities of electrons, modern FIBs consist of a dual-beam system, essentially combining a scanning electron microscope (SEM) and FIB in the same instrument as shown in Figure 2.3.1. The SEM is in many ways similar to STEM, however, the acceleration voltages used are typically in the range of 0.2-30 kV. In addition, bulk samples are used, such that backscattered or secondary electrons, which leave the upper sample surface, are used for image formation instead of the transmitted electrons. The dual-beam FIB is an instrument which exploits the best of both worlds in terms of the nanomachining capabilities of the FIB and the much less invasive electron beam which can be used for high resolution imaging without simultaneously damaging the sample. When it comes to the properties of the electron beam and the ion beam, they can both form nanometre-sized probes, depending on potential and current used. The interaction volumes for electrons and Ga^+ are very different. As an example, electrons penetrate to depths of about 1800 and 25 nm in iron at beam voltages of 30 and 2 kV, respectively, while the Ga^+ penetrate to depths of about 20 and 4 nm at the same beam voltages. The electron beam can also be used to deposit material on the sample surface from a precursor gas in the same manner as the ion beam, albeit at a much slower rate. As indicated in Figure 2.3.1, the electron column and ion column are usually positioned with a 52° angle between them, hence the sample stage has to be tilted to 52° for the ion beam to be incident parallel to the surface normal. Also depicted in Figure 2.3.1 is the gas injection nozzle and a lift-out needle. The lift-out needle can be used to move pieces of a sample from one body to another, for example in the process of making a TEM specimen, it is used to lift a lamella, which is cut out of the sample, to a TEM grid which fits in the TEM holder.

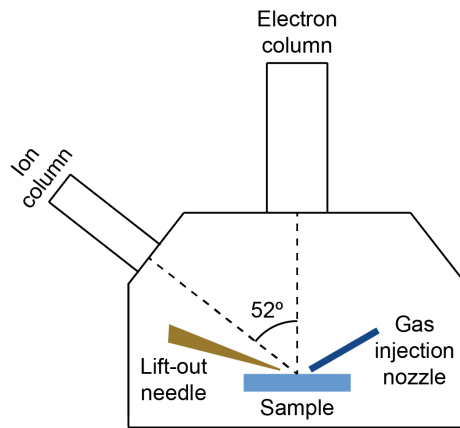


Figure 2.3.1 Schematic of the dual-beam FIB indicating the position of the electron column and ion column positioned 52° apart. Also shown is the gas injection nozzle used for materials deposition and the lift-out needle. The figure is inspired by [89] and the set-up of the FEI Helios G4 at NTNU Nanolab.

Experimental details

3.1 Materials

3.1.1 Barium titanate films on strontium titanate substrates

The investigated BaTiO₃ films were prepared by aqueous CSD by Trygve M. Ræder as described in [41], and spin coated onto (100), (110), and (111) oriented SrTiO₃ substrates. The films were heated from ambient temperature to 450 °C, 550 °C and 1000 °C, with heating rates of 100 °C/min, 50 °C/min, and 20 °C/s, respectively. The hold time at 1000 °C was 5 min, and the process was repeated eight times to reach the desired film thickness. Interdigitated electrodes (5 nm Ti and 20 nm Pt) were deposited on the films to measure the in-plane properties as described in [90].

3.1.2 Bismuth containing tetragonal tungsten bronzes

$A_4\text{Bi}_2\text{Nb}_{10}\text{O}_{30}$, $A = \text{K or Rb}$ (KBN or RBN) ceramics were prepared via a two-step solid-state synthesis route by Caren R. Zeiger. The precursor powders were dried at 120 °C overnight prior to weighing as well as before uniaxial pressing of pellets, except A_2CO_3 , which was dried at 200 °C before weighing due to their hygroscopic nature. The heating and cooling rates for heat treatments were 200 °C/h if not stated otherwise. The first step comprised synthesis of the alkali niobates ANbO_3 and bismuth niobate BiNbO_4 . The potassium carbonate (K_2CO_3 , Sigma Aldrich BioXtra) or rubidium carbonate (Rb_2CO_3 , Sigma Aldrich) and niobium oxide (Nb_2O_5 , Sigma Aldrich) were weighed out in a 1:1 molar ratio to prepare the alkali niobates. BiNbO_4 was prepared from a 1:1 stoichiometric ratio of bismuth oxide (Bi_2O_3 , Sigma Aldrich) and Nb_2O_5 . The powder mixtures were ball milled for 2 h in ethanol (isopropanol in case of RbNbO_3 ; 1 h for BiNbO_4) before the solvent was removed via rotary evaporation. The powder mixes were then uniaxially pressed into pellets of 15 mm diameter and thicknesses below 4 mm using a pressure of about 40 MPa. The pellets were stacked inside a crucible with a lid and the ANbO_3 pellets were calcined at 700 °C for 4 h before the temperature was increased to 900 °C and kept at this temperature for another 12 h. The BiNbO_4 pellets were calcined for 2 h at 800 °C. The calcined pellets were crushed to powders by a mortar and stored in a desiccator for further processing. KBN and RBN were made in the second step by mixing

ANbO_3 , BiNbO_4 , and Nb_2O_5 in a 4:2:2 stoichiometric fashion. The resulting powder mixture was ball milled for 24 h in ethanol and subsequently dried by rotary evaporation. The powder was pressed into pellets of 10 mm diameter and less than 4 mm thickness using a uniaxial press with about 60 MPa. The pellets were then packed into sacrificial powder inside a crucible closed with a lid and the compounds were sintered at 1150 °C. The sintering time was 1 h for KBN and 8 h for RBN, with a heating rate of 400 °C/h. The sintered pellets were polished to remove any non-stoichiometric phases that might have formed on the surface due to volatility of the alkali cations. TEM specimens of KBN and RBN were prepared by crushing and grinding the pellets using a carbide mortar. The particles were then dispersed in isopropanol and dropped onto a Cu grid coated with a holey amorphous carbon film.

3.1.3 Barium containing tetragonal tungsten bronzes

$\text{Ba}_4\text{M}_2\text{Nb}_{10}\text{O}_{30}$, $M = \text{Na, K, or Rb}$ (BNN, BKN, or BRN) ceramics were synthesized using BaCO_3 (99+%, ThermoFisher), Nb_2O_5 (>99.99%) and either Na_2CO_3 ($\geq 99.0\%$), K_2CO_3 ($\geq 99.0\%$), or Rb_2CO_3 (99%) respectively, as precursors (Sigma-Aldrich). The barium containing TTBs were prepared by Nora S. Løndal. To avoid extensive loss of the highly volatile alkali cations at high temperature, MNbO_3 was first prepared by mixing in ethanol by ball milling, drying, uniaxial pressing at approximately 30 MPa and calcination first at 700 °C for 4 h before further calcination at 900 °C for 12 h. BaNb_2O_3 was prepared in the same manner with calcination at 1100 °C for 6 h. NaNbO_3 was mixed with BaNb_2O_3 in ethanol by ball milling, dried, pressed to pellets at approximately 70 MPa and sintered at 1285 °C for 6 h with heating rate of 200 °C/h to make BNN. To avoid loss of alkali cations during sintering the pellets were covered by sacrificial powder of the same composition. The same procedure, with adjusted sintering parameters and mixing BaNb_2O_3 with KNbO_3 and RbNbO_3 , respectively, gave BKN (1275 °C, 6 h, 300 °C/h) and BRN (1150 °C, 2 h, 200 °C/h). The sintered pellets were polished to remove any secondary phases that might have formed on the surface due to volatility of the alkali cations. Powders were prepared by crushing and hand grinding in a carbide mortar. To make TEM specimens, the fine powder was dispersed in ethanol or isopropanol and dropped onto a Cu grid coated with a holey amorphous carbon film.

3.1.4 Gadolinium molybdate

The single crystalline $\text{Gd}_2(\text{MoO}_4)_3$ used in the TEM studies was grown by Edith Bourret and Didier Perrodin from the Lawrence Berkeley National Laboratory, USA, using the Czochralski method.

The XRD study on $\text{Gd}_2(\text{MoO}_4)_3$ was performed on powder from a solid-state synthesis.

The synthesis parameters were chosen based on conditions presented in the work by Afonso [91], who successfully synthesised both the α - and β -phase of $\text{Gd}_2(\text{MoO}_4)_3$. Single-phase β - $\text{Gd}_2(\text{MoO}_4)_3$ was obtained by drying MoO_3 (99.97% trace metals basis, Sigma Aldrich) and Gd_2O_3 (99.9% trace metals basis, Sigma Aldrich) for 5 h at 650 °C and 900 °C, respectively, and mixing stoichiometric amounts in an agate mortar with ethanol. The powder was then dried and pressed at 80 MPa into pellets with diameter of 10 mm. The pellets were sintered at 950 °C for 25 h, before crushed and finely ground in an agate mortar for the XRD analysis.

3.2 Specimen preparation by focused ion beam

3.2.1 Instrumentation

The TEM lamellae which were prepared by FIB were made using the FEI Helios G4 UX, equipped with an EasyLift EX NanoManipulator for lamella transfer. The gas injection system provides the possibility to deposit either Pt or C, through the precursor gases $(\text{CH}_3)_5\text{C}_5\text{H}_{10}\text{Pt}(\text{CH}_3)_3$ or C_{10}H_8 (naphthalene), respectively. The conventional procedure for TEM lamellae preparation is presented in the following section, and the procedure developed for *in situ* studies is presented in Section 3.2.3. The conventional procedure was used in the case of BaTiO_3 films on SrTiO_3 , and to prepare lamellae from single crystalline $\text{Gd}_2(\text{MoO}_4)_3$, and the latter material was also used in the *in situ* procedure.

3.2.2 Conventional preparation technique

The conventional TEM specimen preparation used in this work is inspired by the work of Schaffer *et al.* [92], and the procedure is demonstrated by the preparation of $\text{BaTiO}_3/\text{SrTiO}_3$ as shown in Figure 3.2.1.

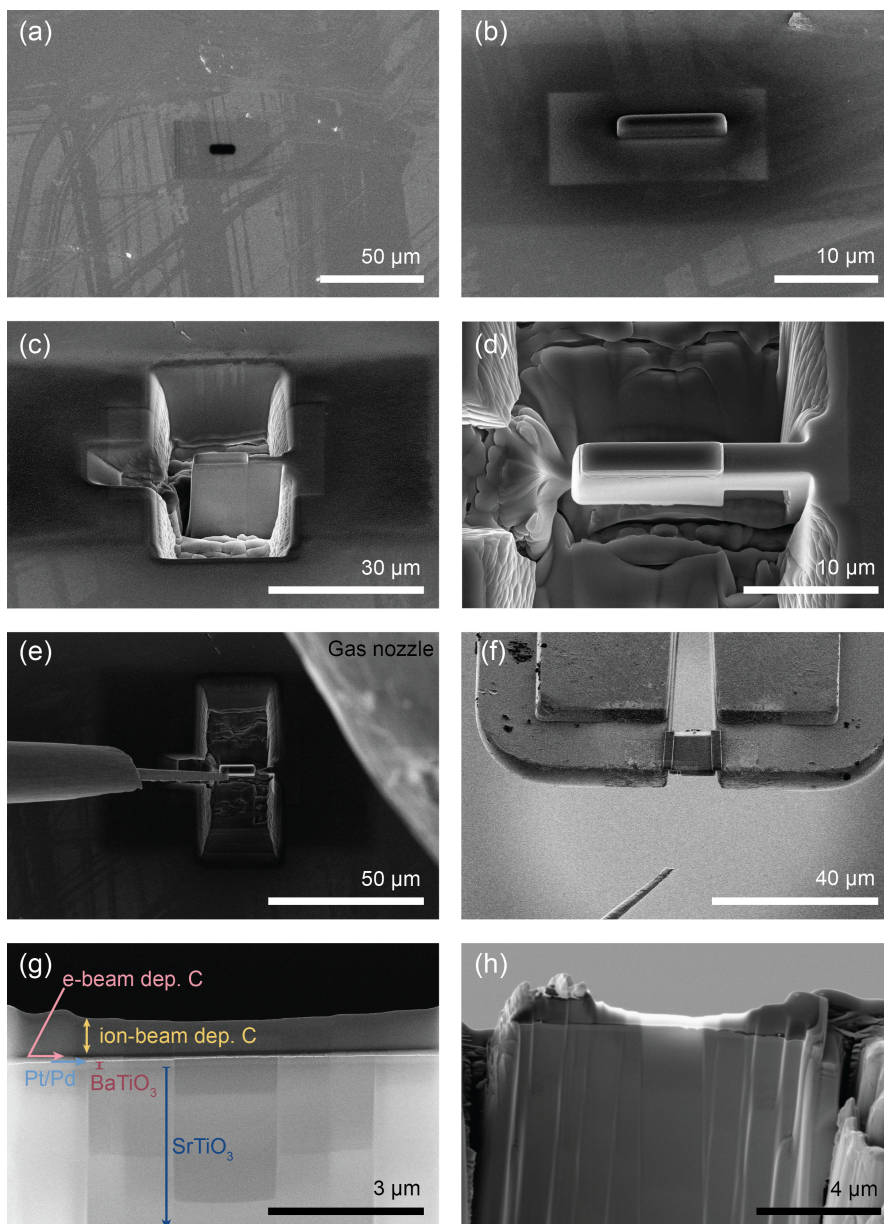


Figure 3.2.1 Images showing the conventional TEM preparation procedure. (a) First, C was deposited by the electron beam, and then (b) by the ion beam. (c) Trenches were then milled out around the lamella, and then (d) the material beneath the lamella was milled away. (e) The lamella was then mounted to the lift-out needle, and moved to (f) the TEM grid where it was fastened. (g) Shows the layers of the final lamella. (h) Is an image taken with the ICE detector. The brighter the contrast is, the thinner the lamella is.

In the case of BaTiO₃ on SrTiO₃, the most important part of the sample was the film essentially covering the surface of the substrate, meaning that it was important to protect the surface layer from damage by the Ga⁺ beam. Thus, a thin layer (~100-200 nm) of C was first deposited using the electron beam assisted deposition at 0° stage tilt, as shown in Figure 3.2.1(a). During electron beam assisted deposition secondary electrons break the atomic bonds in the naphthalene precursor gas. Low acceleration voltage in combination with a high beam current (typically 3 kV and 26 nA) was used to achieve a high flux of secondary electrons at the surface, and hence a fast deposition rate. Then, the stage was tilted to 52°, to deposit more C using the ion beam, as shown in Figure 3.2.1(b). As a rule of thumb, an ion beam current of 10 pA per μm² was used for depositing material on the sample surface, meaning that when a protection pad of 2 × 10 = 20 μm² was deposited, an ion beam of approximately 0.20 nA was desirable. As there are only a certain selection of ion beam currents available, 0.26 nA was used in this step. The final protection layer had a thickness of about 2 μm. After deposition of the protection layer, trenches were milled out around the lamella using a high ion beam current, first at 42 nA for fast milling, then at 9.1 nA for more precise milling around the lamella. The result after 9.1 nA is shown in Figure 3.2.1(c). Then, the sample stage was tilted to 7° to mill away material beneath the lamella, leaving only a thin bridge of material between the lamella and the sample, as shown in Figure 3.2.1(d).

At 0° tilt, the lift-out needle was fastened to the corner of the lamella with a thin layer of C as shown in Figure 3.2.1(e). Lastly, the thin bridge of remaining material was milled away and the lift-out needle, including the lamella, was retracted. C was chosen as the welding and protection layer material instead of Pt, which is more commonly used. There are several reasons to chose C instead of Pt. First, possible, unwanted contamination of C on the sample surface can be removed by oxygen plasma cleaning prior to the TEM analysis, whereas contamination of small Pt nanoparticles can not be removed by plasma cleaning. In addition, Pt gives a high signal in HAADF-STEM images. It is therefore desirable to avoid the high contrast Pt in the protection layer, and even more important to avoid contamination/redeposition of Pt atoms or clusters on the sample surface. Lastly, C deposited by electron beam assisted deposition can be removed by extended plasma cleaning, while C deposited by ion beam assisted deposition is almost completely stable during normal oxygen plasma cleaning.

The next step of the specimen preparation procedure was to fasten the lamella to a TEM Cu grid. Usually, a trench was milled out in the Cu grid, as shown in Figure 3.2.1(f), then the lamella was lowered down in the trench and fastened on each side by C pads. The stage tilt was at 52° when making the trench in the Cu grid, and 0° when fastening

the lamella. Lastly, the lift-out needle was cut away using the ion beam before thinning the lamella to a suitable thickness for TEM analysis. The thinning was performed in an iterative manner, using lower and lower currents and voltages to have efficient removal of material in the beginning and create a high quality specimen surface by using low currents and voltages in the final steps of the procedure. The thinning steps typically started with the ion beam at 30 kV and a current of 2.4 nA. Each side of the lamella was thinned using a relative angle between the lamella and ion beam of $\pm 2^\circ$, meaning that the stage was alternately tilted to 50° and 54° , when thinning the “top” and “bottom” side of the lamella, as seen by the ion beam image, respectively. In the initial thinning steps, the entire width of the lamella was thinned to equal thickness. However, to maintain structural stability of the lamella, only a narrow area in the middle was thinned down to 30-80 nm, depending on the TEM analysis the lamella was intended for. Further thinning at 30 kV was typically done using 0.75 nA, and 90 pA for higher precision when the lamella got thinner. At about 80-100 nm thickness, the ion beam voltage was set to 5 kV, to create a thinner surface damage layer when further thinning the lamella. Final thinning was done at 2 kV and 17 pA, and stage tilt of $\pm 3^\circ$, to minimize the amorphous layer of the TEM lamella. Final lamellae are shown in Figure 3.2.1(g) and (h). The image in Figure 3.2.1(g) is a secondary electron image acquired using an in-column TLD detector, showing how the lamella is made thinner and thinner towards the middle of the specimen. In addition, the cross section of all the layers of the lamella is shown. Starting at the bottom of the image, the SrTiO_3 substrate can be seen, then (with a very slight contrast difference) the BaTiO_3 film can (barely) be seen. The very bright line above the BaTiO_3 film is a layer of Pt/Pd, which was sputter coated on top of the macroscopic sample to improve the electrical conductivity and avoid sample charging. Then, above the Pt/Pd layer is first a dark, then a brighter layer of the deposited C protection layer. The contrast difference is caused by the difference in chemical composition between the C protection layers deposited by electron beam assisted deposition or ion beam assisted deposition, respectively. The C layer from the electron beam assisted deposition contains a significant amount of residual hydrogen from the naphthalene precursor gas, thus resulting in an overall low atomic weight material. While the ion beam assisted deposition causes significant amounts of Ga to be included in the amorphous matrix of C and hydrogen.

The Pt/Pd layer was sputtercoated on the (100) oriented BaTiO_3 film prior to the specimen preparation in the FIB. However, since the conductive layer inhibit dielectric measurements with the interdigitated electrodes, the Pt/Pd layer was not applied to the (110) and (111) oriented films. Instead, it turned out that a conductive tape fastened to the pad of the interdigitated electrodes eliminated the charging issues, while

simultaneously being removable for other experiments to be performed on the BaTiO₃ films. Figure 3.2.1(h) shows a similar image as (g), however it is taken with the side-mounted ICE detector. The ICE detector is positioned to most efficiently collect secondary electrons emitted from the “back” side of the lamella when the primary electron beam is scanned across the “front” side. As the lamella gets thinner, more and more secondary electrons are emitted from the back side depending on the combination of the acceleration voltage of the electron beam and the lamella thickness. Thus, the ICE detector can be used to *in situ* monitor the lamella thickness.

The same procedure was used for conventional preparation of Gd₂(MoO₄)₃, except that no protective layer of C was deposited using the electron beam, since a single crystal was studied, and it did not matter that the upper nanometres were irradiated by the ion beam. Furthermore, charging was a severe issue in the specimen preparation of Gd₂(MoO₄)₃ until the lamella was fastened to the TEM grid, so removing a step in the specimen preparation saved time. The Gd₂(MoO₄)₃ single crystals were not sputtercoated with a conductive layer, because the crystals were also analysed with other techniques where a conductive layer would be detrimental for the analysis.

3.2.3 Preparation of *in situ* specimen

The preparation of the Gd₂(MoO₄)₃ lamella for *in situ* biasing experiments were based on the DENS solutions D6+ system, originally developed for heating experiments, with the biasing upgrade called “lightning HB”. The system is easy to use with the “Impulse” software. However, the drawback of this set-up is that it only provides four electrodes, which can either be used for heating or biasing, but not a combination. The procedure described here is thus based on the four-electrode configuration, but it should be fairly straightforward to adapt the process for chips with either six or eight electrodes, where simultaneous heating and biasing is possible.

Recently, FIB has been used to prepare BaTiO₃ for *in situ* biasing and heating experiments, respectively [93, 94]. In the study by Ignatans *et al.* [93], the final polishing steps were performed after the lamella was mounted to the *in situ* chip, while O’Reilly *et al.* [94] used an *ex situ* lift-out procedure to move the lamella after it was thinned to completion in the trench. These studies demonstrate two different approaches to move a lamella from the sample and onto the *in situ* chip. In this work, a procedure was developed which allows for transfer within the FIB, where the aim was to completely finalize the lamella before it was mounted to the biasing chip. By finalizing the lamella first, and mounting it on the chip afterwards, the issue of redeposition from the chip due

to its geometry during the final thinning steps can be minimized, and no other *ex situ* lift out was necessary. Some considerations must be taken into account as presented below.

The developed procedure is illustrated in Figure 3.2.2, and contains the following steps:

- (a) Shows an SEM image of the biasing chip which has four electrodes and two holes where the lamella can be positioned for TEM analysis. There are two different electrode spacings of 5 and 12 μm . Unless it is strictly necessary for the biasing experiment, the largest electrode spacing should be used to make the distance between the electrode weld and the region of interest (ROI) as large as possible to avoid contamination during welding. The specific DENS set-up used here can provide up to 100 V, resulting in maximum fields of 200 and 83 kV/cm for the 5 and 12 μm electrode spacings, respectively.
- (b) The initial part of the procedure was the same as a conventional TEM specimen preparation. Image (b) shows that trenches were made by sputtering away material around the chosen area for the lamella. Blue false coloring is added on the pad of C which was deposited on the surface prior to the milling of the trenches. The lift-out needle, made of pure tungsten with a relatively high electrical conductivity, can be seen to the left in the image. It was placed on the surface of the sample to limit charging effects, due to the low conductance of the oxide material from which the lamella was made.
- (c) Shows the lamella lifted out and mounted as a flag to a Cu grid, where it could easily be thinned down following the conventional procedure. Note that the lamella was fairly “lightly fastened” to the Cu grid with only two small C pads of about $2.5 \mu\text{m} \times 2.5 \mu\text{m}$, the remnants of which can be seen in image (e).
- (d) Shows the finalized lamella. During the thinning of the lamella, it was important to also make sure that its length fit the desired electrode spacing. It is further important that the lamella is as flat as possible on the side facing downwards in the image. It was also easier to mount the lamella to the biasing chip if the side facing upwards is relatively flat too. As seen in the image, the lamella is thicker on either side to maintain some structural stability and avoid severe bending.
- (e) When the lamella was done, the FIB chamber was ventilated and the TEM grid holder was rotated 90° from an orientation where the lamella was standing upright to laying flat. (Image (c) and (e) are both taken at 0° stage tilt, so the 90° rotation of the TEM grid holder is reflected in the images, where the lamella can be seen at different angles). From this point in the sample preparation procedure it was

important to avoid all irradiation of the ROI which can damage the quality of the area. That means no irradiation with the ion beam. Furthermore, just after any weld is made, there will be remnants of the precursor gas for welding in the chamber. Care must therefore also be taken not to irradiate the ROI with the electron beam immediately after any weld is made, since the electron beam may also deposit some contamination from the remnants of the precursor gas on the surface of the ROI. No systematic study of the exact effect of this possible “remnant deposition” was performed, however, paying attention to the chamber pressure just before and after a weld was made can give an indication of the amount of remnant gas in the chamber. The vacuum level is usually recovered after a few minutes. Another important point illustrated in image (e) is the orientation of the lamella and Cu grid. In the FIB used here, the ion beam comes in at an angle of 52° relative to the paper plane from the top of the image, meaning that when the lamella is cut away from the grid, the ion beam is parallel to the long edge of the lamella, causing the least possible amount of redeposition.

- (f) Shows the biasing chip rotated according to the orientation of the lamella, and a sketch indicating how the lamella should be placed. Lowering the lamella down to the biasing chip was a crucial step, since it was easier to see how far the lamella is above the biasing chip by using the ion beam. However, the ROI can not be irradiated by the ion beam, so care must be taken. The red dot in the corner of the sketch of the lamella marks where the first Pt deposition was placed to slightly fasten the lamella to the chip before the lift-out needle was cut away and the lamella was properly welded to the chip.
- (g) Shows an image which was made by using the reduced area scanning (RAS) function when imaging with the ion beam, hence only parts of the areas within the frame was scanned. In the yellow square, a RAS used to find the weld between the lamella and Cu grid can be seen. Thus, after the lift-out needle was fastened to the lamella, the weld could be cut away without illuminating the ROI of the lamella with the ion beam. In the pink square, a RAS used to illuminate only the corner of the lamella together with the lift-out needle can be seen. This view was safe for the lamella.
- (h) Shows the first Pt weld on the lamella with false red color. The field of view was chosen so that the ROI of the lamella was not illuminated.
- (i) Shows the lift-out needle coming in from the left and grounding the electrodes to avoid any charging effects. Also shown is the finalized Pt weld between the lamella

and the right electrode. In order to place the weld on the correct place the RAS function was again used to avoid illuminating the ROI of the lamella with the ion beam. This SEM image is taken after waiting for a while for the remnants of the precursor gas to be pumped away.

- (j) Shows the lamella rotated 180° after the second weld between the electrode and the lamella was made. Since the precursor gas used here comes in from the right (with respect to all these images), the chip was rotated to always make the weld on the right side of the lamella.

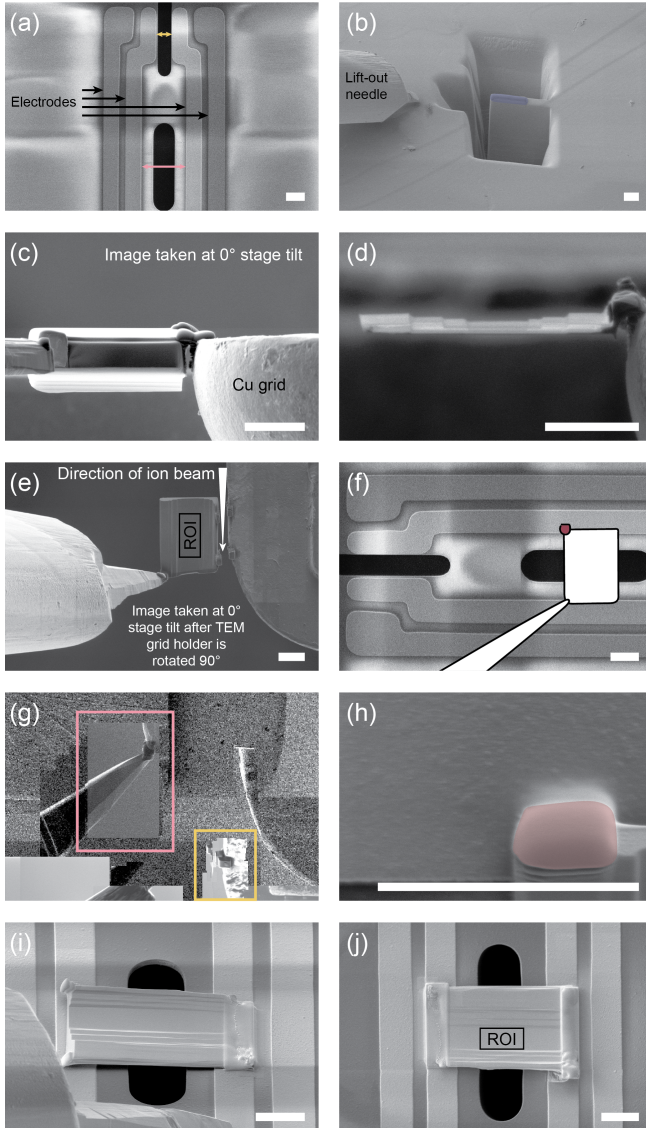


Figure 3.2.2 (a) The biasing chip with the small (yellow arrow) and the large (pink arrow) electrode spacing of 5 and 12 μm , respectively. (b) Following conventional TEM specimen preparation, trenches were milled out around the lamella. Blue false color indicates the C protection layer. (c) The lamella was fastened to a Cu grid for final thinning. (d) Shows the final lamella. (e) The TEM grid holder was rotated 90° by opening the chamber and rotating the holder before closing and evacuating it again. The lift-out needle was fastened to the lamella which was cut away from the Cu grid. (f) The chip, where the sketch indicates the placement of the lamella. (g) Shows how the RAS function was used to avoid illuminating the ROI of the lamella with the ion beam. (h) The lamella was fastened to the chip by a Pt-weld indicated with false red color. (i) and (j) show that the lamella was welded to the electrodes with Pt, first at one side, then the chip was rotated 180° before the other Pt-weld was deposited. All scalebars 5 μm .

3.3 Transmission electron microscopy analysis

Three TEM instruments were used in this work. The majority of the work was performed on the aberration-corrected Jeol JEM ARM200F. The microscope is equipped with a cold FEG which was always operated at 200 kV. The “ARM” is equipped with two CCD cameras, a 2k Orius and a 2k UltraScan XP, and has five different STEM detectors allowing for BF to HAADF-STEM imaging at many different collection angles. It is equipped with a Centurio SDD EDS (nominal solid angle 0.98 sr) for EDS analysis, and a Quantum GIF with DualEELS and 2k CCD for EELS acquisition. The structure determination by CBED was performed on a Jeol JEM 2100F equipped with a Schottky FEG operated at 200 kV. The 2100F has a Gatan 2k UltraScan CCD camera for acquisition of images and diffraction patterns. A Jeol JEM 2100 equipped with a LaB₆ gun was also used for specimen inspection. The “2100” has a Gatan 2k Orius CCD camera.

Gatan Digital Micrograph was used for image acquisition and simple image inspection. In addition, the EELS analysis package in Digital Micrograph was used to calculate relative compositions from EEL spectra. Rigid and non-rigid image registration was done by the SmartAlign plug-in to Digital Micrograph by Jones *et al.* [95]. Any analysis involving finding and fitting a two-dimensional Gaussian to a lattice in a high-resolution STEM image was done using Atomap [96], and HyperSpy [97] was used to analyse the EDS data. The STEM image simulation was performed using MULTEM [98, 99] on the IDUN cluster [100]. Analysis, curve fitting, and plotting of data, was done using the packages NumPy [101], SciPy [102], and Matplotlib [103] in Python.

3.4 X-ray diffraction

Ambient X-ray diffraction (XRD) was performed on a Bruker D8 Focus with a CuK α radiation source. The temperature dependent XRD experiment was done using a Bruker D8 Advanced, also equipped with a CuK α radiation source. An MRI Physikalische Geräte GmbH high temperature controller was used to heat a Pt-strip which was acting as the heat source as well as the sample holder. Both instruments were set up in a Bragg-Brentano geometry. Pawley and Rietveld refinements of the XRD data were done using Topas v5.

Summary of results

4.1 Epitaxial (100), (110), and (111) BaTiO₃ films on SrTiO₃ substrates

BaTiO₃ films deposited on SrTiO₃ substrates, via aqueous CSD, were studied by SAD, TEM and STEM imaging, and EELS for chemical mapping. Ræader *et al.* demonstrated that the films exhibit ferroelectric properties with a remnant polarization between 8.4 and 16.8 $\mu\text{C cm}^{-2}$ depending on the film and electrode orientations. The films had a thickness of about 220-230 nm, and cross sectional TEM specimens were prepared by FIB, as described in Section 3.2.2. Figure 4.1.1 shows three SAD patterns taken from the (100), (110), and (111) oriented films. The selected area aperture used was about 160 nm in diameter and the specimens were positioned such that the substrate-film interfaces bisected the aperture. It is apparent from the diffraction patterns that the films have an epitaxial orientation relation to the substrates, however as shown by the enlarged spots in each pattern, there is a splitting between the spots originating from the SrTiO₃ substrates and the BaTiO₃ films, demonstrating that the films were relaxed. The relaxation was caused by the introduction of misfit dislocations at the substrate-film interfaces.

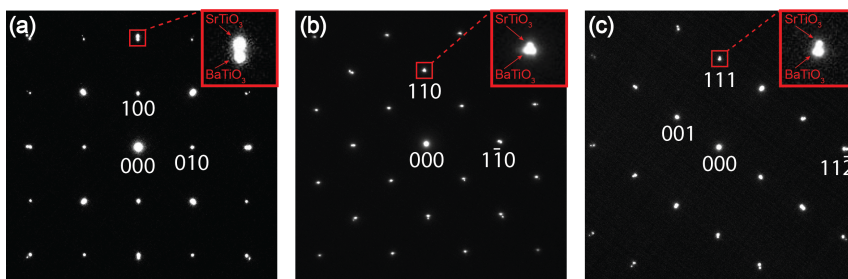


Figure 4.1.1 SAD patterns from the (a) (100), (b) (110), and (c) (111) oriented films. The diffraction patterns were acquired from a volume containing both substrate and film. The patterns are oriented such that “upwards” in the figure is parallel to the substrate normal. Visible in all the patterns is a splitting between the spots originating from the substrate and the film.

A bright-field STEM image of the (100) film is shown in Figure 4.1.2, where strain contrast makes it possible to observe multiple misfit dislocations (highlighted by yellow arrows) and measure the distance between them. Similar STEM images were acquired for the (110) and (111) films, which were imaged from two different directions because of the anisotropy of the higher index substrates. The measured dislocation spacing for the different films are presented in Table 4.1.1. For the (111) film imaged along the $[11\bar{2}]$ zone axis, high-resolution images with two dislocations in the same frame were acquired instead, since the bright-field STEM contrast was weaker in this case, and then the distance between two and two dislocations were measured in multiple images.

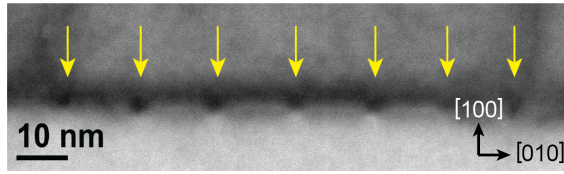


Figure 4.1.2 Bright-field STEM image where misfit dislocations can be observed at the substrate-film interface, due to strain contrast.

The theoretical spacing (S) between edge dislocations in a film on a rigid substrate can be calculated by

$$S = \frac{b}{\delta - \epsilon}, \quad (4.1.1)$$

where b is the in-plane component of Burgers vector perpendicular to the dislocation line direction, $\delta = (a_f - a_d)/a_s$ is the misfit parameter between the film, with lattice parameter a_f , and the substrate, with lattice parameter a_s , and ϵ is the residual in-plane strain in the film. The Burgers vectors and line directions of the misfit dislocations were determined based on the HAADF-STEM images, shown in Figure 4.1.3, where the Burgers closures are indicated by yellow lines. Misfit dislocations in perovskite films usually have Burgers vectors of type $a\langle 100 \rangle$ or $a\langle 110 \rangle$ [104]. Furthermore, a dislocation core will look sharp, if the dislocation is viewed “edge on”, i.e., the line direction is parallel to the beam direction [105]. Based on this, it was determined that the type of Burgers vector for the misfit dislocations in the (100) film is $a\langle 010 \rangle$, and in the (110) film, the dislocations have Burgers vectors $a[1\bar{1}0]$ and $a[001]$ with line directions $[00\bar{1}]$ and $[1\bar{1}0]$, respectively. There are two types of misfit dislocations in the (110) film due to the anisotropy of the substrate. Since the images in Figure 4.1.3 are projections, the indicated Burgers vectors can contain components parallel to the electron beam. Figure 4.1.3(d) and (e) show the projected Burgers vectors observed along two different zone axes in the (111) film. Figure 4.1.3(e) shows a Burgers vector of type $a\langle 110 \rangle$. The projected Burgers vector ($\frac{1}{2}a[11\bar{2}]$) in Figure 4.1.3(d) probably contains a component parallel to the beam direction,

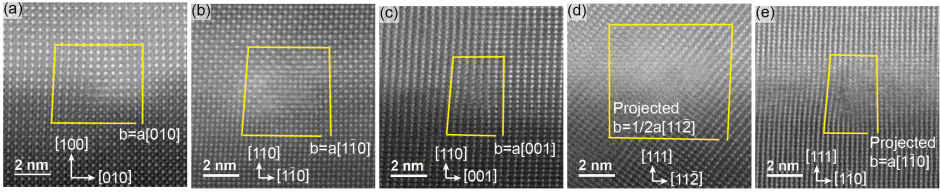


Figure 4.1.3 HAADF-STEM images of the observed misfit dislocations in (a) the (100), (b,c) the (110), and (d,e) the (111) films. The (110) and (111) films were imaged along two different crystallographic orientation, as indicated in the figure.

since it is not a typical Burgers vector in a perovskite based system. Tang *et al.* inferred that misfit dislocations with Burgers vector of type $a\langle 110 \rangle$ in (111) oriented perovskite films have line directions along the $\langle 112 \rangle$ direction [105]. This is also shown here, since the dislocation core looks sharp in Figure 4.1.3(e). According to Xu *et al.*, the Burgers vector $a[0\bar{1}1]$ can be decomposed as [104]

$$a[0\bar{1}1] = \frac{1}{2}a[1\bar{1}0] + \frac{1}{2}a[\bar{1}\bar{1}2]. \quad (4.1.2)$$

The term $\frac{1}{2}a[1\bar{1}0]$ is perpendicular to the direction of the dislocation line and $\frac{1}{2}a[\bar{1}\bar{1}2]$ is parallel to the direction of the dislocation line. The former is a pure edge component that can relax strain along the $(1\bar{1}0)$ planes, while the latter is a pure screw component that can relax shear strains. The findings are summarized in Table 4.1.1 together with the calculated theoretical spacing between the misfit dislocations, based on Equation (4.1.1), assuming that there was no residual strain present in the films.

Table 4.1.1: Measured and theoretical spacing between misfit dislocations in the different films along different directions. Theoretical spacing is provided where the beam direction is parallel to the dislocation line direction. Also presented is the *edge* component of the Burgers vector.

Film	Beam direction	Burgers edge component	S_{Measured} [nm]	S_{Theory} [nm]
(100)	[001]	$a\langle 001 \rangle$	14.5 ± 1.4	15.6
(110)	[00 $\bar{1}$]	$a[1\bar{1}0]$	18.4 ± 2.5	22.0
(110)	[$\bar{1}\bar{1}0$]	$a[001]$	15.2 ± 2.6	15.6
(111)	[$\bar{1}\bar{1}0$]	-	15.7 ± 3.2	-
(111)	[$\bar{1}\bar{1}\bar{2}$]	$\frac{1}{2}a[1\bar{1}0]$	15.3 ± 4.4	11.0

In summary, the (100) film contain only pure edge dislocations, where the Burgers vector is perpendicular to the dislocation line direction. This is also the case for the (110) film, although two types of edge dislocations are found due to the in-plane anisotropy of the substrate. In the (111) film, misfit dislocations containing both an edge component and a screw component were observed.

Figure 4.1.4 shows information obtained about the (100) film by EELS. Similar measurements were also performed for the two other films. Firstly, Figure 4.1.4(a) shows the interdiffusion of Ba and Sr across the substrate-film interface (at 0 nm), where the film and substrate were assumed to be stoichiometric sufficiently far (3-4 nm) from the interface. The stippled lines are fits to the experimental data. The interdiffusion lengths for the different orientations were found to be 3.4, 5.3, and 5.3 nm for the (100), (110), and (111) systems, respectively. Figure 4.1.4(b) shows a HAADF-STEM image where dark stripes are visible between each spin-coated layer. An atomically resolved image of the feature marked in Figure 4.1.4(b) is shown in Figure 4.1.4(c). Since the contrast in HAADF-STEM images scales approximately as Z^2 , the dark feature indicates a lack of a heavy element. This is confirmed by the Ba concentration profile measured by EELS displayed in Figure 4.1.4(d). Similar Ba deficient layers were also observed in the (110) and (111) films, and are proposed to be caused by the volatility of BaO and the high sintering temperature used [106, 107].

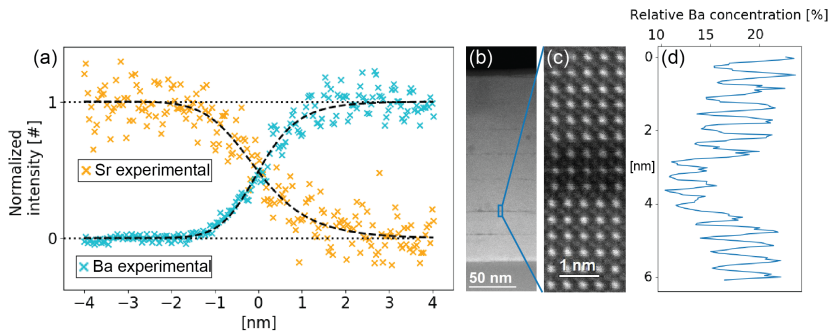


Figure 4.1.4 Properties measured by EELS for the (100) film. (a) The Sr and Ba concentration profile at the substrate film interface, where the intensity was normalized to 1 sufficiently far from the interface. (b) HAADF-STEM images showing thin dark lines between each spin-coated layer, (c) atomically resolved HAADF-STEM image of a dark line, and (d) the Ba concentration profile measured by EELS for the image in (c).

As shown thus far, all the differently oriented films exhibit similar features, like an epitaxial relation to the substrate and strain relaxation due to formation of misfit dislocations at the interface. However, the (111) film displayed a few features that were not observed in the other films, and that was the presence of a thin crystallographic twin layer, an anti-phase boundary, and the growth of a grain with a twin orientation relative to the rest of the film.

4.2 Filled tetragonal tungsten bronzes

Two different compositional series of filled TTBs were studied. The first series was $A_4\text{Bi}_2\text{Nb}_{10}\text{O}_{30}$, $A=\text{Na}$, K , or Rb (ABN), and the second series was $\text{Ba}_4M_2\text{Nb}_{10}\text{O}_{30}$, $M=\text{Na}$, K , or Rb (BMN). As seen by the chemical formulas, substitution of A -site cations were employed in both cases, however, in the case of the Bi-containing TTBs, the substituted alkali metals Na , K , and Rb constituted four out of six A -cations, whereas in the Ba-containing TTBs, the alkali metals constituted only two out of six A -cations. Using the two-step solid state synthesis method ensured that the loss of the volatile Bi and alkali metals were minimized.

In the case of the ABN series, the TEM work was focused on $\text{K}_4\text{Bi}_2\text{Nb}_{10}\text{O}_{30}$ (KBN) and $\text{Rb}_4\text{Bi}_2\text{Nb}_{10}\text{O}_{30}$ (RBN), thus the other compounds are excluded in this summary. Ambient XRD and dielectric spectroscopy up to $700\text{ }^\circ\text{C}$ indicated that a structural change occurred for KBN and RBN in the temperature ranges $340\text{--}420\text{ }^\circ\text{C}$ and $420\text{--}500\text{ }^\circ\text{C}$, respectively, however, at room temperature, some satellite reflections in the XRD patterns could not be accounted for by the most common tetragonal or orthorhombic space groups known for TTBs. CBED was therefore carried out in order to determine the exact symmetry of KBN and RBN.

As described in Section 2.2.5, the space group determination comprises a two-step procedure, first determining the point group, and then the space group. The CBED patterns obtained to establish the point group of KBN and RBN are shown in Figure 4.2.1. The $[001]$ patterns for KBN and RBN displayed in Figure 4.2.1(a) and (b), respectively, demonstrate that $4mm$ symmetry is present in both cases. This limits the possible point groups to $4/mmm$, $\bar{4}2m$, $4mm$, and 422 , since the TTBs must have tetragonal or lower symmetry [69]. The $[110]$ zone axis patterns shown in Figure 4.2.1(c) and (d) for KBN and RBN, exhibit $2mm$ symmetry, which further narrows the possible point groups down to $4/mmm$ and 422 . A zone axis pattern from an $[uov]$ axis can distinguish the remaining point groups, depending on the presence of $2mm$ or only m symmetry. As seen in Figure 4.2.1(e) and (f) for KBN and RBN, respectively, the $[103]$ pattern from KBN, and $[101]$ pattern from RBN both demonstrate $2mm$ symmetry, thus both materials belong to the $4/mmm$ point group [69].

Figure 4.2.2(a) and (b) show $[001]$ SAD patterns, which include both the ZOLZ and the first-order Laue zone (FOLZ), from KBN and RBN, respectively. These can be used to determine the unit cell centring of the space group, due to different extinction rules for differently centred unit cells. When the reflections in the ZOLZ and FOLZ line up in both the a^* - and the b^* -direction, as indicated by the dashed lines, the unit cell has a

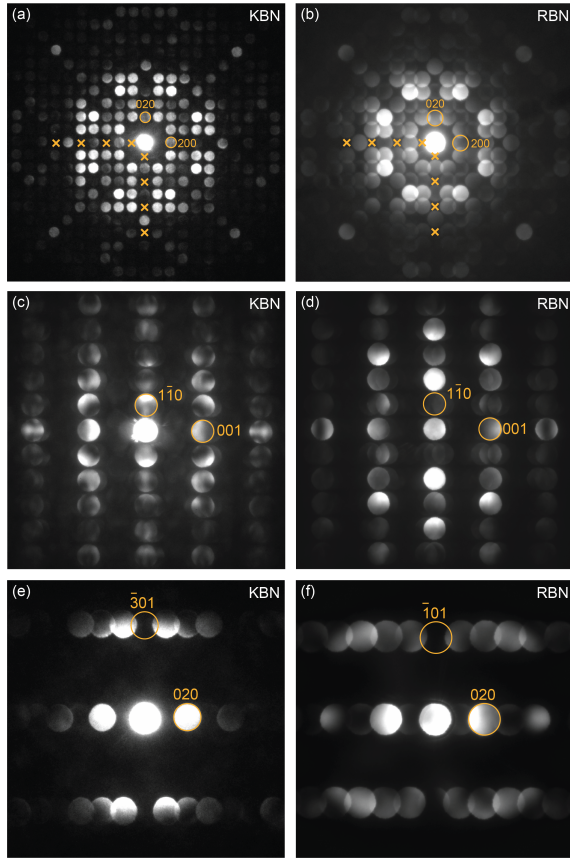


Figure 4.2.1 [001] CBED patterns from (a) KBN and (b) RBN with $4mm$ symmetry present in both cases. Crosses mark kinematically forbidden, but dynamically allowed reflections. [110] CBED patterns from (c) KBN and (d) RBN showing that $2mm$ symmetry is present in both cases. (e) [103] CBED pattern from KBN and (f) [101] CBED pattern from RBN also displaying that $2mm$ symmetry is present in both cases.

primitive centring [1]. There are 16 space groups which possess the $4/mmm$ point group and a primitive unit cell centring, however, information obtained from the [001] zone axis patterns in Figure 4.2.1(a) and (b) narrows it down to only four possible space groups: $P4/mbm$, $P4/mnc$, $P4_2/mbc$, and $P4_2/mnm$. This is due to the presence of GM lines in the kinematically extinct reflections marked by crosses in Figure 4.2.1(a) and (b) [69]. The [103] and [101] CBED patterns in Figure 4.2.1(e) and (f) show kinematic extinct reflections for h_o0l and $0k0$, where h_o indicates that h is odd, thus GM lines must be present in both directions in these patterns. The space groups $P4/mnc$ and $P4_2/mnm$ can be ruled out, since they require GM lines in reflections where $h+l = 2n+1$ (n =integer), however, this never happens in the [103] and [101] CBED patterns in Figure 4.2.1, because the GM

lines always occur where $h + l = 2n$. Lastly, to distinguish between the two remaining space groups, the $[114]$ and $[112]$ CBED patterns shown in Figure 4.2.2(c) and (d) for KBN and RBN, respectively, can be used. $P4_2/mbc$ and $P4/mbm$ differs by having GM lines present in the hhl_o reflections or not, along these projections. There are clearly no GM lines present in the $22\bar{1}$ or $11\bar{1}$ reflections in Figure 4.2.2(c) or (d), respectively. Thus, KBN and RBN must belong to $P4/mbm$, which is centrosymmetric and hence incompatible with ferroelectric properties.

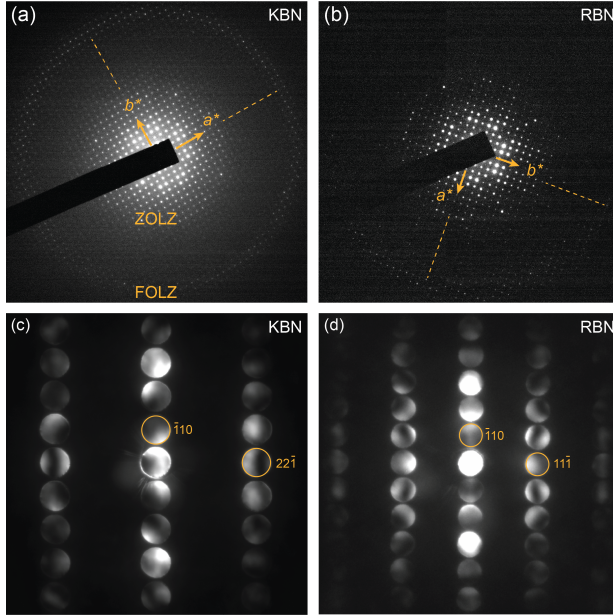


Figure 4.2.2 [001] SAD patterns from (a) KBN and (b) RBN, including ZOLZ and FOLZ reflections. The reflections in the ZOLZ and FOLZ line up for both KBN and RBN, as indicated by the dashed lines. (c) $[114]$ CBED pattern from KBN and (d) $[112]$ CBED pattern from RBN.

The crystal symmetry determined by CBED was supported by P - E loops, which demonstrate a purely dielectric behavior within the measured field strengths for both materials. Furthermore, the lack of an anomaly in the latent heat observed by differential scanning calorimetry (DSC) for both materials demonstrate that a first- or second-order phase transition is likely not present.

It is well known that the Pb^{2+} lone pair causes a large distortion in PbTiO_3 [30], and the same effect is demonstrated, by DFT calculations, to stabilize the high in-plane (within the a - b plane) polarization in the orthorhombic PN [48]. In the first-principles study by Olsen *et al.* [48], it was also proposed that KBN is orthorhombic with an in-plane

polarization due to the presence of the Bi^{3+} lone pair cation. However, the data presented here show that this is not observed experimentally. The anomalies observed in the XRD data and dielectric permittivity are suggested to be connected to the presence of the Bi^{3+} lone pair cations, however, compared to PN, which contain five lone pair cations per unit cell, KBN and RBN only contain two lone pair cations per unit cell. Hence, it is proposed that the concentration of lone pair cations is too low to cause the same distortion in KBN and RBN, as the one observed in PN. Lastly, the Bi^{3+} lone pair is known to be stereochemically weaker than the Pb^{2+} lone pair [108], which may also contribute to the different behavior in KBN and RBN compared to PN.

Figure 4.2.3(a) and (b) display two [110] SAD patterns from KBN and RBN, respectively. Visible in the diffraction patterns are diffraction spots which originate from the primary lattice (indexed spots), in addition to spots originating from incommensurate phases present in the materials. Two types of incommensurate phases are observed in KBN, denoted $\mathbf{q}_1 = 0.14\mathbf{c}^*$ and $\mathbf{q}_2 = 0.32(\mathbf{a}^* + \mathbf{b}^*) + \frac{1}{2}\mathbf{c}^*$, whereas only \mathbf{q}_1 is observed in RBN. TTBs are well known to exhibit incommensurate modulations [51, 52].

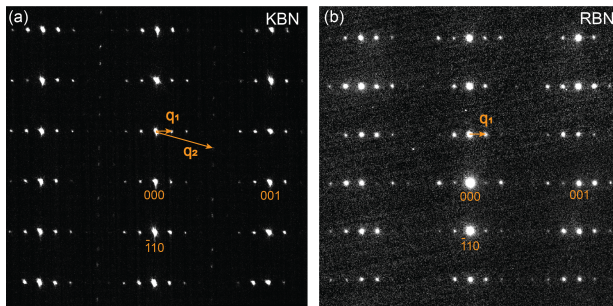


Figure 4.2.3 [110] SAD patterns from (a) KBN and (b) RBN with diffraction spots visible due to incommensurate modulations. KBN (a) exhibits two modulations \mathbf{q}_1 and \mathbf{q}_2 (\mathbf{q}_2 is most clearly visible in the upper left corner), whereas RBN (b) only exhibits the \mathbf{q}_1 modulation.

A systematic study of cation ordering in the TTBs were performed by investigating BMN by XRD and STEM-EDS to establish the degree of intermixing of Ba and $M=\text{Na, K, or Rb}$ on the $A1$ - and $A2$ -site. Quantification of the EDS data was performed by the CL method, both on a pixel-by-pixel basis and on summed spectra from the $A1$ - and $A2$ -site, respectively. HAADF-STEM images and compositional maps of $\text{Ba}_4\text{Na}_2\text{Nb}_{10}\text{O}_{30}$ (BNN), $\text{Ba}_4\text{K}_2\text{Nb}_{10}\text{O}_{30}$ (BKN), and $\text{Ba}_4\text{Rb}_2\text{Nb}_{10}\text{O}_{30}$ (BRN) are shown in Figure 4.2.4. The left column, Figure 4.2.4(a-d), shows results from BNN, the middle column, Figure 4.2.4(e-h), shows results from BKN, and the right column, Figure 4.2.4(i-l), shows results from BRN.

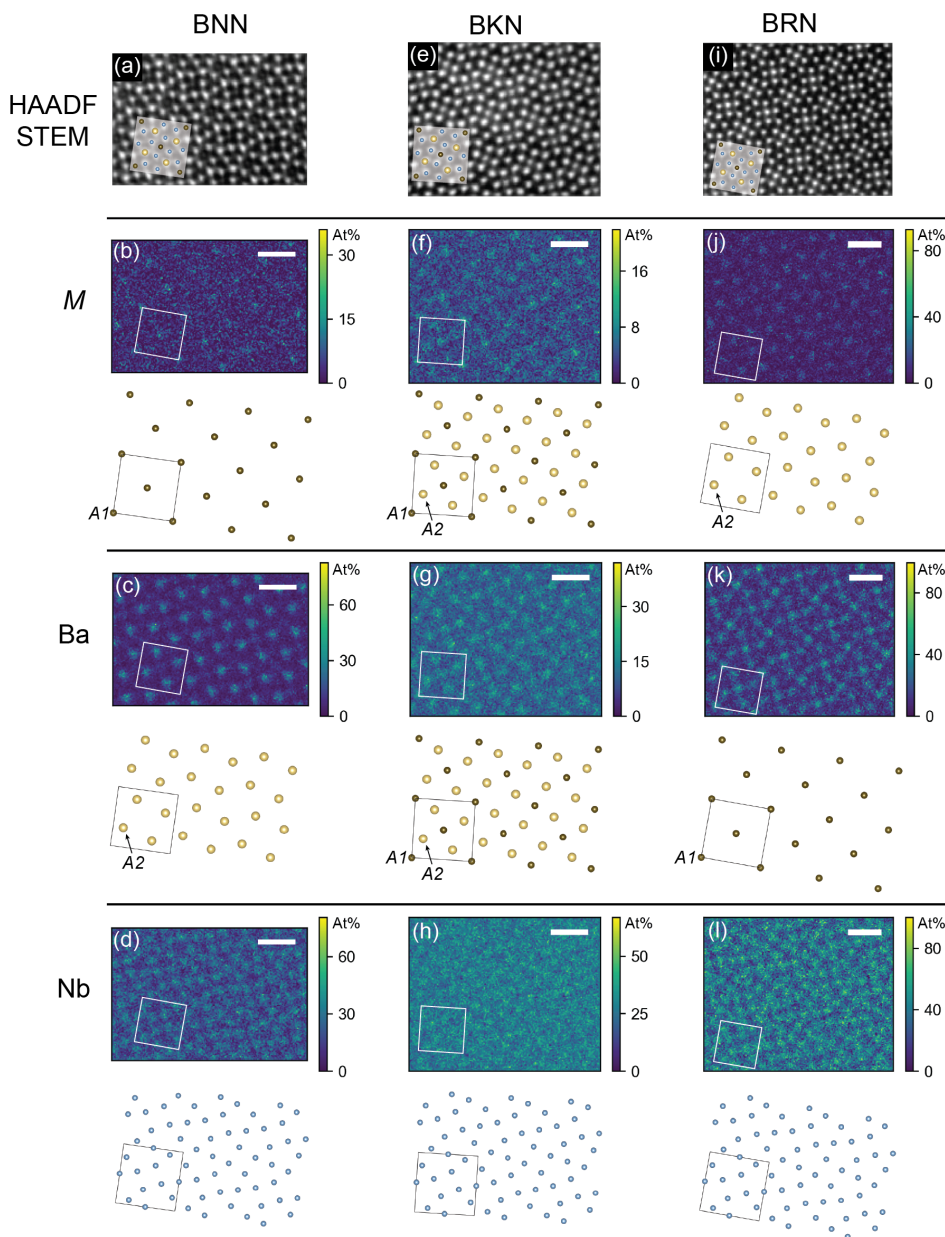


Figure 4.2.4 HAADF-STEM images and compositional maps for (a-d) BNN, (e-h) BKN, and (i-l) BRN, viewed along the c -axis. An atomic sublattice is shown below each map indicating the main site for each element.

Looking first at the Ba concentration in BNN and BRN, it is clear that Ba is mostly situated at the $A2$ -site in BNN, whereas the highest concentration of Ba is found on

the A1-site in BRN. The opposite is the case for the alkali metals in BNN and BRN, where the concentration of Na is highest on the A1-site and Rb is mostly located on the A2-site. BKN demonstrates an intermediate situation to BNN and BRN, where K and Ba are found on both sites. The Nb maps are shown for all the compounds. The Nb atom columns are harder to distinguish since the distance between them are shorter than between the Ba and *M* columns, respectively. The average occupation at each site was calculated from the summed EDS spectra and from Rietveld refinement of the XRD data, and the results are presented in Figure 4.2.5, where the occupation of the alkali metal in the A1-site is plotted against the ionic Shannon radius of the respective alkali metals. The distributions can be explained by the different ionic radii of the constituent A-site cations, where the larger cations have a tendency to occupy the larger A2-site rather than the smaller A1-site. The ionic radii of Na⁺, K⁺, Rb⁺, and Ba²⁺ are 1.39, 1.64, 1.72, and 1.61 Å, respectively [109], meaning that Na⁺ is much smaller, K⁺ is of similar size, and Rb⁺ is larger than Ba²⁺. The overall stoichiometry of the compounds is the reason why the A2-site is occupied approximately 50/50 by Rb and Ba in BRN, whereas mostly only Ba occupies the A2-site in BNN.

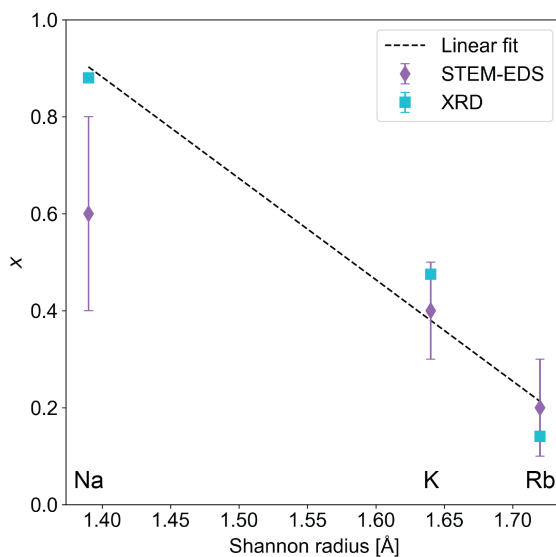


Figure 4.2.5 Occupancy of alkali metal on the A1-site, x , plotted against the Shannon ionic radius of the respective alkali metals. Data from both Rietveld refinement and STEM-EDS are shown, where the error of the XRD data is so small that it is not visible. The stippled line shows a linear fit to the XRD data with $r^2 = 0.95$.

The systematic study on cation distribution in the BMN series demonstrates that it is an important factor to consider for TTBs. The lone pair cation Bi³⁺ has an ionic radius

of 1.36 Å [109], thus the cation distribution in KBN can be expected to be similar to the one in BNN, where 88% of the Na is observed on the *A1*-site. In the first-principles study by Olsen *et al.* [48], the *A1*-site was suggested to be the most ferroelectric active site for the lone pair containing cation. Thus, in addition to containing a low amount of lone pair cations, the fact that possibly less than 100% Bi occupy the *A1*-site in KBN might be disadvantageous for the development of a ferroelectric state at room temperature.

4.3 TEM investigations and phase transition in improper ferroelectric $\text{Gd}_2(\text{MoO}_4)_3$

Conventional and *in situ* biasing TEM specimens of single crystalline $\text{Gd}_2(\text{MoO}_4)_3$ were prepared by FIB. The conventional specimens were investigated by HAADF-STEM imaging to figure out if the polarization direction could be determined from atomically resolved images. The possibility to determine the polarization direction from atomically resolved images would open up for detailed study of the crystal structure at the domain wall as previously demonstrated for e.g. $\text{PbZr}_{0.2}\text{Ti}_{0.8}\text{O}_3$ [73] and hexagonal manganites [14]. Compared to $\text{PbZr}_{0.2}\text{Ti}_{0.8}\text{O}_3$ and hexagonal manganites, the structural difference between two domains in $\text{Gd}_2(\text{MoO}_4)_3$ is small, and the problem is reduced to investigate if it is possible to distinguish how “elliptical” a Mo atom columns is whether it consists of atoms which are positioned 7 or 17 pm apart in projection, as illustrated in Figure 4.3.1. (The atom columns in question are the Mo columns in the upper row in Figure 2.1.12). Or said in other words, can it be determined whether a STEM image is acquired along the *a*- or *b*-axis of the orthorhombic structure, even though they look very similar in projection. High-quality atomically resolved images were obtained from the beam sensitive specimen by acquiring multiple images using a low beam current, which were subsequently stacked after performing image alignment and scan-distortion compensation by SmartAlign as described in [95]. One of the resulting images is shown in Figure 4.3.1(b), where the atom columns which should differ the most between different domains/orientations are marked by pink arrows. Also shown in Figure 4.3.1(c) and (d) are multislice image simulations along two different zone axes of $\text{Gd}_2(\text{MoO}_4)_3$, corresponding to the two different domains. The Python package Atomap [96] was used to fit the atom columns marked with pink arrows to two-dimensional Gaussians, and the ellipticity ϵ of each atom column was then defined as:

$$\epsilon = \begin{cases} \frac{\sigma_x}{\sigma_y}, & \text{if } \sigma_x > \sigma_y \\ \frac{\sigma_y}{\sigma_x}, & \text{if } \sigma_y > \sigma_x, \end{cases} \quad (4.3.1)$$

where σ_x and σ_y are the standard deviations, in the x - and y -direction, of the two-dimensional Gaussian. The rotation of the ellipse is defined such that it is the angle between the positive x -axis and the longest σ . This will always be a value between 0 and $\pi \sim 3.14$ rad, due to the symmetry of a two-dimensional Gaussian. Figure 4.3.1(e) and (g) present the ellipticity and rotation values obtained from the simulated image along the a -axis in Figure 4.3.1(d), and the results from the analysis of the image simulated along the b -axis (Figure 4.3.1(d)) are shown in Figure 4.3.1(f) and (h). Visible in Figure 4.3.1(e-h) is that the distribution of ellipticity values is very similar for both cases, in addition, the rotation appears to have an even spread between 0 and 3.14 rad, meaning that no clear trend towards the ellipses being oriented along the horizontal is observed. This indicates that columns of atoms which are displaced 7 or 17 pm apart along the x -axis does not cause the ellipticity of the atom column to be large enough to be observed by HAADF-STEM imaging and subsequent image analysis.

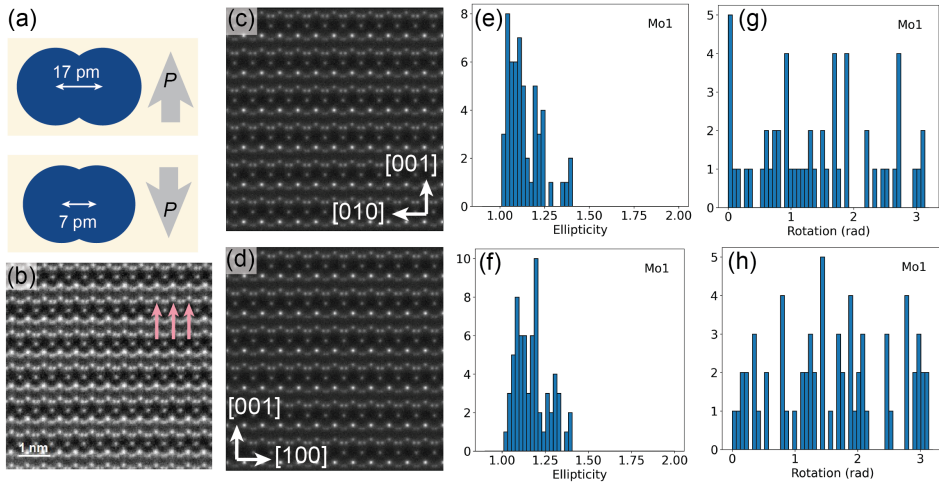


Figure 4.3.1 (a) Illustration of how the two atom columns which shift the most between polarization orientations are displaced for “polarization up” and “polarization down”. Note that the polar axis is along the direction of the arrows, whereas the displacement is along the horizontal, as indicated. (b) HAADF-STEM image of $\text{Gd}_2(\text{MoO}_4)_3$ where the arrows indicate the atom column where the atoms which shift the most upon polarization reversal sits. (c) and (d) are HAADF-STEM image simulations along the a - and b -axes, respectively. (e-h) are results from the analysis of the ellipticity of the atom columns. (e) and (f) show the occurrences of ellipticity values measured in (c) and (d), respectively, and (g) and (h) show the “rotation” of the ellipticity compared to the horizontal measured in (c) and (d), respectively. Rotation values of 0 and 3.14 rad means that the ellipse is parallel to the horizontal.

A successful FIB preparation procedure was developed for *in situ* biasing in the TEM. The quality of the specimen was confirmed by an initial resistivity in the $\text{M}\Omega$ range

and no sign of amorphous layers from SAD. However, challenges were encountered during the biasing experiment due to remnant strain present in the lamella from the preparation procedure. In addition, increasing conductivity during the experiment, and strain contrast, likely caused by the ferroelastic properties of $\text{Gd}_2(\text{MoO}_4)_3$, possibly overshadowing other features developing during biasing, caused difficulties. The structural complexity combined with the minor distortions between different polarization states encountered in $\text{Gd}_2(\text{MoO}_4)_3$ motivated a thorough XRD study combined with Rietveld refinement to study the structure in detail, and in particular investigate the phase transition in the improper ferroelectric.

The XRD study of $\text{Gd}_2(\text{MoO}_4)_3$ was performed using powder synthesized via a solid state method, and temperatures ranging from ambient up to 275 °C. Rietveld refinement of the diffraction patterns were performed by a fit to the space group $Pba2$ below 159 °C, and from 159 °C and above they were fitted to $P\bar{4}2_1m$. Because of the unit cell doubling at the phase transition, the lattice parameters of the paraelectric phase were converted to the non-standard setting $C\bar{4}2_1$, where $a_{C\bar{4}2_1} = \sqrt{2}a_{P\bar{4}2_1m}$, such that the ferroelectric and paraelectric phases could be compared directly, as introduced by Jeitschko [54]. The thermal evolution of the lattice parameters and the volume evolution are shown in Figure 4.3.2. The stippled lines display the extrapolated a and c parameters of the $C\bar{4}2_1$ phase in Figure 4.3.2(a), in addition to the extrapolated volume in Figure 4.3.2(b). Visible at the paraelectric-to-ferroelectric transition point at 159 °C, is the expansion of the c -axis and the splitting and contraction of the tetragonal a -axis into the orthorhombic a - and b -axes. A discontinuous volume change is also evident at the transition point, which reflects the first order nature of the phase transition. The lattice parameter evolution is in excellent agreement with literature, and demonstrates that the synthesized powder is of high quality, as it reproduces results previously reported for single crystals [110]. Since the lattice parameter evolution was obtained for multiple temperatures above the phase transition, the strain of the ferroic phase could be calculated, demonstrating negative values for the a - and the b -axis, since they are compressed in the ferroic state, while the strain was positive for the c -axis.

Rietveld refinement was employed to study the displacement of cations during the development of the ferroic phase. The oxygen positions were not refined, since it required the addition of 36 free parameters without significantly improving the fit. Figure 4.3.3(a) and (b) shows the result for the cations which displaced the most from their position in the paraelectric state. The crystal structure of $\text{Gd}_2(\text{MoO}_4)_3$ is shown along the a -axis in Figure 4.3.3(c), where it can be seen that the structure can be viewed as a layered structure with three layers. The cations which displace the most from the paraelectric phase are

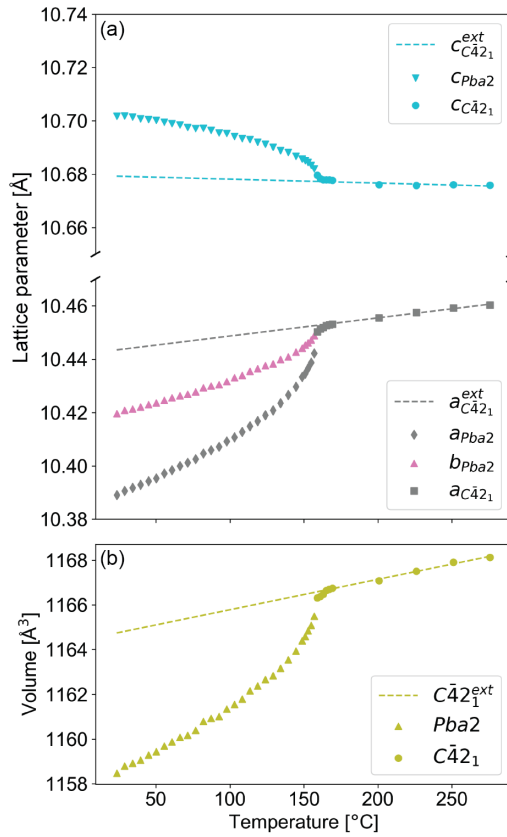


Figure 4.3.2 (a) Thermal evolution of the lattice parameters of Gd₂(MoO₄)₃. (b) Thermal evolution of the volume below and above $T_C=159$ °C. A discontinuity in the volume change is visible at the transition temperature.

positioned in layer 1 and layer 2, which are shown along the c -axis in Figure 4.3.3(d) and (e), respectively. Two different types of critical behavior were observed, either a linear displacement away from the position in the paraelectric phase or a discontinuous behaviour at T_C , followed by a behavior which was better described by an empirical formula based on second order Landau theory, than a linear fit, as demonstrated by a better goodness-of-fit value for the empirical Landau fit.

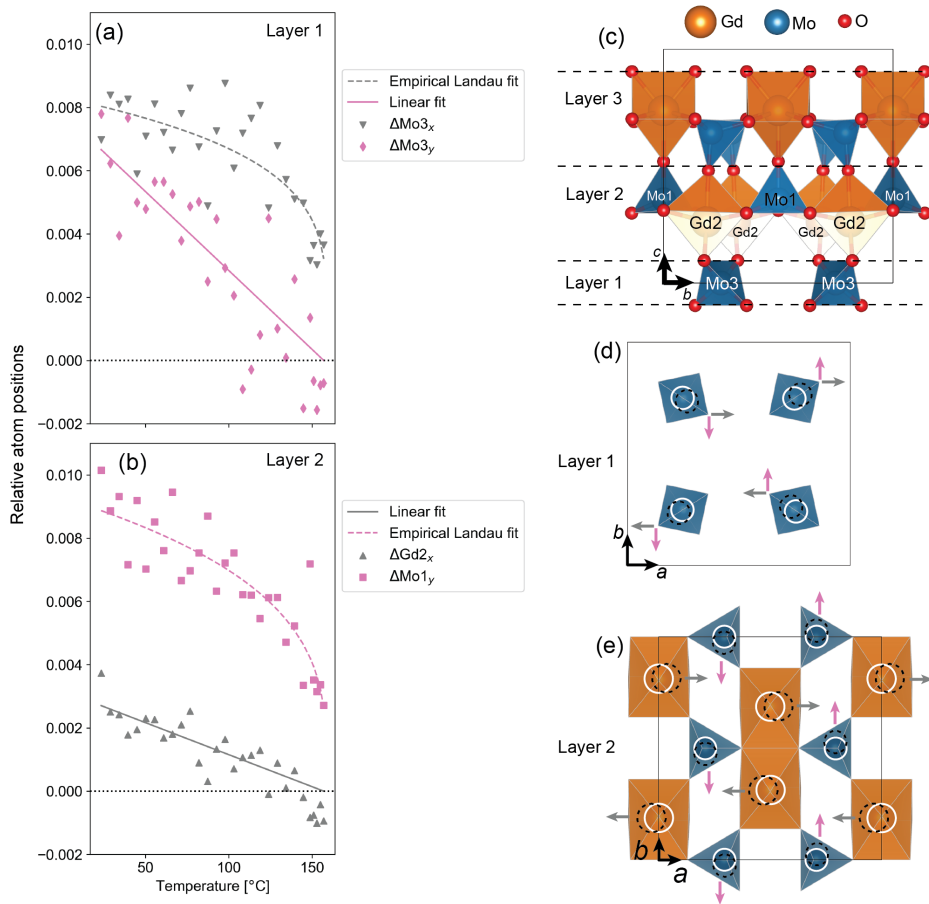


Figure 4.3.3 The temperature evolution of the relative displacement of (a) Mo3, and (b) Mo1 and Gd2 in the $Pba2$ phase. (c), (d), and (e) show the $C\bar{4}2_1$ phase of $Gd_2(MoO_4)_3$ (with atom designation referring to the $Pba2$ phase). (c) $Gd_2(MoO_4)_3$ viewed as a three-layered structure when projected along the a -axis, and (d) layer 1 and (e) layer 2 viewed along the c -axis. The direction of the cation movement from the $C\bar{4}2_1$ phase to the $Pba2$ is indicated with white rings as the starting positions, and black dashed rings and arrows indicate the direction of the cation displacement. (The relative movement is exaggerated in the illustration).

Conclusion

The work presented in this thesis has demonstrated that TEM is a very useful tool in the study of ferroic materials. Local variation in the structure and chemistry at an atomic scale were investigated in oxide films as well as bulk materials, through techniques such as high-resolution HAADF-STEM and atomically resolved EELS and EDS. These techniques provide information which is difficult to obtain through other experimental methods. The crystal symmetry of KBN and RBN, which was previously not known, was established to be centrosymmetric through investigations by CBED. On the other hand, when the structural variations between two domains became miniature, on the order of picometers, or when specimen damage occurred by the incident high-energy electron beam, it was useful to combine TEM with alternative characterization techniques, such as XRD. Temperature dependent experiments are also more routinely performed with XRD than in the TEM. Thus, structural information across the phase transition in $\text{Gd}_2(\text{MoO}_4)_3$ was obtained by XRD, providing new insight into the improper ferroelectric transition. The high vacuum environment within the TEM may also cause unwanted effects, as demonstrated by the observed increased conductivity during the *in situ* biasing experiment. Furthermore, the combination of multiple nanoscopic and macroscopic characterization techniques proved to be useful to fully investigate different properties of the tetragonal tungsten bronzes, demonstrating an important feature of modern materials science, that a combination of multiple experimental techniques is essential in order to advance the field.

Bibliography

- [1] D. B. Williams and C. B. Carter. *Transmission Electron Microscopy*. Springer US, 2009.
- [2] S. Pennycook et al. “Materials Advances through Aberration-Corrected Electron Microscopy.” *MRS Bulletin* 31 (2006), 36.
- [3] D. J. Smith. “Ultimate resolution in the electron microscope?” *Materials Today* 11 (2008), 30.
- [4] J. Valasek. “Piezo-Electric and Allied Phenomena in Rochelle Salt.” *Physical Review* 17 (1921), 475.
- [5] J. F. Scott. “Applications of Modern Ferroelectrics.” *Science* 315 (2007), 954.
- [6] K. Aizu. “Possible Species of “Ferroelastic” Crystals and of Simultaneously Ferroelectric and Ferroelastic Crystals.” *Journal of the Physical Society of Japan* 27 (1969), 387.
- [7] M. Fiebig et al. “The evolution of multiferroics.” *Nature Reviews Materials* 1 (2016), 16046.
- [8] N. A. Spaldin. “Multiferroics: Past, present, and future.” *MRS Bulletin* 42 (2017), 385.
- [9] N. A. Spaldin and R. Ramesh. “Advances in magnetoelectric multiferroics.” *Nature Materials* 18 (2019), 203–212.
- [10] J. M. Zuo and J. C. Spence. *Advanced Transmission Electron Microscopy*. Springer, 2017.
- [11] S. Kobayashi et al. “Multiphase nanodomains in a strained BaTiO₃ film on a GdScO₃ substrate.” *Journal of Applied Physics* 123 (2018), 064102.
- [12] A. K. Yadav et al. “Observation of polar vortices in oxide superlattices.” *Nature* 530 (2016), 198.
- [13] F. Li et al. “Giant piezoelectricity of Sm-doped Pb(Mg_{1/3}Nb_{2/3})O₃-PbTiO₃ single crystals.” *Science* 364 (2019), 264.

- [14] M. E. Holtz et al. "Topological Defects in Hexagonal Manganites: Inner Structure and Emergent Electrostatics." *Nano Letters* 17 (2017), 5883.
- [15] Y.-T. Shao and J.-M. Zuo. "Nanoscale symmetry fluctuations in ferroelectric barium titanate, BaTiO₃." *Acta Crystallographica Section B* 73 (2017), 708.
- [16] C. Kittel. *Introductio to Solid State Physics*. John Wiley & Sons, Inc, 2005.
- [17] M. E. Lines and A. M. Glass. *Principles and Applications of Ferroelectrics and Related Materials*. Oxford University Press, 1977.
- [18] D. Damjanovic. "Ferroelectric, dielectric and piezoelectric properties of ferroelectric thin films and ceramics." *Reports on Progress in Physics* 61 (1998), 1267.
- [19] J. Nye. *Physical properties of crystals: Their representation by tensors and matrices*. Oxford: Clarendon Press, 1985.
- [20] B. M. Wul and I. M. Goldman. *Dokl. Akad. Nauk SSSR* 51 (1946), 21.
- [21] H. D. Megaw. "Crystal structure of double oxides of the perovskite type." *Proceedings of the Physical Society* 58 (1946), 133.
- [22] H. D. Megaw. "Origin of ferroelectricity in barium titanate and other perovskite-type crystals." *Acta Crystallographica* 5 (1952), 739.
- [23] K. Momma and F. Izumi. "VESTA 3 for three-dimensional visualization of crystal, volumetric and morphology data." *Journal of Applied Crystallography* 44 (2011), 1272.
- [24] A. Tagantsev, L. E. Cross, and J. Fousek. *Domains in Ferroic Crystals and Thin Films*. Springer-Verlag New York, 2010.
- [25] P. W. Anderson. In: *Fizika Dielektrikov*. Ed. by G. I. Skanavi. Akad. Nauk. SSSR, 1960.
- [26] W. Cochran. "Crystal stability and the theory of ferroelectricity." *Advances in Physics* 9 (1960), 387.
- [27] C. N. R. Rao and J. Gopalakrishnan. *New Directions in Solid State Chemistry*. Cambridge University Press, Feb. 1997.
- [28] S. M. Selbach. *Lecture notes on soft modes*. 2019.
- [29] E. A. Stern. "Character of Order-Disorder and Displacive Components in Barium Titanate." *Physical Review Letters* 93 (2004), 037601.
- [30] R. E. Cohen. "Origin of ferroelectricity in perovskite oxides." *Nature* 358 (1992), 136.

- [31] L. Landau. "On The Theory of Phase Transitions." *Zh. Eksp. Teor. Fiz.* 7 (1937), 19.
- [32] V. L. Ginzburg. "Phase transitions in ferroelectrics: some historical remarks." *Physics-Uspekhi* 44 (2001), 1037.
- [33] A. Devonshire. "XCVI. Theory of barium titanate." *The London, Edinburgh, and Dublin Philosophical Magazine and Journal of Science* 40 (1949), 1040.
- [34] N. A. Hill. "Why Are There so Few Magnetic Ferroelectrics?" *The Journal of Physical Chemistry B* 104 (2000), 6694.
- [35] H. Kay and P. Vousden. "XCV. Symmetry changes in barium titanate at low temperatures and their relation to its ferroelectric properties." *The London, Edinburgh, and Dublin Philosophical Magazine and Journal of Science* 40 (1949), 1019.
- [36] A. Safari and E. K. Akdoğan, eds. *Piezoelectric and Acoustic Materials for Transducer Applications*. Springer US, 2008.
- [37] W. J. Merz. "The Dielectric Behavior of BaTiO₃ Single-Domain Crystals." *Physical Review* 75 (1949), 687.
- [38] K. J. Choi et al. "Enhancement of Ferroelectricity in Strained BaTiO₃ Thin Films." *Science* 306 (2004), 1005.
- [39] R. People and J. C. Bean. "Calculation of critical layer thickness versus lattice mismatch for Ge_xSi_{1-x}/Si strained-layer heterostructures." *Applied Physics Letters* 47 (1985), 322.
- [40] T. Suzuki, Y. Nishi, and M. Fujimoto. "Analysis of misfit relaxation in heteroepitaxial BaTiO₃ thin films." *Philosophical Magazine A* 79 (1999), 2461.
- [41] T. M. Raeder et al. "Enhanced in-plane ferroelectricity in BaTiO₃ thin films fabricated by aqueous chemical solution deposition." *AIP Advances* 8 (2018), 105228.
- [42] K. L. Ngai and T. L. Reinecke. "Model of the Ferroelectric Phase Transition in the Tetragonal Tungsten-Bronze-Structure Ferroelectrics." *Physical Review Letters* 38 (1977), 74.
- [43] T. A. Whittle, C. J. Howard, and S. Schmid. "Structures and phase transitions in barium sodium niobate tungsten bronze (BNN)." *Acta Crystallographica Section B* 77 (2021).

- [44] R. R. Neurgaonkar et al. "Growth and optical properties of ferroelectric tungsten bronze crystals." *Ferroelectrics* 142 (1993), 167.
- [45] Z. J. Yang et al. " $\text{Ba}_4\text{R}_2\text{Sn}_4\text{Nb}_6\text{O}_{30}$ (R = La, Nd, Sm) lead-free relaxors with filled tungsten bronze structure." *Journal of the American Ceramic Society* 102 (2019), 4721.
- [46] X. Zhu et al. "A Crystal-Chemical Framework for Relaxor versus Normal Ferroelectric Behavior in Tetragonal Tungsten Bronzes." *Chemistry of Materials* 27 (2015), 3250.
- [47] G. H. Olsen et al. "Origin of ferroelectric polarization in tetragonal tungsten-bronze-type oxides." *Physical Review B* 93 (2016), 180101.
- [48] G. H. Olsen et al. "Role of Lone Pair Cations in Ferroelectric Tungsten Bronzes." *Chemistry of Materials* 29 (2017), 6414.
- [49] S. S. Aamlid, S. M. Selbach, and T. Grande. "Structural Evolution of Ferroelectric and Ferroelastic Barium Sodium Niobate Tungsten Bronze." *Inorganic Chemistry* 59 (2020), 8514.
- [50] A. A. Bokov and Z.-G. Ye. "Recent progress in relaxor ferroelectrics with perovskite structure." *Journal of Materials Science* 41 (2006), 31.
- [51] M. Paściak et al. "Local structure of relaxor ferroelectric $\text{Sr}_x\text{Ba}_{1-x}\text{Nb}_2\text{O}_6$ from a pair distribution function analysis." *Physical Review B* 99 (2019), 104102.
- [52] K. Lin et al. "Unusual Strong Incommensurate Modulation in a Tungsten-Bronze-Type Relaxor $\text{PbBiNb}_5\text{O}_{15}$." *Journal of the American Chemical Society* 137 (2015), 13468.
- [53] E. T. Keve, S. C. Abrahams, and J. L. Bernstein. "Ferroelectric Ferroelastic Paramagnetic Beta- $\text{Gd}_2(\text{MoO}_4)_3$ Crystal Structure of the Transition-Metal Molybdates and Tungstates. VI." *The Journal of Chemical Physics* 54 (1971), 3185.
- [54] W. Jeitschko. "A Comprehensive X-ray Study of the Ferroelectric-Ferroelastic and Paraelectric-Paraelastic Phases of $\text{Gd}_2(\text{MoO}_4)_3$." *Acta Crystallographica Section B* 28 (1972), 60.
- [55] L. Brixner et al. "Precision parameters of some $\text{Ln}_2(\text{MoO}_4)_3$ -type rare earth molybdates." *Materials Research Bulletin* 6 (1971), 545.

- [56] I.-E. Nylund et al. “Observation of cation-specific critical behavior at the improper ferroelectric phase transition in $\text{Gd}_2(\text{MoO}_4)_3$.” *Physical Review Materials* 6 (3 2022), 034402.
- [57] J. R. Barkley and W. Jeitschko. “Antiphase boundaries and their interactions with domain walls in ferroelastic-ferroelectric $\text{Gd}_2(\text{MoO}_4)_3$.” *Journal of Applied Physics* 44 (1973), 938.
- [58] N. Yamamoto, K. Yagi, and G. Honjo. “Electron microscopic studies of ferroelectric and ferroelastic $\text{Gd}_2(\text{MoO}_4)_3$. I. General features of ferroelectric domain wall, antiphase boundary, and crystal defects.” *Physica Status Solidi (a)* 41 (1977), 523.
- [59] M. Nord et al. “Fast Pixelated Detectors in Scanning Transmission Electron Microscopy. Part I: Data Acquisition, Live Processing, and Storage.” *Microscopy and Microanalysis* 26 (2020), 653.
- [60] G. W. Paterson et al. “Fast Pixelated Detectors in Scanning Transmission Electron Microscopy. Part II: Post-Acquisition Data Processing, Visualization, and Structural Characterization.” *Microscopy and Microanalysis* 26 (2020), 944.
- [61] D. Peng. *Categorization inspired by a lecture given at NTNU*. 2021.
- [62] C. J. Humphreys. “The scattering of fast electrons by crystals.” *Reports on Progress in Physics* 42 (1979), 1825.
- [63] R. Erni. *Aberration-Corrected Imaging in Transmission Electron Microscopy*. Imperial College Press, 2010.
- [64] P. E. Batson, N. Dellby, and O. L. Krivanek. “Sub-ångstrom resolution using aberration corrected electron optics.” *Nature* 418 (2002), 617.
- [65] M. Haider et al. “Electron microscopy image enhanced.” *Nature* 392 (1998), 768.
- [66] A. S. Everhardt et al. “Temperature-independent giant dielectric response in transitional BaTiO_3 thin films.” *Applied Physics Reviews* 7 (2020), 011402.
- [67] C. B. Carter and D. B. Williams, eds. *Transmission Electron Microscopy*. Springer International Publishing, 2016.
- [68] B. F. Buxton et al. “The symmetry of electron diffraction zone axis patterns.” *Philosophical Transactions of the Royal Society of London. Series A, Mathematical and Physical Sciences* 281 (1976), 171.

- [69] M. Tanaka and M. Terauchi. *Convergent-Beam Electron Diffraction Vol. I*. JEOL Ltd., 1985.
- [70] J. Gjønnes and A. F. Moodie. “Extinction conditions in the dynamic theory of electron diffraction.” *Acta Crystallographica* 19 (1965), 65.
- [71] P. Nellist and S. Pennycook. *The principles and interpretation of annular dark-field Z-contrast imaging*. Vol. 113. Advances in Imaging and Electron Physics. Academic Press, 2000, 147.
- [72] A. B. Yankovich et al. “Picometre-precision analysis of scanning transmission electron microscopy images of platinum nanocatalysts.” *Nature Communications* 5 (2014), 4155.
- [73] C.-L. Jia et al. “Direct Observation of Continuous Electric Dipole Rotation in Flux-Closure Domains in Ferroelectric Pb(Zr,Ti)O₃.” *Science* 331 (2011), 1420.
- [74] D. Rusu et al. “Ferroelectric incommensurate spin crystals.” *Nature* 602 (2022), 240.
- [75] P. Gao et al. “Picometer-scale atom position analysis in annular bright-field STEM imaging.” *Ultramicroscopy* 184 (2018), 177.
- [76] S. de Graaf et al. “Resolving hydrogen atoms at metal-metal hydride interfaces.” *Science Advances* 6 (2020).
- [77] P. Nukala et al. “Reversible oxygen migration and phase transitions in hafnia-based ferroelectric devices.” *Science* 372 (2021), 630.
- [78] W. Gao et al. “Real-space charge-density imaging with sub-ångström resolution by four-dimensional electron microscopy.” *Nature* 575 (2019), 480.
- [79] E. J. Kirkland. *Advanced Computing in Electron Microscopy*. Springer US, 2010.
- [80] H. Winick. *X-ray data booklet*. 2009.
- [81] E. P. Bertin. *Principles and Practice of X-Ray Spectrometric Analysis*. Plenum Press, 1975.
- [82] G. Cliff and G. W. Lorimer. “The quantitative analysis of thin specimens.” *Journal of Microscopy* 103 (1975), 203.
- [83] P. Lu et al. “Chemical Quantification of Atomic-Scale EDS Maps under Thin Specimen Conditions.” *Microscopy and Microanalysis* 20 (2014), 1782.

- [84] S. Wenner et al. "Atomic-resolution chemical mapping of ordered precipitates in Al alloys using energy-dispersive X-ray spectroscopy." *Micron* 96 (2017), 103.
- [85] S. Iijima, I. Ohnishi, and Z. Liu. "Atomic-resolution STEM-EDS studies of cation ordering in Ti-Nb oxide crystals." *Scientific Reports* 11 (2021), 18022.
- [86] R. F. Egerton. *Electron Energy-Loss Spectroscopy in the Electron Microscope*. Springer-Verlag GmbH, 2011.
- [87] R. F. Egerton. "Electron energy-loss spectroscopy in the TEM." *Reports on Progress in Physics* 72 (2008), 016502.
- [88] I. MacLaren et al. "EELS at very high energy losses." *Microscopy* 67 (2017), i78.
- [89] N. Yao, ed. *Focused Ion Beam Systems*. Cambridge University Press, 2007.
- [90] T. M. Raeder et al. "Anisotropic in-plane dielectric and ferroelectric properties of tensile-strained BaTiO₃ films with three different crystallographic orientations." *AIP Advances* 11 (2021), 025016.
- [91] M. C. G. Afonso. "Preparation and characterization of rare earth molybdates: structure-property relation." PhD thesis. Universidad de La Laguna, 2015.
- [92] M. Schaffer, B. Schaffer, and Q. Ramasse. "Sample preparation for atomic-resolution STEM at low voltages by FIB." *Ultramicroscopy* 114 (2012), 62.
- [93] R. Ignatans, D. Damjanovic, and V. Tileli. "Local hard and soft pinning of 180° domain walls in BaTiO₃ probed by in situ transmission electron microscopy." *Physical Review Materials* 4 (2020), 104403.
- [94] T. O'Reilly, K. Holsgrove, and M. Arredondo. "Investigating BaTiO₃ via in situ heating TEM. The effect of annealing on thermally driven behavior." *Wiley Analytical Science: Electron and Ion Microscopy Articles* (2021).
- [95] L. Jones et al. "Smart Align - a new tool for robust non-rigid registration of scanning microscope data." *Advanced Structural and Chemical Imaging* 1 (2015).
- [96] M. Nord et al. "Atomap: a new software tool for the automated analysis of atomic resolution images using two-dimensional Gaussian fitting." *Advanced Structural and Chemical Imaging* 3 (2017).
- [97] F. D. L. Peña et al. *HyperSpy v1.5.2*. 2019.

- [98] I. Lobato and D. V. Dyck. “MULTEM: A new multislice program to perform accurate and fast electron diffraction and imaging simulations using Graphics Processing Units with CUDA.” 156 (2015), 9.
- [99] I. Lobato, S. V. Aert, and J. Verbeeck. “Progress and new advances in simulating electron microscopy datasets using MULTEM.” 168 (2016), 17.
- [100] M. Sjölander et al. *EPIC: An Energy-Efficient, High-Performance GPGPU Computing Research Infrastructure*. 2019.
- [101] C. R. Harris et al. “Array programming with NumPy.” *Nature* 585 (2020), 357.
- [102] P. Virtanen et al. “SciPy 1.0: fundamental algorithms for scientific computing in Python.” *Nature Methods* 17 (2020), 261.
- [103] J. D. Hunter. “Matplotlib: A 2D Graphics Environment.” *Computing in Science & Engineering* 9 (2007), 90.
- [104] Y. B. Xu et al. “Misfit Strain Relaxation of Ferroelectric PbTiO₃/LaAlO₃ (111) Thin Film System.” *Scientific Reports* 6 (2016), 35172.
- [105] Y. Tang et al. “Misfit dislocations of anisotropic magnetoresistant Nd_{0.45}Sr_{0.55}MnO₃ thin films grown on SrTiO₃ (110) substrates.” *Acta Materialia* 60 (2012), 5975.
- [106] R. Sažinas et al. “Effect of CO₂ Exposure on the Chemical Stability and Mechanical Properties of BaZrO₃-Ceramics.” *Journal of the American Ceramic Society* 99 (2016), 3685.
- [107] R. Sažinas, M.-A. Einarsrud, and T. Grande. “Toughening of Y-doped BaZrO₃ proton conducting electrolytes by hydration.” *Journal of Materials Chemistry A* 5 (2017), 5846.
- [108] A. Walsh et al. “Stereochemistry of post-transition metal oxides: revision of the classical lone pair model.” *Chemical Society Reviews* 40 (2011), 4455.
- [109] R. D. Shannon. “Revised effective ionic radii and systematic studies of interatomic distances in halides and chalcogenides.” *Acta Crystallographica Section A* 32 (1976), 751.
- [110] J. Kobayashi, Y. Sato, and T. Nakamura. “X-ray study on thermal expansion of ferroelectric Gd₂(MoO₄)₃.” *Physica Status Solidi (a)* 14 (1972), 259.

Appendices

Paper 1

**Epitaxial (100), (110), and (111) BaTiO₃ films on SrTiO₃ substrates
- A transmission electron microscopy study**

Nylund, I.-E., Raeder, T. M., Vullum, P. E., and Grande, T.

Journal of Applied Physics **129**, 095304 (2021)

Epitaxial (100), (110), and (111) BaTiO₃ films on SrTiO₃ substrates—A transmission electron microscopy study

Cite as: J. Appl. Phys. 129, 095304 (2021); doi: 10.1063/5.0045011
Submitted: 21 January 2021 · Accepted: 14 February 2021 ·
Published Online: 4 March 2021



I.-E. Nylund,¹ T. M. Raeder,¹ P. E. Vullum,² and T. Grande^{1,a)}

AFFILIATIONS

¹Department of Materials Science and Engineering, NTNU Norwegian University of Science and Technology, NO-7491 Trondheim, Norway

²Department of Physics, NTNU Norwegian University of Science and Technology, NO-7491 Trondheim, Norway

^{a)}Author to whom correspondence should be addressed: grande@ntnu.no

ABSTRACT

Chemical solution deposition (CSD) is a versatile method to fabricate oxide films. Here, the structure and local variations in the chemical composition of BaTiO₃ (BTO) films prepared by CSD on (100), (110), and (111) SrTiO₃ (STO) substrates were examined by transmission electron microscopy. The films were shown to be epitaxial and the relaxation of the films occurred by the formation of edge dislocations at the substrate–film interfaces. The Burgers vectors of the dislocations were determined to be $a(010)$, $a[110]$ and $a[001]$, and $a(110)$ for the (100), (110), and (111) films, respectively. Due to the difference in thermal expansion between STO and BTO, the films are demonstrated to be under tensile strain. Furthermore, the boundaries between each deposited layer in the BTO films were found to be Ba-deficient in all cases. In the case of the (111) oriented film, defects like an anti-phase boundary or a thin layer with a twinned crystal structure were identified at the boundary between each deposited layer. Moreover, a larger grain was observed at the film surface with a twinned crystal structure. The interdiffusion length of A-cations at the STO–BTO interface, studied by electron energy-loss spectroscopy, was found to be 3.4, 5.3, and 5.3 nm for the (100), (110), and (111) oriented films, respectively. Interdiffusion of cations across the STO–BTO interface was discussed in relation to cation diffusion in bulk BTO and STO. Despite the presence of imperfections demonstrated in this work, the films possess excellent ferroelectric properties, meaning that none of the imperfections are detrimental to the ferroelectric properties.

Published under license by AIP Publishing. <https://doi.org/10.1063/5.0045011>

I. INTRODUCTION

BaTiO₃ (BTO) is known as one of the prototypic lead-free ferroelectric materials applied in electrical devices due to its excellent dielectric properties.¹ Bulk BTO has a tetragonal crystal structure at room temperature, with cell parameters $a = 3.993 \text{ \AA}$ and $c = 4.035 \text{ \AA}$, and a Curie temperature (T_c) of 120°C .² Typically, ferroelectric domains with 90° or 180° domain walls, located on pseudocubic $\{110\}$ and $\{100\}$ planes, respectively, are found in BTO, which can be observed either by optical or electron microscopy.³ Thin films have become increasingly more important in order to minimize the physical size and energy demand of electronic devices. BTO films can be deposited either by physical deposition techniques like pulsed laser deposition (PLD)^{4,5} or by chemical deposition techniques like chemical solution deposition (CSD).^{6,7}

Strain engineering of oxide ferroelectric films is a viable way of controlling and enhancing the functional properties, e.g., increasing the Curie temperature (T_c). There are multiple ways of straining a ferroelectric film. Most common for thin films grown via atomic layer-by-layer deposition is epitaxial strain engineering, utilizing the lattice parameter mismatch between the substrate and the thin film.^{8,9} In BTO grown on DyScO₃, the enhancement of ferroelectricity was demonstrated under compressive strain, where T_c was increased by about 500°C and the remnant polarization was increased by 250%.¹⁰ Coherent epitaxially strained BTO on SrTiO₃ (STO) is under compressive strain since the lattice parameter of BTO is larger than the lattice parameter of STO ($a_{\text{STO}} = 3.905 \text{ \AA}$). In this case, the polar c -axis points perpendicular to the film surface since this crystal orientation minimizes the lattice mismatch between the substrate and film. However, thin

films can only be strained epitaxially up to a certain film thickness, depending on the magnitude of the lattice mismatch, before dislocations are introduced and the crystal lattice of the film relaxes. In the case of BTO grown on (100) STO, it has been shown that the critical thickness is 5 nm or less.⁵

Another way of introducing strain is to utilize the difference in thermal expansion coefficient between the substrate and the film. This is known as thermal strain, and it was demonstrated that a tensile strain was introduced in thick BTO films (>200 nm) grown on STO, where the polar axis is aligned in-plane.⁶ The same films are subject to the present study. The dielectric and ferroelectric properties of these films have been reported in detail, including the determination of the domain pattern by piezoresponse force microscopy (PFM).¹¹ However, the structure and the effect of the CSD processing method on the film quality remain to be investigated.

Transmission electron microscopy (TEM) is a powerful tool, which can be used to investigate both structural and chemical properties down to the atomic scale. Here, we present a thorough study of the structure of BTO films on STO substrates. The BTO films, with the in-plane tensile strain, were synthesized by CSD on (100), (110), and (111) oriented STO substrates.¹¹ TEM was utilized to study how the CSD technique affects the structure and chemistry of the three differently oriented films at the nanoscale. Specifically, the degree of epitaxy and dislocations at the STO–BTO interface was studied by electron diffraction and imaging. Furthermore, local variations in chemical composition across the STO–BTO interface, as well in the interior of the BTO films, were investigated by electron energy-loss spectroscopy (EELS). Despite the present observations of several types of defects and inhomogeneities, the corresponding films possess excellent ferroelectric properties like high remnant polarization and enhanced T_c .¹¹

II. EXPERIMENTAL

A. BTO film processing

BTO films were prepared by aqueous CSD based on $\text{Ba}(\text{NO}_3)_2$ and Ti-isopropoxide cation precursors. Ethylenediaminetetraacetic acid (EDTA) and citric acid were used as complexing agents, and an ammonia solution was used to increase the pH. All chemicals were obtained from Sigma-Aldrich, St. Louis, MI, USA. The solution was adjusted to a concentration of 0.13 M and spin coated onto (100), (110), and (111) oriented STO substrates (Crystal GmbH, Berlin, Germany). In total, eight layers were deposited, where each layer was heat treated from ambient temperature with a heating rate of 100 °C/min to 450 °C, then at 50 °C/min to 550 °C, and lastly, at 20 °C/s to 1000 °C where it was held for 5 min after the deposition of each layer. The CSD process is described in further detail elsewhere.^{6,11}

B. TEM analysis

The TEM specimens were prepared using a FEI Helios G4 UX focused ion beam (FIB) with an EasyLift EX NanoManipulator. A carbon protection layer was deposited on top of the area of interest prior to ion-milling. The first part of the protection layer was deposited by electron beam assisted deposition to avoid any Ga^+

TABLE I. The orientations, along with the in-plane (IP) and out-of-plane (OOP) lattice parameters in the BTO films were measured. See Fig. 2 for indexed DPs.

Film	d_{IP}	$ d_{\text{IP}} $	d_{OOP}	$ d_{\text{OOP}} $
(100)	[010]	1	[100]	1
(110)	[110]	$\sqrt{2}$	[110]	$\sqrt{2}$
(111)	[112]	$\sqrt{6}$	[111]	$\sqrt{3}$

induced damage of the BTO film. Coarse thinning was performed at 30 kV acceleration voltage for the Ga^+ ions. In the final thinning steps, 5 kV and, lastly, 2 kV was used on either side of the lamella to minimize the thickness of the surface damaged layer.

The TEM analysis was carried out on a double Cs aberration corrected cold FEG JEOL ARM200F, operated at 200 kV. The ARM is equipped with a Quantum ER GIF for fast dual EELS. Diffraction patterns (DPs) were acquired using a selected area aperture where the substrate–film interface was placed approximately in the middle of the aperture such that diffraction from both the STO substrate and BTO film was included in each DP. The in-plane (IP) and out-of-plane (OOP) lattice parameters for all the differently oriented BTO films were measured by the software digital micrograph. The STO diffraction spots were used as internal references, assuming that the substrate lattice parameter equals that of single crystal STO. The orientations along which the in-plane and out-of-plane lattice parameters were measured are presented in Table I. In order to compare lattice parameters across differently oriented films, they are presented as $d/|d|$, where $|d|$ is the length of the unit vectors along different crystallographic axes, assuming a cubic symmetry. $|d|$ along the different crystallographic axes is included in Table I.

Scanning TEM (STEM) imaging was performed using a beam semi-convergence angle of 27 mrad. Bright-field STEM (BF-STEM) images were acquired with an outer semi-collection angle of 33 mrad, while the simultaneously acquired high-angle annular dark-field STEM (HAADF-STEM) images were taken with semi-collection angles of 51–203 mrad [Figs. 4, 5, 6, and 9(a)]. The other HAADF-STEM images [Figs. 1, 8, and 9(b)] were taken with semi-collection angles of 118–471 mrad to promote pure Z-contrast and minimize diffraction and strain contrast. STEM-EELS was performed with a beam current of 66 pA, a beam semi-convergence angle of 27 mrad, while the semi-collected angle into the GIF was 67 mrad. The HAADF-STEM images accompanying the EELS data were taken with semi-collection angles of 118–471 mrad. EELS maps were acquired with a step size of 0.4 Å with 0.01 s or 0.02 s dwell time in each probe position. The energy dispersion was 1 eV/ch. At the STO–BTO interface, the EELS maps were acquired between the misfit dislocations to minimize diffusion effects caused by the dislocations.

C. Data analysis

The EEL spectra were collected as maps and analyzed by the Gatan Digital Micrograph EELS Analysis package to determine the relative composition of Sr and Ba. Each compositional map was then binned perpendicular to the feature of interest for further analysis. The Python packages HyperSpy,¹² SciPy,¹³ and

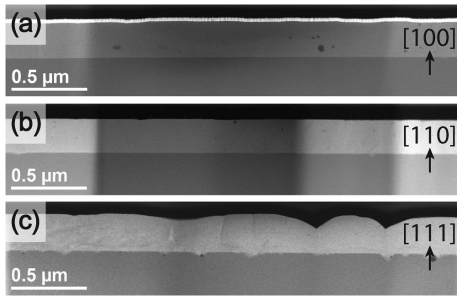


FIG. 1. HAADF-STEM images showing the cross section of the three differently oriented films (a) (100), (b) (110), and (c) (111). Vertical contrast differences occur because of varying lamella thickness, created by the FIB specimen preparation method. The (100) and (110) films show uniform thickness, whereas the thickness of the (111) oriented film varies. The thin, bright contrast layer directly above the BTO film in (a) is Pt/Pd that was sputter coated on top of the sample prior to FIB preparation in order to avoid charging.

Matplotlib¹⁴ were then used to load, fit, and plot the data, respectively. In order to determine the length scale of the interdiffusion of Sr and Ba at the substrate–film interface, and thereby determine the width of the interface, the four parameter logistic regression function in Eq. (1) was used as the mathematical model to fit the experimental concentration profiles of Sr and Ba,

$$f(x) = \frac{A - D}{1 + (x/C)^B} + D. \quad (1)$$

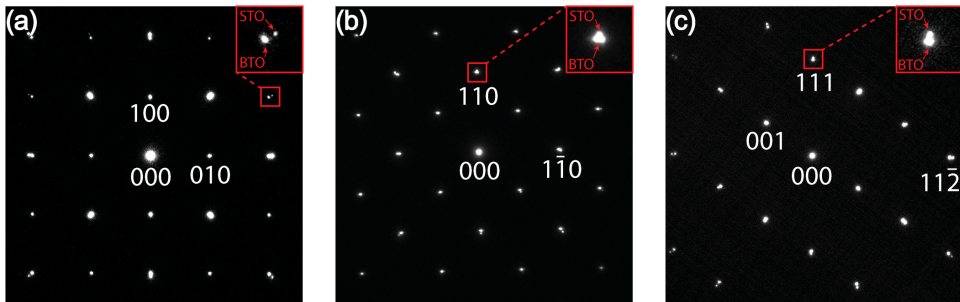


FIG. 2. SADPs from (a) (100), (b) (110), and (c) (111) oriented films and substrates. The DPs are rotated corresponding to Fig. 1, i.e., with the film surface pointing upward. The red boxes indicate a highlighted and enlarged set of BTO and STO diffraction spots for each film orientation. The STO spots are circular, while the BTO spots are somewhat non-circular and distorted.

Here, x is the independent variable and the parameters A , B , C , and D were fitted using non-linear least squares regression. The concentration profiles were then normalized based on this fit, assuming that STO and BTO were stoichiometric sufficiently far from the interface ($>3\text{--}4$ nm from the intersection of the two concentration profiles).

The interdiffusion distance was found by determining the distance from 0 to 1 normalized concentration for the Ba profiles, where the start and end points of the interdiffusion region were defined to be between 0.02 and 0.98 normalized concentration of Ba. Specimen drift during the acquisition of the EEL spectra was corrected by comparing the experimental and theoretical values of the lattice spacing along the interface normal in the HAADF-STEM images, which were acquired simultaneously with EEL spectra. The relative thickness t/λ was measured by EELS and found to be 0.7, 0.4, and 0.7, for the (100), (110), and (111) lamellae, respectively.

III. RESULTS

A. Film morphology and relaxed epitaxy

Scanning electron micrographs (Fig. S1, [supplementary material](#)) of the three BTO films demonstrated that the (100) and (110) BTO films possessed smooth surfaces, whereas the surface of the (111) BTO film was inhomogeneous with a pronounced roughness in certain areas. Cross-sectional TEM lamellae were prepared from arbitrary regions of (100) and (110) BTO films, and the cross-sectional lamella from the (111) film was prepared to include regions with both smooth and rough surfaces. HAADF-STEM images of the cross sections are shown in Fig. 1. The images of the (100) and (110) films demonstrate that they have a uniform thickness of $t = 230 \pm 4$ nm and $t = 218 \pm 2$ nm and that the thickness of the (111) film is less uniform: $t = 220 \pm 27$ nm. The selected area diffraction patterns (SADPs) from the three BTO films are shown in Fig. 2. The SADPs are rotated corresponding to

TABLE II. In-plane (IP) and out-of-plane (OOP) lattice parameters of the BTO films determined by TEM.

Film	IP $d \pm \Delta d$ (Å)	OOP $d \pm \Delta d$ (Å)
(100)	4.02 ± 0.01	4.02 ± 0.01
(110)	$(4.01 \pm 0.01)/\sqrt{2}$	$(4.00 \pm 0.01)/\sqrt{2}$
(111)	$(4.01 \pm 0.01)/\sqrt{6}$	$(4.01 \pm 0.01)/\sqrt{3}$

the orientations of the films in Fig. 1, i.e., with the film surface upward. Visible in all the SADPs is splitting between two sets of diffraction spots: One set corresponding to diffraction from STO, and the second set corresponding to the BTO film. The SADPs from the films and substrates show the same orientation, demonstrating that the films are epitaxial to the crystallographic orientation of the substrates. The splitting between the diffraction spots along all directions demonstrates that the films are relaxed compared to the substrates. The measured in-plane and out-of-plane lattice parameters are presented in Table II. All the in-plane and out-of-plane lattice parameters of the BTO films are intermediate to the a and c parameter of single crystal BTO, meaning that the films are under the tensile strain. This was also demonstrated by reciprocal space mapping of the same film system previously.^{6,11} In each diffraction pattern in Fig. 2, a pair of diffraction spots is enlarged and highlighted in the insets (red). For all films, the BTO spots are drawn out normal to the radial direction; however, the spread is only within 1° .

B. Periodic misfit dislocations and Burgers vectors

Figure 3 displays a BF-STEM image of the STO-BTO interface in the (100) film. Misfit dislocations, seen by strain contrast (highlighted by yellow arrows), are clearly present at the interface. The presence of dislocations at the STO-BTO interface evidence that the epitaxial strain due to lattice mismatch is relaxed by the formation of dislocations at the interface. Similar images for the (110) and (111) films are shown in Fig. S2, supplementary material. The distance between each dislocation is quite periodic, particularly, in the case of the (100) film, where the distance was found to be 14.5 ± 1.4 nm. In the case of the (110) and the (111) films, the periodic dislocations were imaged from two different orientations due to the in-plane anisotropy of the higher index substrates. In the (110) film the dislocation spacing was found to be 18.4 ± 2.5 nm

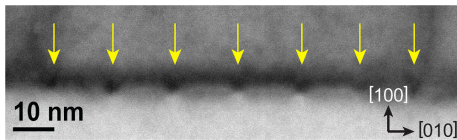


FIG. 3. BF-STEM image displaying strain contrast originating from misfit dislocations at the substrate-film interface in the (100) film.

and 15.2 ± 2.6 nm, when viewed along the beam direction $[00\bar{1}]$ and $[1\bar{1}0]$, respectively. In the (111) film, the dislocation spacing was found to be 15.7 ± 3.2 nm and 15.3 ± 4.4 nm, when viewed along the beam direction $[\bar{1}10]$ and $[11\bar{2}]$, respectively. In the case of the (111) film with beam direction $[11\bar{2}]$, the BF-STEM contrast was so poor that high-resolution images including two dislocations were acquired, and the distance between two and two dislocations were measured in multiple images.

A high-resolution HAADF-STEM image of the dislocations observed in the (100) film is shown in Fig. 4. Constructing a Burgers closure around the dislocation reveals that the Burgers vector is $a[010]$. Only dislocations with Burgers vector $a(010)$ were observed in the (100) film. Similar types of high-resolution HAADF-STEM images for the (110) and (111) films are shown in Figs. 5 and 6, where the dislocation-types which were most frequently observed are displayed. A few other types of dislocations, which were not analyzed further, were also observed. In the case of the (110) and (111) films, the dislocations are imaged from two different orientations to clarify the structural detail of the dislocations, as the Burgers vectors might have a component along the beam direction. Burgers closures were also constructed for the (110) and (111) films, and the projected Burgers vectors were determined to be $a[\bar{1}10]$ and $a[001]$ for the two different projections in the (110) film and $\frac{1}{2}a[11\bar{2}]$ and $a[\bar{1}10]$ for the two different projections in the (111) film. However, the $\frac{1}{2}a[11\bar{2}]$ Burgers vector is just a projection, i.e., it has a component parallel to the beam direction, as misfit dislocations in perovskite-based films usually have a perfect Burgers vector of $a(100)$ or $a(110)$.¹⁵ The atomic structures below

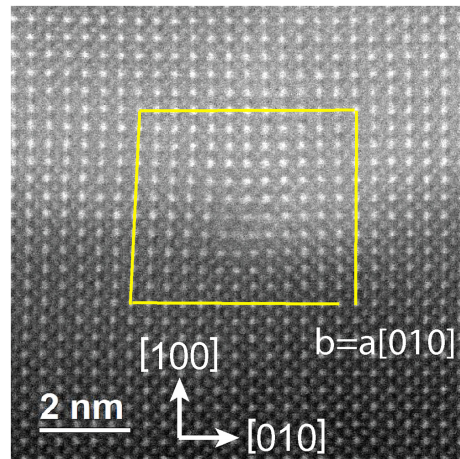


FIG. 4. High-resolution HAADF-STEM image displaying a misfit dislocation with the Burgers vector $\vec{b} = a[010]$ at the STO-BTO interface.

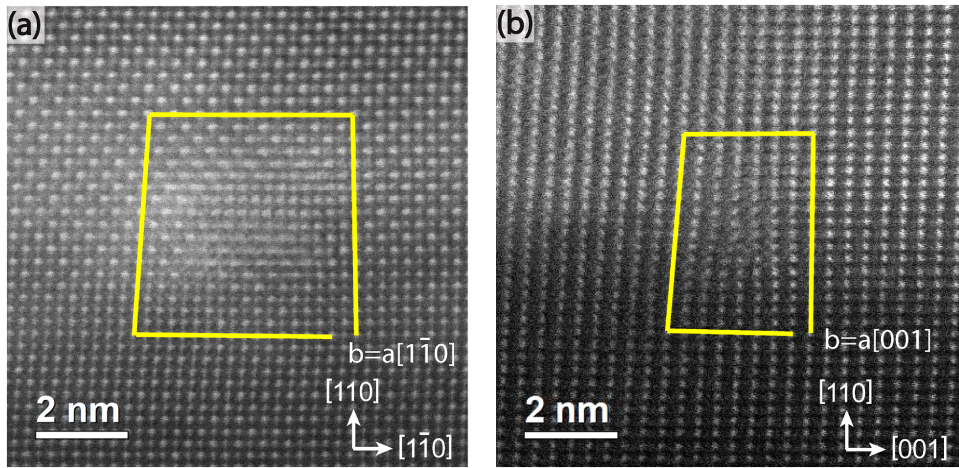


FIG. 5. High-resolution HAADF-STEM images of misfit dislocations in the (110) film imaged along the beam direction (a) $[00\bar{1}]$ and (b) $[1\bar{1}0]$. The Burgers closures demonstrate that the Burgers vectors are (a) $a[110]$ and (b) $a[001]$.

the images in Fig. 6 clarifies the possible Burgers vector, since it is determined as the only common possible Burgers vector based on the two images taken along two different crystallographic directions. In this case, the Burgers vector in the (111) film is $a(110)$.

C. Chemical analysis of the STO–BTO interface

Compositional analysis by EELS was performed across the STO–BTO interface. Representative normalized concentration profiles of Sr and Ba across this interface for the (100), (110), and (111) films are shown in Fig. 7. Measurements at six different locations in the (100) and (110) films, and four locations in the (111) film, give average interdiffusion distances of 3.4 ± 0.5 nm, 5.3 ± 1.4 nm, and 5.3 ± 0.2 nm, respectively. This means that the Sr/Ba interdiffusion extends over a length corresponding to 8–13 unit cells. This can be related to the diffusion constant D by the simple relation,

$$D = \frac{x^2}{\tau}, \quad (2)$$

where x is the interdiffusion distance and τ is the time the films were kept at high temperature during processing. Applying Eq. (2) to calculate the diffusion constants for the different orientations,

where $\tau = 5 \times 8$ min, gives

$$D_{100} = 4.8 \times 10^{-17} \text{ cm}^2/\text{s},$$

$$D_{110} = 1.2 \times 10^{-16} \text{ cm}^2/\text{s},$$

$$D_{111} = 1.2 \times 10^{-16} \text{ cm}^2/\text{s},$$

which is $\sim 10^2$ times lower than reported for Ba diffusion in bulk BTO¹⁶ and $\sim 10^4$ times higher than Sr diffusion in STO.¹⁷

D. Boundaries between spin-coated layers

The films were prepared by multiple spin coatings, and the individual layers formed by CSD could be identified by TEM. Figures 8(a), 8(c), and 8(e) shows HAADF-STEM images of a representative part of the cross section of the BTO films. Visible in these images are darker lines, which are parallel to the film surface. The thickness of each spin-coated layer is ~ 20 – 30 nm, and the dark lines correspond to the boundary between each spin-coated layer. High-resolution images of the areas are marked with blue boxes in Figs. 8(a), 8(c), and 8(e) are displayed in Figs. 8(b), 8(d), and 8(f). Clearly visible in the middle of all the high-resolution images is a band where the atomic columns have darker contrast. The Z-contrast of HAADF-STEM images indicate that the darker areas are layers with lower Ba contents. This was confirmed by EELS (Fig. S3, supplementary material), which demonstrates a significant Ba-deficiency in the boundary between each CSD layer

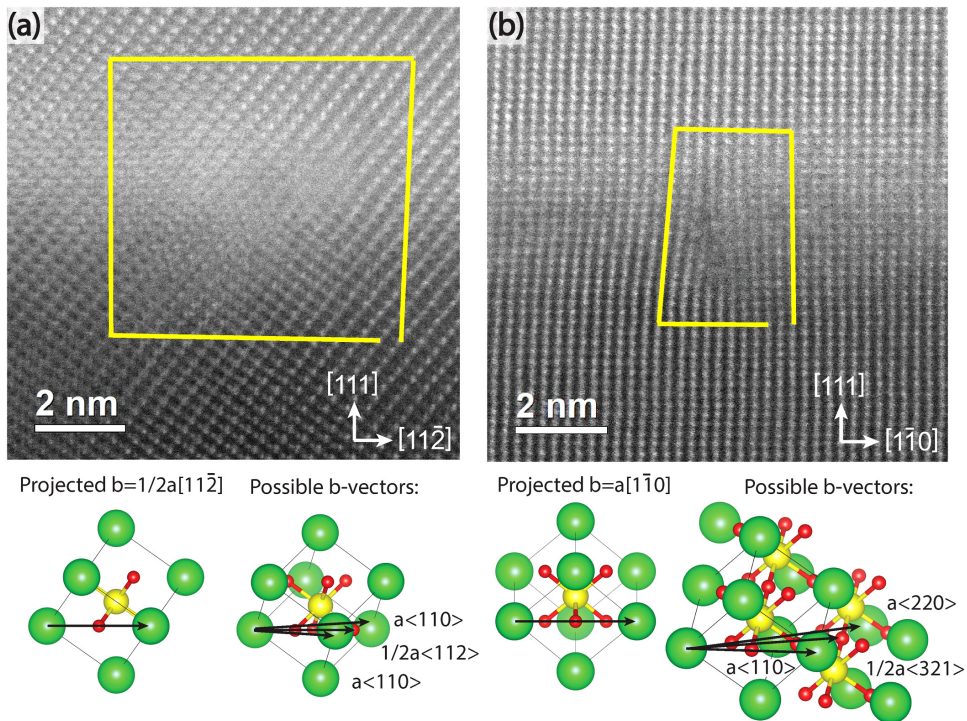


FIG. 6. High-resolution HAADF-STEM images of misfit dislocations in the (111) film imaged along the beam direction (a) $[110]$ and (b) $[11\bar{2}]$. Included are atomic structure figures, which elaborate on the possible Burgers vector for the misfit dislocations in the (111) film. Here, it is demonstrated that $\vec{b} = a\langle 110 \rangle$.

corresponding to the darker contrast in Fig. 8. It is also evident in Fig. 8 that the perovskite crystal remains intact without observable structural defects across the boundaries between the CSD layers. This was the case for all the thin dark lines observed in the (100) and (110) films but not for all cases of the (111) film.

Cross-sectional BF- and HAADF-STEM images of the (111) film are shown in Figs. 9(a) and 9(c), respectively. High-resolution HAADF-STEM images of the borderline between the CSD layers in the (111) film are displayed in Figs. 9(b) and 9(d) from the areas marked with blue boxes in Figs. 9(a) and 9(c). Here, the crystal structure is modified across the borderline between the two CSD layers. In Fig. 9(b), there is a thin layer where the crystal is twinned around the (111) plane compared to the rest of the film. In Fig. 9(d), the red dashed line follows an atomic column below the internal interface and a gap between atomic columns above. This is

known as an anti-phase boundary (APB), wherein the crystal structure remains the same on both sides of the boundary. It is, however, shifted by half a unit cell along the $[001]$ direction by crossing the APB.

Figure 9(e) shows a dark-field TEM (DF-TEM) image of the (111) film, acquired by centering the objective aperture around the 100 spot indexed with red in the diffraction pattern in Fig. 9(f). It is clearly visible that only a certain part of the film is bright in Fig. 9(e), meaning that this part of the film has a different crystallographic orientation than the rest of the film. This “grain” is twinned compared to the rest of the film, with the (111) plane as the twinning plane. All Bragg spots in the twinned grain (indexed in red) can be found by reflecting all Bragg spots from the rest of the film (indexed in white) along the (111) mirror plane, i.e., around the red dashed line shown in Fig. 9(f). The thin, twinned

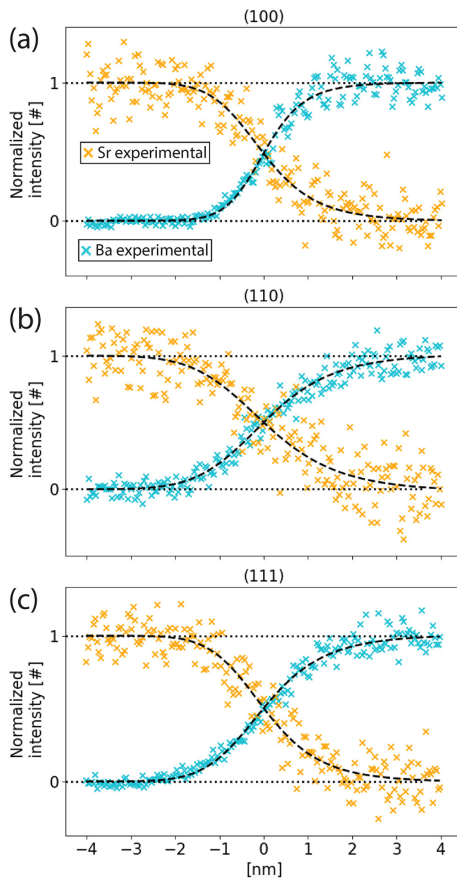


FIG. 7. Normalized Ba and Sr EELS profiles across the (a) (100), (b) (110), and (c) (111) oriented STO-BTO interfaces. Experimental values for Ba is shown in light blue, and experimental values are in orange for Sr. The black dashed lines are the fit from Eq. (1). Horizontal dotted lines are guides at normalized values of 0 and 1.

lamella seen in Fig. 9(b) at the boundary between two spin-coated layers has the same twinning as the larger grain observed in Fig. 9(e). The crystallographic relationship between the film and the grain is also equivalent to a 60° rotation around the [111] axis. A few other defects were observed in the films, e.g., voids visible in

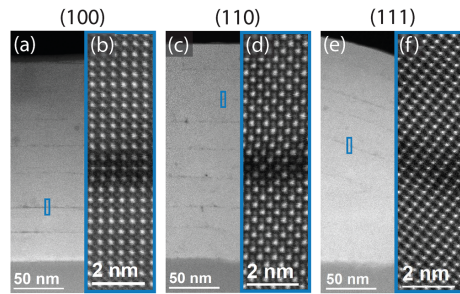


FIG. 8. Z-contrast HAADF-STEM images showing darker layers in the (100) (a) and (b), (110) (c) and (d), and (111) (e) and (f) BTO film.

Figs. 1(a) and 1(b). They were not studied further and are not included in this work.

IV. DISCUSSION

A. Epitaxy, strain state, and ferroelectric domains

Aqueous CSD is a simple, scalable, and environmentally friendly processing route for textured oxide films. It is further possible to tailor the degree of texture and the structure by controlling the heating profile and heating rate for pyrolysis and nucleation.¹⁸ The TEM work shown here demonstrates the nature of the structure and chemistry of BTO films prepared by CSD, including imperfections and defects. Despite these imperfections, the epitaxial films possess impressive ferroelectric properties,¹¹ meaning that none of the imperfections is detrimental to the ferroelectric properties.

For example, it is demonstrated that misfit dislocations are present and that the films are under tensile strain, which can be explained by the following: due to the difference in lattice parameter between STO and BTO, BTO is under compressive strain at the crystallization temperature of 1000 °C. Each spin-coated layer is much thicker than the critical thickness for coherently strained BTO on STO,⁵ and thus, the film is relaxed by misfit dislocations. During cooling, the thermal contraction of STO is smaller than for BTO.² Hence, if the misfit dislocations are pinned and cannot move, BTO will experience a gradually increasing tensile strain caused by the STO substrate.⁵ At the ferroelectric phase transition temperature, the long polar axis will align parallel to the STO-BTO interface in order to minimize the tensile strain. In the (100) film, polarization along [010] and [001] will be equivalent, and a 90° domain pattern is formed. Similarly, macroscopic polarization is aligned mainly in-plane in the (110) and (111) films, with a more complicated domain pattern.¹¹ This demonstrates an alternative route for strain engineering of thin films, where changing either the crystallization temperature or choosing substrates with different thermal expansion coefficients is a way of controlling the amount

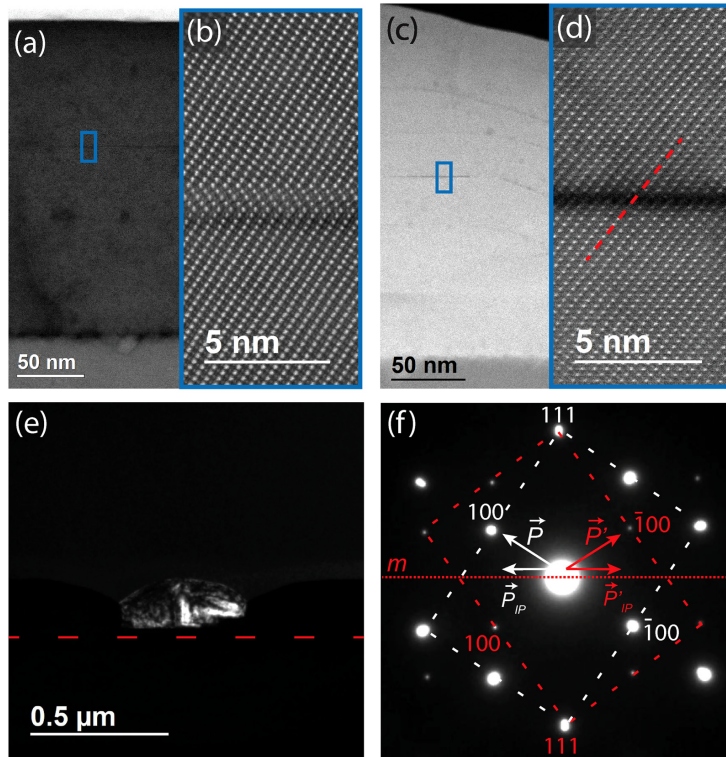


FIG. 9. Interfaces and grain only observed in the (111) oriented film. (a) BF-STEM image of the cross section of the (111) film, where a darker horizontal line is observed and marked with a blue rectangle, (b) magnification of the area in the blue rectangle in (a) where a thin crystallographic twin layer is observed. (c) HAADF-STEM image showing a clear dark horizontal line, which is marked with a blue square and magnified in (d) where an APB is present. (e) DF-TEM image acquired from the 100 spot marked with red in the DP in (f). The red dashed line in (e) indicates the substrate-film interface. Also indicated in the DP (f) is the mirror relation between the film (indexed with white) and the grain (indexed with red).

of strain introduced in the film and thus also affecting the polarization state of the film.

It was not possible to observe splitting between diffraction spots from different domains in these films, as demonstrated by the diffraction patterns taken by only including the film in the selected area aperture in Figs. S4, S5, and S6, [supplementary material](#). This is likely due to the very similar in-plane and out-of-plane lattice parameters. The shape of the diffraction spots (in the red boxes in Fig. 2) evidences a broadening in the 120, 110, and 111 BTO spots in the (100), (110), and (111) oriented films, respectively, which is

suggested to be connected to the ferroelectric domain structure of the films.

B. Periodic misfit dislocations and Burgers vectors

The theoretical spacing S between the edge dislocations in a film on a rigid substrate can be calculated by

$$S = b/(\delta - \epsilon), \quad (3)$$

where b is the in-plane component of the Burgers vector perpendicular to the line direction \vec{l} of the misfit dislocation, $\delta = (a_f - a_s)/a_s$ is the misfit parameter between the film (a_f) and substrate (a_s), and ϵ is the residual in-plane strain present in the film.¹⁹ In order to analyze the dislocation spacing, the line direction \vec{l} of the misfit dislocation must be known. The dislocation core will look sharp if the line direction is viewed “edge-on,” i.e., when the dislocation line is the same as the beam viewing direction.²⁰ This is the case for the misfit dislocations found in the (100) film, where the line direction is determined as $\vec{l} = \langle 001 \rangle$ and the misfit dislocation is of pure edge type, where the Burgers vector is always perpendicular to the line direction. Assuming that there were no residual strains present in the film at the crystallization temperature, the theoretical spacing between the edge dislocations (calculated at 1000 °C, and corrected by thermal expansion to room temperature values) would be 15.6 nm, where lattice parameters for STO and BTO at 1000 °C is taken from the work by Taylor.² The experimental value fits the theoretical value within the standard deviation, demonstrating that the film is relaxed by the introduction of edge dislocations. Langjahr *et al.*²¹ have grown the perovskite SrTi_{0.5}Zr_{0.5}O₃ (STZO) on STO by CSD and heat treated it at 1000 °C for 1 h. STZO-STO has approximately the same lattice mismatch as BTO-STO, and it was also shown that the Burgers vector in the STZO-STO system were of $a\langle 010 \rangle$ -type, with the line direction of $\langle 001 \rangle$. Giving the same theoretical dislocation spacing for a relaxed film, and a measured spacing of 16.1 ± 5.4 nm, demonstrating that the simple relation in Eq. (3) holds for relaxed films across different chemical compositions.

For the (110) film, the line direction is clearly viewed “edge-on” for beam, and hence, line direction $[1\bar{1}0]$ [Fig. 5(b)]. The dislocation core for the beam direction $[00\bar{1}]$ also looks fairly sharp [Fig. 5(a)], so it is also determined as a line direction, where the strong lattice distortion around the dislocation is assumed to be the cause for the blurring in the image.²² This means that the (110) film has two types of misfit dislocations, each with different line direction and Burgers vectors. The line directions are perpendicular to each other, and the respective Burgers vectors are of pure edge type, which relax the in-plane strain in the two anisotropic orthogonal directions in the (110) film. First, $\vec{l} = [00\bar{1}]$ and $\vec{b} = a[110]$ gives a theoretical dislocation distance of 22.0 nm, and $\vec{l} = [1\bar{1}0]$ and $\vec{b} = a[001]$ gives a theoretical dislocation distance of 15.6 nm, where calculations were performed the same way as described previously. The experimental values are 18.4 ± 2.5 nm and 15.2 ± 2.6 nm, respectively, demonstrating that strain is also relaxed due to the introduction of edge dislocations in the (110) film. Dislocations are observed to occur more frequent than the theoretical prediction for $\vec{b} = [1\bar{1}0]$, this might, for example, be caused by a small miscut angle of the substrate. The situation for the (110) STO-BTO system here is different from the dislocation system observed in the (110) Nd_{0.45}Sr_{0.55}MnO₃ film on STO, where misfit dislocations were found along the interface with line directions of both $\langle 111 \rangle$ and $\langle 001 \rangle$, with the Burgers vector of $a\langle 110 \rangle$ -type.²⁰

Tang *et al.* performed an analysis of the formation mechanism of misfit dislocations with the Burgers vector of $a\langle 110 \rangle$ on (111) oriented perovskites, which infers that the misfit line directions should run along the $\langle 112 \rangle$ directions.²⁰ This is further

TABLE III. Summary of the pure edge components of the Burgers vectors and line directions, and the dislocation spacing in the three differently oriented films. See text for decomposition of the Burgers vector in the (111) film.

Film	Burgers vector (edge component)	Line direction	S _{theory} (nm)	S _{experiment} (nm)
(100)	$a\langle 010 \rangle$	$\langle 001 \rangle$	15.6	14.5 ± 1.4
(110)	$a[110]$ $a[001]$	$\langle 001 \rangle$ $[1\bar{1}0]$	22.0 15.6	18.4 ± 2.5 15.2 ± 2.6
(111)	$\frac{1}{2}a[110]$	$[112]$	11.0 ^a	15.3 ± 4.4

^aSee text for explanation of deviation.

demonstrated by Xu *et al.* for (111)PbTiO₃ (PTO) on LaAlO₃ (LAO),¹⁵ and it is also shown here in Fig. 6(b) that the dislocation core is sharp (i.e., viewed “edge-on”) when viewed along $[112]$. Taking $a[011]$ as an example for the Burgers vector in the (111) film, it can be decomposed as

$$a[011] = \frac{1}{2}a[110] + \frac{1}{2}a[1\bar{1}2], \quad (4)$$

where $\frac{1}{2}a[110]$ is perpendicular to the direction of the dislocation line and $\frac{1}{2}a[1\bar{1}2]$ is parallel to the direction of the dislocation line. Meaning that the former is a pure edge component that could relax lattice mismatch along $\langle 110 \rangle$ planes, while the latter is a pure screw component that could relax shear strains.¹⁵ Calculating the theoretical spacing between edge dislocations with $\vec{b} = \frac{1}{2}a[110]$ gives $S = 11$ nm, whereas the measured dislocation density in the (111) film is 15.7 ± 3.2 nm and 15.3 ± 4.4 nm, when viewed along the beam direction $[1\bar{1}0]$ and $[112]$, respectively. The deviation between theoretical and measured distances can be explained by the fact that the $\langle 112 \rangle$ directions have a threefold symmetry in the (111) film, meaning that $[211]$ and $[121]$ are not perpendicular to $[112]$. The misfit dislocations with Burgers vectors along the respective $\langle 110 \rangle$ directions for line directions $[211]$ and $[121]$ will, therefore, have a component that contributes to in-plane relaxation along $[110]$. Consequently, to relax the film completely, fewer dislocations are needed, thus the distance between them becomes larger, which is what is measured for the (111) film. The discussion of the dislocations observed in this work is summarized in Table III.

C. Chemical abruptness at perovskite hetero-interfaces

The diffusion constants calculated for the Sr–Ba interdiffusion at the substrate–film interface are intermediate to the values for Ba diffusion in BTO¹⁶ and Sr diffusion in STO,¹⁷ demonstrating that the interface width of hetero-interfaces in perovskites can be estimated by the knowledge of A-cation diffusion constants in the native materials. Cation diffusion in perovskites is mediated by A-cite vacancies,^{17,23} thus to explain the difference in diffusion constant which is observed between the differently oriented films, the possible paths from one A-site to a vacant A-site in the lattice must be considered. A schematic representation of the possible diffusion paths is shown in Fig. 10. Figure 10(a) shows a 3D sketch of the perovskite unit cell, with three possible straight paths labeled I,

II, and III, which are perpendicular to the interfaces of the (100), (110), and (111) films, respectively. Path I is an unobstructed path, whereas path II is obstructed by the O-anion, and path III is obstructed by the Ti-cation. Assuming that the most likely diffusion path is along $\langle 100 \rangle$, i.e., along the family of path I, as this is an unobstructed path, and taking only a simple jump mechanism into account, one, two, and three jumps would be necessary to cover a distance of a , $\sqrt{2}a$, and $\sqrt{3}a$, normal to the surface of the (100), (110), and (111) films, respectively. This means that the length covered relative to the number of jumps needed is the longest for the (100) film, i.e., the diffusion length for the (100) is expected to be the longest. However, the shortest interdiffusion distance is measured for (100). It is worth noting that the relative thickness t/λ of the TEM lamellae were similar and reasonably low for all the three cases, with values of 0.7, 0.4, and 0.7 for the (100), (110), and (111) films, respectively. This implies that artificial broadening of the interdiffusion due to the lamella thickness is most severe in the (100) and

(111) films. Taking beam broadening into account, the interdiffusion lengths Δ in the order of size have this relation: $\Delta_{110} > \Delta_{111} > \Delta_{100}$. Demonstrating that taking only jumps along $\langle 100 \rangle$ into account is not sufficient to properly describe the orientational dependence on the interdiffusion length. The jump possibility along $\langle 100 \rangle$ was also assumed to be the same for all the films/substrates. However, as this diffusion mechanism relies on A-site vacancies in both BTO and STO, the concentration of these vacancies is crucial to the rate of diffusion. Among others, surface termination may affect the number of Sr vacancies in the different substrates.

D. Internal boundaries in all films and structural distortions specific to the (111) film

Thin, Ba-deficient layers are observed at the interfaces between the spin-coated layers in all the BTO films (Fig. 8), irrespective of STO orientation. This is an interesting observation,

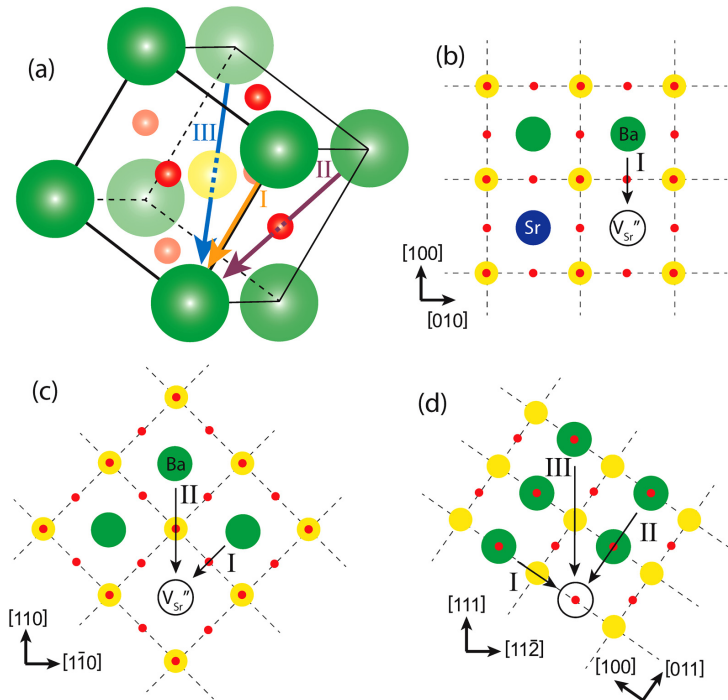


FIG. 10. Possible diffusion paths in the perovskite structure. (a) Schematic showing possible paths in a 3D sketch. I along the cube edge, II along the cube face diagonal, and III along the cube body diagonal. (b), (c), and (d) are 2D sketches of the (100), (110), and (111), respectively, with potential diffusion paths indicated.

which can be due to Ba-deficiency introduced during processing of the films. Between each layer, the BTO surface was exposed to air at 1000 °C before this surface was coated with the next BTO layer, and the thermal processing was repeated. Each layer is approximately 20–30 nm thick, and we propose that the lower Ba-content at the boundary between each layer originates from the loss of BaO at the outer surface in each thermal processing step. BaO-loss is well known in bulk BaZrO₃,^{24,25} and the present work indicates that BaO-loss is also taking place at temperatures as low as 1000 °C. Over time, the Ba-deficiency should diminish due to diffusion of Ba, but the relatively short time at 1000 °C during processing is not sufficient to allow for that. A-site deficiency is also a well-known phenomenon in other ferroelectric oxides such as BiFeO₃ (loss of Bi₂O₃),²⁶ PZT (loss of PbO),²⁷ and KNbO₃ (loss of K₂O).²⁸ Similar dark lines can also be observed in the bottom half of the BTO film deposited by CSD on Si(001) with a 2 nm template layer of STO in the work by Edmondson *et al.*⁷

A potential explanation for the occurrence of the APB in the (111) film [Fig. 9(d)] could be that after each spin-coated layer and successive heat treatment, many surface and near-surface defects are introduced, including Ba-vacancies (as demonstrated previously). In order to compensate for these Ba-vacancies, at an atomic level, Ti⁴⁺ takes the place of Ba²⁺ and the unit cell thus shifts by half in the $\langle 100 \rangle$ direction. It is worth noting that an APB does not affect ferroelectric properties, as it is purely translational in nature.

Regarding the thin twin layer and the twinned grain in the (111) film, they are suggested to originate due to the same mechanism. It is previously demonstrated in perovskites (SrRuO₃, BTO, and PZT) that twins which are rotated 60° around the [111] axis occur frequently in thin films grown on substrates with large lattice mismatch, which is also the case for the STO–BTO films studied here. The twin occurs due to stacking faults, where each successive (111) plane is translated by $\frac{1}{3}[112]$. If the crystal twins such that the A–O planes (in an ABO₃ perovskite) form the twin interface, as is evident in Fig. 9(b), the BO₆ octahedra are preserved.²⁹ Furthermore, twins can relax strain and affect the total net polarization in the thin film. Assuming that the polarization lies along the principal axes in the BTO film, one possibility is that the polarization changes from P to P' , as indicated in Fig. 9(f), i.e., the in-plane component of the ferroelectric polarization changes direction by 180° by crossing the twin domain wall. In Fig. 9(f), it is demonstrated for polarization along the pseudo-cubic [100] direction. However, the same arguments hold if the polarization should be along the pseudo-cubic [010] or [001] directions. Hence, twinning can cancel out or reduce the macroscopic in-plane polarization, while the macroscopic out-of-plane polarization is invariant with respect to twinning. Another possibility is for P' to point toward 100 (red index) instead of $\bar{1}00$ (red index). Then, out-of-plane polarization would be affected, whereas in-plane polarization would remain invariant. In conclusion, twinning affects the macroscopic net polarization of the film.

V. CONCLUSION

CSD was demonstrated to be a viable route to produce high-quality epitaxial BTO films on (100), (110), and (111) oriented STO substrates. The films were relaxed by edge dislocations, which

are semi-periodically spaced across the substrate–film interface. The most frequently observed Burgers vectors were determined as $a\langle 010 \rangle$, $a[110]$ and $a\langle 001 \rangle$, and $a\langle 110 \rangle$ for the (100), (110), and (111) film, respectively. The films are under tensile strain due to the difference in thermal expansion between STO and BTO. Comparing the measured dislocation distances to the theoretical values calculated based on the Burgers vectors, it was demonstrated that the films are fully relaxed by the introduction of the dislocations. In the (100) and (110) films, only pure edge dislocations were observed, whereas a Burgers vector with both an edge component and a screw component was observed in the (111) film. The Sr/Ba interdiffusion distance at the interface was measured by EELS to be 3.4, 5.3, and 5.3 nm for the (100), (110), and (111) oriented films, respectively. Based on Ba-cation diffusion in BTO and Sr-cation diffusion in STO, the interdiffusion width is of expected size. It was demonstrated that the boundary between each spin-coated layer of BTO was Ba-deficient, meaning that BaO is volatile at 1000 °C during thermal processing of the BTO films. In case of the (111) film, an APB and a thin twin crystal was observed at the boundary between each spin-coated layer, as well as a grain with a twin crystal structure growing all the way to the surface. The APB is suggested to accommodate charge imbalance at the highly defective surface, and twins can minimize the macroscopic polarization of the film.

SUPPLEMENTARY MATERIAL

See the [supplementary material](#) for SEM images of the film surfaces (Fig. S1), BF-STEM images of dislocation densities in the (110) and (111) film (Fig. S2), EELS scans across Ba-deficient boundaries (Fig. S3), and SADPs from multiple sites within the films (Figs. S4, S5, and S6).

AUTHORS' CONTRIBUTIONS

I.-E.N. performed all the TEM work with supervision from P.E.V. and T.G. T.M.R. synthesized the films. I.-E.N. wrote the manuscript under supervision of T.G. and with contributions from all the authors.

ACKNOWLEDGMENTS

The Research Council of Norway is acknowledged for financial support through the Projects FASTS (No. 250403/F20) and BORNIT (275139/F20) and for supporting the Norwegian Micro- and Nano-Fabrication Facility, NorFab (295864) and the Norwegian Center for Transmission Electron Microscopy, NORTEM (197405/F50). The authors would also like to thank Professor Mari-Ann Einarsrud for proof reading the manuscript.

DATA AVAILABILITY

The data that support the findings of this study are available from the corresponding author upon reasonable request.

REFERENCES

1. J. F. Scott, "Applications of modern ferroelectrics," *Science* **315**, 954–959 (2007).

- ²D. Taylor, "Thermal expansion data. VIII: Complex oxides, ABO₃, the perovskites," *Trans. J. Br. Ceram. Soc.* **84**, 181–188 (1985).
- ³Z. X. W. Yung, H. Hu, H. M. Chan, and M. P. Harmer, "Scanning electron microscopy and transmission electron microscopy study of ferroelectric domains in doped BaTiO₃," *J. Am. Ceram. Soc.* **69**, 594–602 (1986).
- ⁴A. S. Everhardt, T. Denneulin, A. Grünebohm, Y.-T. Shao, P. Ondrejovic, S. Zhou, N. Domingo, G. Catalan, J. Hlinka, J.-M. Zuo, S. Matzen, and B. Noheda, "Temperature-independent giant dielectric response in transitional BaTiO₃ thin films," *Appl. Phys. Rev.* **7**, 011402 (2020).
- ⁵T. Suzuki, Y. Nishi, and M. Fujimoto, "Analysis of misfit relaxation in heteroepitaxial BaTiO₃ thin films," *Philos. Mag. A* **79**, 2461–2483 (1999).
- ⁶T. M. Raeder, K. Bakken, J. Glaum, M. A. Einarsrud, and T. Grande, "Enhanced in-plane ferroelectricity in BaTiO₃ thin films fabricated by aqueous chemical solution deposition," *AIP Adv.* **8**, 105228 (2018).
- ⁷B. I. Edmondson, S. Kwon, C. H. Lam, J. E. Ortmann, A. A. Demkov, M. J. Kim, and J. G. Ekerdt, "Epitaxial, electro-optimally active barium titanate thin films on silicon by chemical solution deposition," *J. Am. Ceram. Soc.* **103**, 1209–1218 (2019).
- ⁸D. G. Schlom, L.-Q. Chen, C.-B. Eom, K. M. Rabe, S. K. Streiffer, and J.-M. Triscone, "Strain tuning of ferroelectric thin films," *Annu. Rev. Mater. Res.* **37**, 589–626 (2007).
- ⁹A. R. Damodaran, J. C. Agar, S. Pandya, Z. Chen, L. Dedon, R. Xu, B. Apgar, S. Saremi, and L. W. Martin, "New modalities of strain-control of ferroelectric thin films," *J. Phys.: Condens. Matter* **28**, 263001 (2016).
- ¹⁰K. J. Choi, M. Biegalski, Y. L. Li, A. Sharan, J. Schubert, R. Uecker, P. Reiche, Y. B. Chen, X. Q. Pan, V. Gopalan, L.-Q. Chen, D. G. Schlom, and C. B. Eom, "Enhancement of ferroelectricity in strained BaTiO₃ thin films," *Science* **306**, 1005–1009 (2004).
- ¹¹T. M. Raeder, T. S. Holstad, I.-E. Nylund, M.-A. Einarsrud, J. Glaum, D. Meier, and T. Grande, "Anisotropic in-plane dielectric and ferroelectric properties of tensile-strained BaTiO₃ films with three different crystallographic orientations," *AIP Adv.* **11**, 025016 (2021).
- ¹²F. D. L. Peña, E. Prestat, V. T. Fauske, P. Burdet, P. Jokubauskas, M. Nord, T. Ostasevicius, K. E. MacArthur, M. Sarahan, D. N. Johnstone, J. Taillon, J. Lähnemann, V. Mignonov, A. Eljarrat, J. Caron, T. Aarholt, S. Mazzucco, M. Walls, T. Slater, F. Winkler, P. Quinn-Dils, B. Martineau, G. Donval, R. McLeod, E. R. Høglund, I. Alkneit, D. Lundebj, T. Henninen, Luiz Fernando Zagonel, and A. Garmannslund, "hyperspy/hyperspy: Hyperspy v1.5.2" (2019).
- ¹³P. Virtanen, R. Gommers, T. E. Oliphant, M. Haberland, T. Reddy, D. Cournapeau, E. Burovski, P. Peterson, W. Weckesser, J. Bright, S. J. van der Walt, M. Brett, J. Wilson, K. J. Millman, N. Mayorov, A. R. J. Nelson, E. Jones, R. Kern, E. Larson, C. J. Carey, I. Polat, Y. Feng, E. W. Moore, J. VanderPlas, D. Laxalde, J. Perktold, R. Cimrman, I. Henriksen, E. A. Quintero, C. R. Harris, A. M. Archibald, A. H. Ribeiro, F. Pedregosa, and P. van Mulbregt, "SciPy 1.0: Fundamental algorithms for scientific computing in python," *Nat. Methods* **17**, 261–272 (2020).
- ¹⁴J. D. Hunter, "Matplotlib: A 2D graphics environment," *Comput. Sci. Eng.* **9**, 90–95 (2007).
- ¹⁵Y. B. Xu, Y. L. Tang, Y. L. Zhu, Y. Liu, S. Li, S. R. Zhang, and X. L. Ma, "Misfit strain relaxation of ferroelectric PbTiO₃/LaAlO₃ (111) thin film system," *Sci. Rep.* **6**, 35172 (2016).
- ¹⁶R. Sažinas, I. Sakaguchi, M.-A. Einarsrud, and T. Grande, "¹³⁴Ba diffusion in polycrystalline BaMO₃ (M = Ti, Zr, Ce)," *AIP Adv.* **7**, 115024 (2017).
- ¹⁷K. Gömann, G. Borchardt, M. Schulz, A. Gömann, W. Maus-Friedrichs, B. Lesage, O. Kaitasov, S. Hoffmann-Eifert, and T. Schneller, "Sr diffusion in undoped and La-doped SrTiO₃ single crystals under oxidizing conditions," *Phys. Chem. Chem. Phys.* **7**, 2053–2060 (2005).
- ¹⁸K. Bakken, A. B. Blichfeld, D. Chernyshov, T. Grande, J. Glaum, and M.-A. Einarsrud, "Mechanisms for texture in BaTiO₃ thin films from aqueous chemical solution deposition," *J. Solgel. Sci. Technol.* **95**, 562–572 (2020).
- ¹⁹Y. Ikuhara and P. Pirouz, "High resolution transmission electron microscopy studies of metal/ceramics interfaces," *Microsc. Res. Tech.* **40**, 206–241 (1998).
- ²⁰Y. Tang, Y. Zhu, H. Meng, Y. Zhang, and X. Ma, "Misfit dislocations of anisotropic magnetoresistant Nd_{0.45}Sr_{0.55}MnO₃ thin films grown on SrTiO₃ (110) substrates," *Acta Mater.* **60**, 5975–5983 (2012).
- ²¹P. Langjahr, F. Lange, T. Wagner, and M. Rühle, "Lattice mismatch accommodation in perovskite films on perovskite substrates," *Acta Mater.* **46**, 773–785 (1998).
- ²²C. L. Jia, S. B. Mi, K. Urban, I. Vrejoiu, M. Alexe, and D. Hesse, "Effect of a single dislocation in a heterostructure layer on the local polarization of a ferroelectric layer," *Phys. Rev. Lett.* **102**, 117601 (2009).
- ²³R. Sažinas, I. Sakaguchi, I. Hasle, J. M. Polfus, R. Haugsrud, M.-A. Einarsrud, and T. Grande, "Tracer diffusion of ⁹⁶Zr and ¹³⁴Ba in polycrystalline BaZrO₃," *Phys. Chem. Chem. Phys.* **19**, 21878–21886 (2017).
- ²⁴R. Sažinas, C. Bernuy-López, M.-A. Einarsrud, and T. Grande, "Effect of CO₂ exposure on the chemical stability and mechanical properties of BaZrO₃-ceramics," *J. Am. Ceram. Soc.* **99**, 3685–3695 (2016).
- ²⁵R. Sažinas, M.-A. Einarsrud, and T. Grande, "Toughening of Y-doped BaZrO₃ proton conducting electrolytes by hydration," *J. Mater. Chem. A* **5**, 5846–5857 (2017).
- ²⁶S. M. Selbach, M.-A. Einarsrud, T. Tybell, and T. Grande, "Synthesis of BiFeO₃ by wet chemical methods," *J. Am. Ceram. Soc.* **90**, 3430–3434 (2007).
- ²⁷M. Kosec, B. Malic, and M. Mandeljc, "Chemical solution deposition of PZT thin films for microelectronics," *Mater. Sci. Semicond. Process.* **5**, 97–103 (2002).
- ²⁸N. H. Gaukás, S. M. Dale, T. M. Ræder, A. Tøresen, R. Holmestad, J. Glaum, M.-A. Einarsrud, and T. Grande, "Controlling phase purity and texture of K_{0.5}Na_{0.5}NbO₃ thin films by aqueous chemical solution deposition," *Materials* **12**, 2042 (2019).
- ²⁹K. P. Fahey, B. M. Clemens, and L. A. Wills, "Nonorthogonal twinning in thin film oxide perovskites," *Appl. Phys. Lett.* **67**, 2480–2482 (1995).

Supporting information

I.-E. Nylund,¹ T. M. Raeder,¹ P. E. Vullum,² and T. Grande¹

¹*Department of Materials Science and Engineering, NTNU Norwegian University of Science and Technology, NO-7491 Trondheim, Norway*

²*Department of Physics, NTNU Norwegian University of Science and Technology, NO-7491 Trondheim, Norway*

(Dated: 12 February 2021)

I. BTO FILM SURFACE

Figure S1 shows SEM images of the (100), (110), and (111) oriented film surfaces. The (100) and (110) films appear to have smooth surfaces whereas the (111) oriented film has a rougher surface morphology. Particularly, the (111) oriented film has areas where it appears as smooth as the other orientations and other areas with a rougher surface. TEM lamellae were made from arbitrary areas in (100) and (110) oriented films, whereas the TEM lamella was positioned to include both flat and rougher areas in the (111) oriented film.

II. PERIODIC EDGE DISLOCATIONS AND BURGER'S VECTORS IN THE (110) AND (111) FILMS

Figure S2(a) and (b) show BF-STEM images for the (110) film, with beam direction $[00\bar{1}]$, and $[1\bar{1}0]$, respectively. Figure S2(c) shows a BF-STEM image of the (111) film, with beam direction $[\bar{1}10]$. Misfit dislocations at the interface between STO and BTO are visible due to strain contrast creating dark spots which are marked by yellow arrows. The distance between each misfit dislocation were measured in Digital Micrograph. In the case of the (111) film with beam direction

$[11\bar{2}]$, there were poor contrast around the edge dislocations in the BF-STEM images, the distance between dislocations was therefore measured on high-resolution HAADF-STEM images where two dislocations were present.

III. EELS ACROSS BOUNDARIES BETWEEN LAYERS

EELS analysis was performed across the boundaries between the layers found in the BTO films. The EELS analysis indicated significant Ba-deficiency at the internal interfaces.

IV. SELECTED AREA DIFFRACTION TAKEN ONLY FROM THE BTO FILMS

The Jeol JEM 2100 with a LaB_6 electron source was used to acquire multiple selected area diffraction patterns (SADPs) from the (100), (110), and (111) BTO films only, shown in Fig. S4, S5, and S6, respectively. The selected area aperture includes a circular area of the film with a diameter of ~ 160 nm. The (100) film was slightly damaged after handling, but the SADPs acquired showed high quality, so the sample was considered to be of sufficient quality for this analysis.

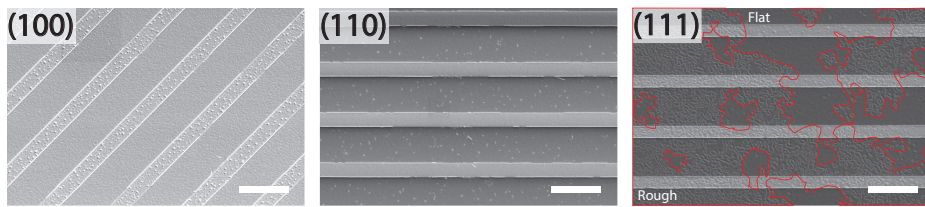


FIG. S1. SEM surface overview images. (100) and (110) show homogeneous smooth surfaces, while (111) shows areas of smooth surface and areas with a rougher surface morphology, separated by a drawn red line. The interdigitated electrodes used to measure P-E loops are visible on all film surfaces. The scale bars are 10 μm .

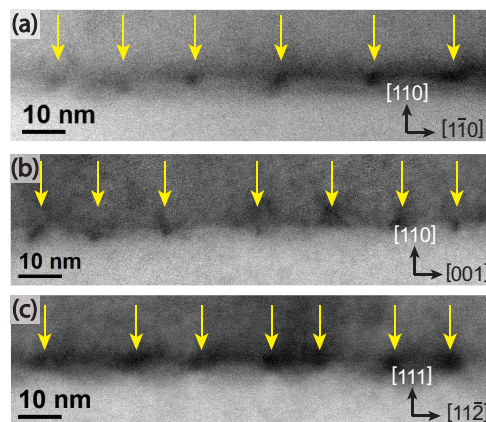


FIG. S2. Misfit dislocations visible at the STO-BTO interface due to strain contrast. (a) and (b) shows the two different projections of the (110) film, and (c) shows one projection of the (111) film.

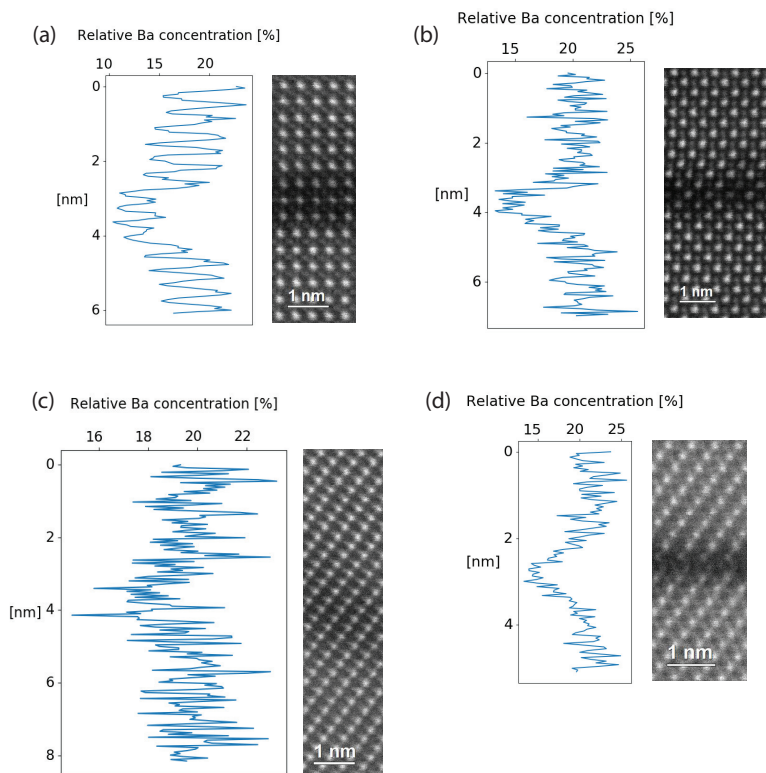


FIG. S3. HAADF-STEM images of the areas scanned during EELS analysis. The EELS signal is binned to one pixel in the horizontal direction and the relative Ba concentration is plotted next to each HAADF STEM image. (a) (100), (b) (110), (c) (111) where the crystal structure remains the same across the internal interface, and (d) across an APB in (111).

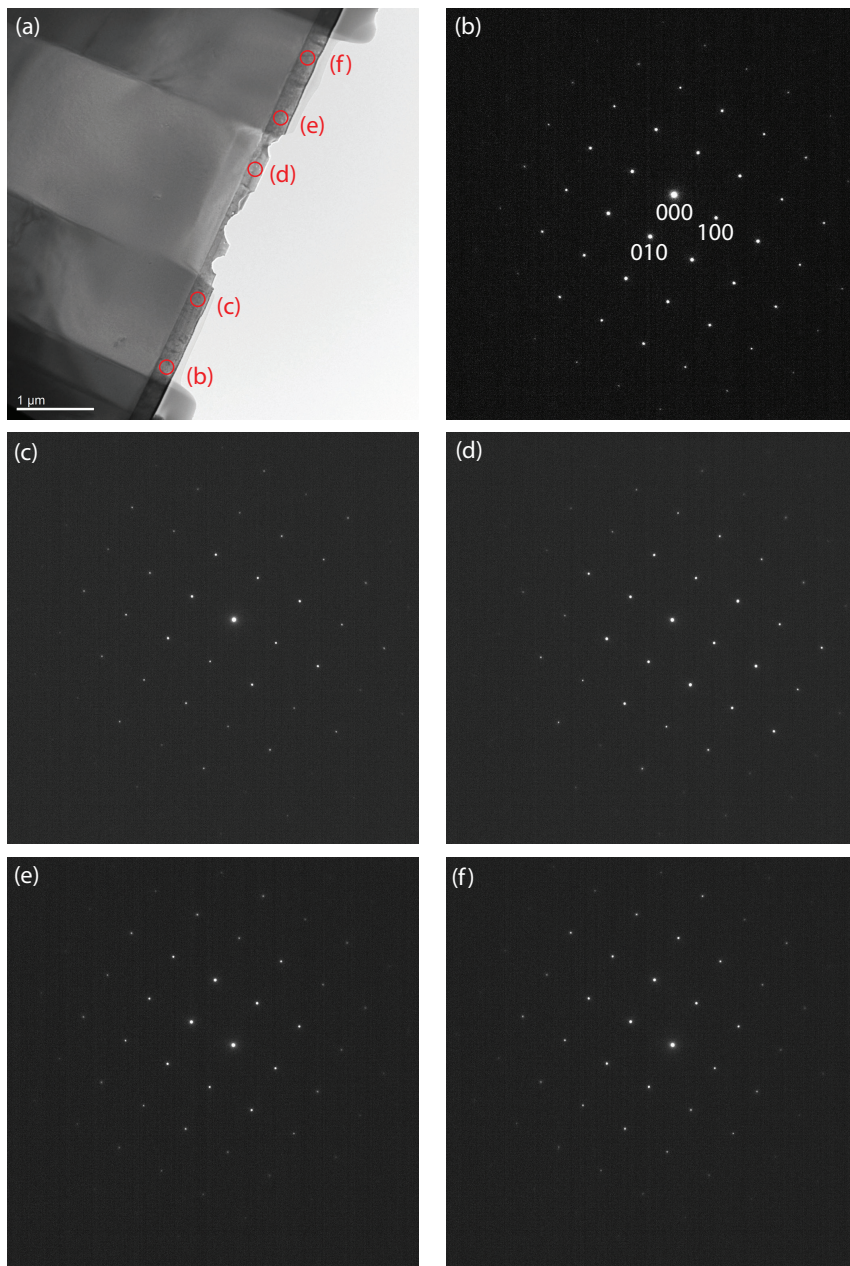


FIG. S4. (a) Bright-field image and (b-f) diffraction patterns from the (100) BTO film. The red circles indicate the selected area used in the different diffraction patterns.

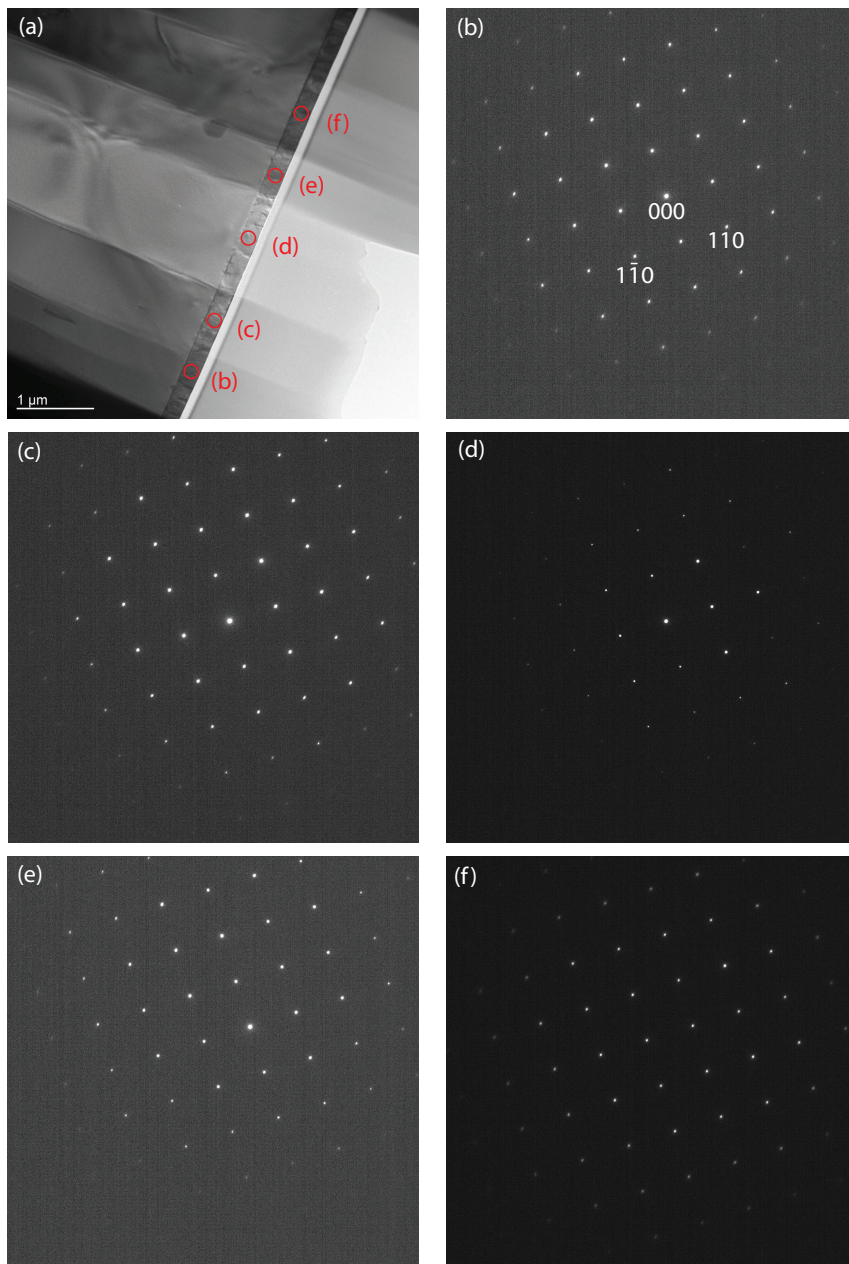


FIG. S5. (a) Bright-field image and (b-f) diffraction patterns from the (110) BTO film. The red circles indicate the selected area used in the different diffraction patterns.

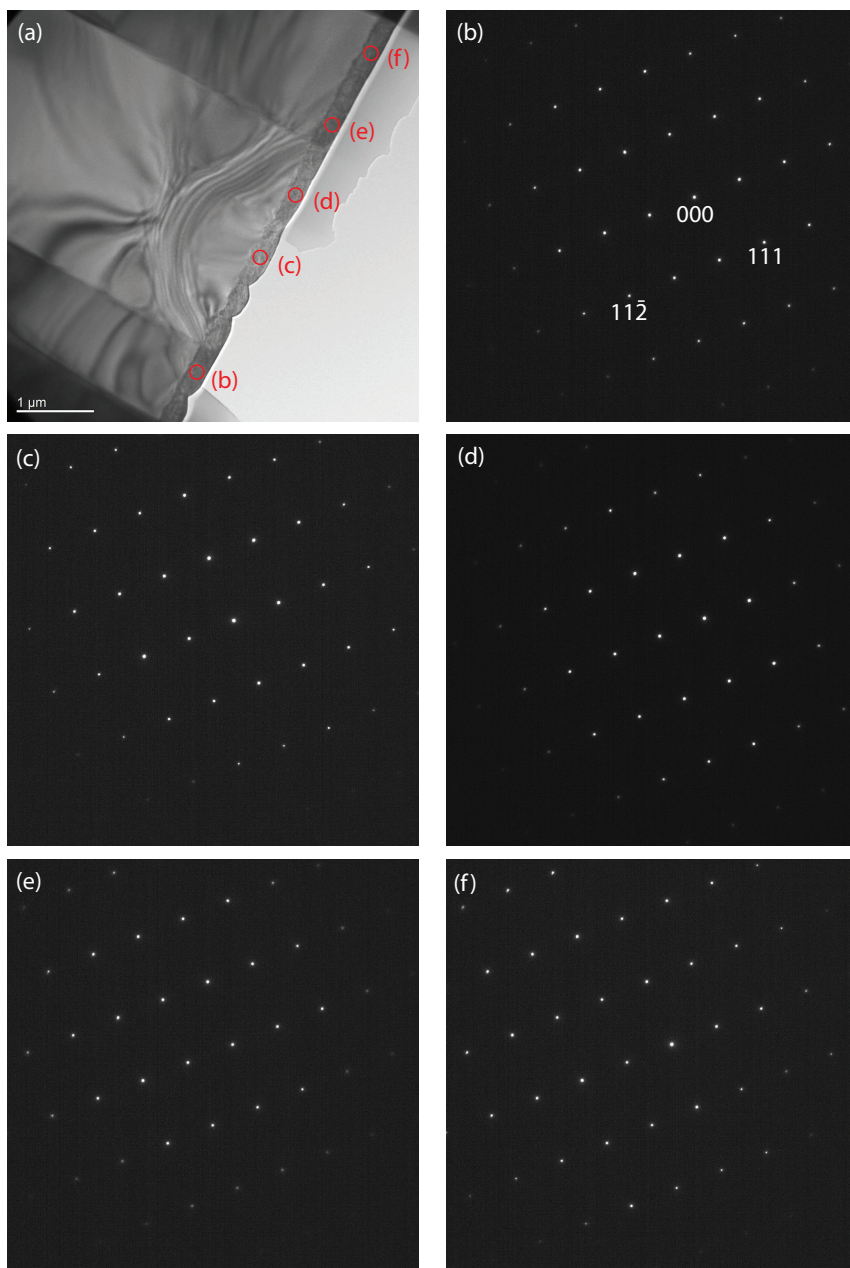


FIG. S6. (a) Bright-field image and (b-f) diffraction patterns from the (111) BTO film. The red circles indicate the selected area used in the different diffraction patterns.

Manuscript 1

Exploring the role of Bi 6s lone pair in tetragonal tungsten bronzes

$A_4\text{Bi}_2\text{Nb}_{10}\text{O}_{30}$ ($A=\text{Na, K, Rb}$)

Nylund, I.-E., Zeiger, C. R., Peng, D., Vullum, P. E., Walker, J., Einarsrud, M.-A., Grande, T.

To be submitted

This manuscript is awaiting publication and is not included in NTNU Open

Manuscript 2

Cation disorder in $\text{Ba}_4M_2\text{Nb}_{10}\text{O}_{30}$ ($M=\text{Na, K, Rb}$) tetragonal tungsten bronzes

Nylund, I.-E., Løndal, N. S., Walker, J., Vullum, P. E., Einarsrud, M.-A., Grande, T.

To be submitted

This manuscript is awaiting publication and is not included in NTNU Open

Manuscript 3

Scanning transmission electron microscopy of the improper ferroelectric
 $\text{Gd}_2(\text{MoO}_4)_3$

Nylund, I.-E.

Not intended for publication in its present form

This manuscript is awaiting publication and is not included in NTNU Open




Paper 2

Observation of cation-specific critical behavior at the improper ferroelectric phase transition in $\text{Gd}_2(\text{MoO}_4)_3$

Nylund, I.-E., Tsoutsouva, M., Grande, T., and Meier, D.

Physical Review Materials **6**, 034402 (2022)

Observation of cation-specific critical behavior at the improper ferroelectric phase transition in $\text{Gd}_2(\text{MoO}_4)_3$

Inger-Emma Nylund , Maria Tsoutsouva, Tor Grande , and Dennis Meier ^{*}

Department of Materials Science and Engineering, NTNU Norwegian University of Science and Technology, NO-7491 Trondheim, Norway



(Received 23 November 2021; accepted 10 February 2022; published 10 March 2022)

Gadolinium molybdate is a classical example of an improper ferroelectric and ferroelastic material. It is established that the spontaneous polarization arises as a secondary effect, induced by a structural instability in the paraelectric phase, which leads to a unit cell doubling and the formation of a polar axis. However, previous x-ray diffraction (XRD) studies on gadolinium molybdate have been restricted by the limited ability to include a wide 2θ range in the analysis, and thus, at atomic scale, much remains to be explored. By applying temperature-dependent XRD, we observe the transition from the paraelectric tetragonal phase to the orthorhombic ferroelectric phase. The ferroelastic strain is calculated based on the thermal evolution of the lattice parameters, and Rietveld refinement of the temperature-dependent data reveals that the displacement of different cations follows different critical behavior, providing insight into the structural changes that drive the improper ferroelectricity in gadolinium molybdate.

DOI: [10.1103/PhysRevMaterials.6.034402](https://doi.org/10.1103/PhysRevMaterials.6.034402)

I. INTRODUCTION

Gadolinium molybdate [$\text{Gd}_2(\text{MoO}_4)_3$] is a classical example for improper ferroelectricity, which has been studied intensively for more than half a century [1]. Improper ferroelectrics are a special class of electrically ordered materials, where the primary symmetry-breaking order parameter is not the electric polarization. Instead, the phase transition to the ferroelectric state is driven by a structural or magnetic instability, which breaks inversion symmetry and leads to the formation of a polar axis. In contrast to *proper* ferroelectrics, such as LiNbO_3 , BaTiO_3 , and $\text{Pb}(\text{Zr}_x\text{Ti}_{1-x})\text{O}_3$, ferroelectricity in improper systems only occurs as a secondary effect, promoting unusual correlation phenomena between spin, charge, and lattice degrees of freedom. In TbMnO_3 and MnWO_4 , for example, the emergence of a magnetically induced polarization gives rise to pronounced magnetoelectric and magnetocapacitance effects [2–5], and in hexagonal manganites RMnO_3 ($R = \text{Sc}, \text{Y}, \text{In}, \text{Dy}$ to Lu), geometrically driven ferroelectricity causes the formation of unusual domain wall structures and topologically protected domains [6,7].

In the model material $\text{Gd}_2(\text{MoO}_4)_3$, a structural instability in the paraelectric high-temperature phase leads to a doubling of the unit cell volume and a distortion of the unit cell. The latter leads to the formation of a polar axis, which is then accompanied by a spontaneous polarization, making $\text{Gd}_2(\text{MoO}_4)_3$ a uniaxial improper ferroelectric. The induced polarization is oriented along the crystallographic c axis as indicated in Fig. 1.

It is established that the paraelectric-to-ferroelectric transition in $\text{Gd}_2(\text{MoO}_4)_3$ is a first-order phase transition. This

is supported by dielectric [8] and neutron scattering [9] measurements, in addition to the observation of latent heat [10] and lattice parameter hysteresis [11] at the phase transition. The structural primary order parameter that drives the phase transition has been determined as a phonon instability at the $(\frac{1}{2}, \frac{1}{2}, 0)$ Brillouin zone corner of the tetragonal parent phase, leading to the unit cell doubling when this soft mode “freezes in” [9]. $\text{Gd}_2(\text{MoO}_4)_3$ can thus be categorized as a geometric improper ferroelectric [12].

Ferroelastic switching can be achieved by applying mechanical stress along the b axis and results in an exchange of the a and b axes of the material [13]. Because of the improper nature of the ferroelectric order, however, switching the strain state inevitably results in polarization reversal and vice versa by the application of an electric field, reflecting a one-to-one correlation between the ferroelastic and ferroelectric order [9]. Furthermore, $\text{Gd}_2(\text{MoO}_4)_3$ is birefringent [8,14], and as a result, the material has found application as optical shutters, which are either mechanically or electrically controlled, and a potential use in memory devices has been proposed [15]. Thus, in addition to the intriguing physics of the coupled ferroelastic and ferroelectric order in $\text{Gd}_2(\text{MoO}_4)_3$, the material displays unique functional properties, being of interest for both fundamental and applied sciences.

Crystallographically, $\text{Gd}_2(\text{MoO}_4)_3$ can exist in two modifications referred to as the α and β phases. The α phase is thermodynamically stable at room temperature and up to 857 °C, where it transforms to the stable high-temperature β phase. $\text{Gd}_2(\text{MoO}_4)_3$ can be retained in the metastable β phase by cooling back <857 °C, where transformation to the α phase is imperceptibly slow <600 °C [16,17].

β - $\text{Gd}_2(\text{MoO}_4)_3$ belongs to the tetragonal space group $P4_2m$ with $a = 7.39 \text{ \AA}$ and $c = 10.67 \text{ \AA}$ and 2 f.u. per unit cell [18]. The unit cell can be said to have a layered structure which consists of $(\text{MoO}_4)^{2-}$ tetrahedra and Gd^{3+}

^{*}dennis.meier@ntnu.no

cations in seven-coordinated oxygen polyhedra [1]. In the β phase, $\text{Gd}_2(\text{MoO}_4)_3$ is piezoelectric [9]. On cooling, $\beta\text{-Gd}_2(\text{MoO}_4)_3$ transforms at 159°C into the improper ferroelastic [9,19], improper ferroelectric [20] β' phase. This is the phase transition at which the abovementioned unit cell doubling occurs, and the β' phase belongs to the orthorhombic space group $Pba2$ with $a = 10.39 \text{ \AA}$, $b = 10.42 \text{ \AA}$, and $c = 10.70 \text{ \AA}$ [1,18]. In addition to the unit cell doubling, the $P\bar{4}2_1m$ and $Pba2$ space groups are related through a 45° rotation about the collinear c axis and a shift of the unit cell origin by $(0, \frac{1}{2}, 0)$. Thus, to describe the structural change between the β and β' phases, it is convenient to use the nonstandard space group description $C4_2$ of the β phase with $a = 10.46 \text{ \AA}$ and $c = 10.67 \text{ \AA}$ (and a shared unit cell origin), as it facilitates direct comparison of the two phases [18].

Here, we report on the structural evolution of $\text{Gd}_2(\text{MoO}_4)_3$ in the $Pba2$ phase by temperature-dependent x-ray diffraction (XRD) from ambient to above the ferroelectric phase transition. Going beyond previous studies of the thermal evolution of the lattice parameters [11,21], we investigate the temperature-driven displacement of the specific cations within the unit cell by applying Rietveld refinement of the diffraction data. Importantly, more than 780 Bragg reflections are considered, which enables a much more detailed structure analysis of the cation positions. The relative displacement of the cations in the improper ferroelectric and the paraelectric parent phase are obtained. The data reveal that the different cations follow different critical behavior, giving insight into the nature of the paraelectric-to-ferroelectric phase transition in $\text{Gd}_2(\text{MoO}_4)_3$.

II. METHOD

A. Synthesis

Single-phase powder of $\text{Gd}_2(\text{MoO}_4)_3$ was prepared via solid-state synthesis [22]. MoO_3 (99.97% trace metals basis, Sigma Aldrich) and Gd_2O_3 (99.9% trace metals basis, Sigma Aldrich) were dried for 5 h at 650 and 900°C , respectively. Stoichiometric amounts were then mixed in an agate mortar with ethanol and dried. Pellets were pressed at 80 MPa and sintered at 950°C for 25 h. The pellets were then crushed and finely ground in an agate mortar for XRD analysis.

B. Characterization

In situ temperature-dependent XRD experiments were performed using a Bruker AXS, D8 Advanced diffractometer with $\text{CuK}\alpha$ radiation ($\lambda = 0.154 \text{ nm}$) equipped with a VANTEC-1 position sensitive detector. The powder was dissolved in ethanol and deposited on a Pt strip acting as the sample holder, as well as the heating source, using an MRI Physikalische Geräte GmbH high-temperature controller. The paraelectric-to-ferroelectric phase transition in $\text{Gd}_2(\text{MoO}_4)_3$ was investigated over an extended temperature range from 25 to 145°C every 5°C , from 149 to 169°C every 2°C , and from 200 to 275°C every 25°C . Diffraction patterns were collected in the 2θ range $7\text{--}110^\circ$ with a step size of 0.016° and counting time of 1 s. A holding time of 5 min was used before each measurement which was performed at constant temperature. The temperature was calibrated against temperature-dependent XRD of a corundum standard powder

TABLE I. Restrictions on cations during Rietveld refinement.

Phase	Restriction
$Pba2$	$\text{Mo}3 : z = 0$
$P\bar{4}2_1m$	$\text{Mo}1, \text{Gd}1 : y = -x + (\frac{3}{2})$ $\text{Mo}3 : x = \frac{1}{2}, y = \frac{1}{2}, z = 0$

deposited on the same Pt strip, which gave an estimated temperature error $<5^\circ\text{C}$.

Rietveld refinement was performed with the fundamental parameter peak shape fitting using TOPAS (v5). The improper ferroelectric and paraelectric phases were refined using the $Pba2$ and $P\bar{4}2_1m$ space groups, respectively, with starting parameters taken from Jeitschko [18]. The diffractograms from 159°C and above were fitted using the $P\bar{4}2_1m$ space group. The refined parameters of the $P\bar{4}2_1m$ phase were transformed to $C4_2$ to facilitate direct comparison, as described above. The refinements were performed using a Chebyshev polynomial background of order seven and a preferred orientation factor for the (001) plane. In addition, the sample displacement, lattice parameters, and cation positions were refined, and the correlation matrix was calculated for every refinement (not shown). The cation positions were refined without restrictions, with the exceptions indicated in Table I. The oxygen positions were not refined and were fixed to the positions reported by Jeitschko [18].

III. RESULTS

A. Lattice parameter evolution

Representative diffraction patterns from four different temperatures are shown in Fig. 2. The Rietveld refinement (pink) is presented together with the measured intensity (blue) and the difference (gray). A detailed view of the 2θ range from 33.0 to 34.5° is presented in Fig. 1 in the Supplemental Material [23], demonstrating the transition from the tetragonal to the orthorhombic phase.

The refined lattice parameters of $\text{Gd}_2(\text{MoO}_4)_3$ are presented as a function of temperature in Fig. 3(a), and the volume evolution of the unit cell is shown in Fig. 3(b). Visible

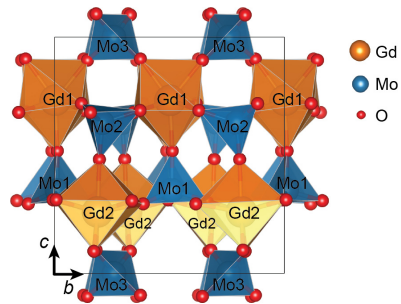


FIG. 1. Crystal structure of improper ferroelectric $\text{Gd}_2(\text{MoO}_4)_3$. The induced polarization is along the c axis.

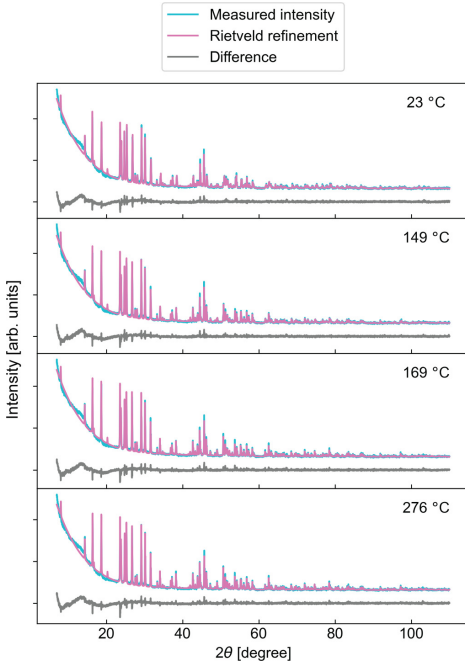


FIG. 2. Measured diffracted intensity and Rietveld refinement for four different temperatures. The difference between the experimental and refined data is shown in gray for all temperatures. The nonlinear increasing background at low 2θ is caused by the incident beam and the optics of the high-temperature setup.

in Fig. 3(a), at the paraelectric-to-ferroelectric phase transition, is the expansion of the c axis and contraction and splitting of the tetragonal a axis into the orthorhombic a and b axes below $T_c = 159^\circ\text{C}$, which is in excellent agreement with literature [11]. A discontinuous volume change at the transition is evident in Fig. 3(b), which reflects the first-order nature of the phase transition, demonstrating that the synthesized powder is of high quality, as it reproduces results previously shown for single crystals [11].

The linear (α_a , α_b , α_c) and volumetric (α_V) thermal expansion coefficients (TECs) are determined for the $Pba2$ and $C\bar{4}2_1$ phases, respectively, and the values are presented in Table II. To avoid nonlinear effects occurring near the phase

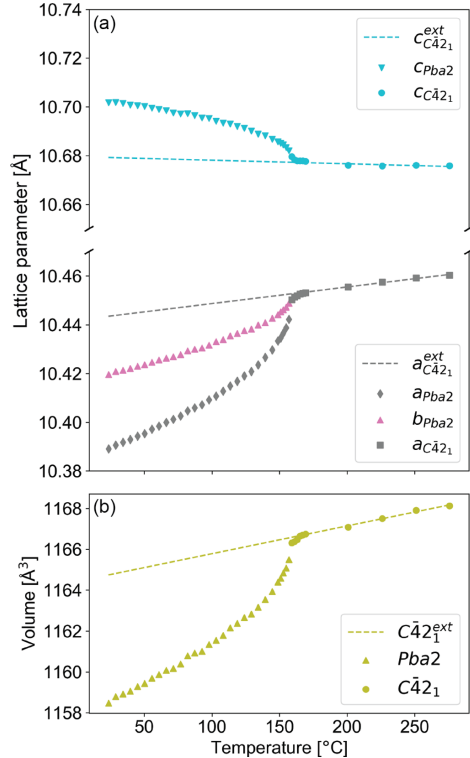


FIG. 3. (a) Lattice parameter and (b) unit cell volume evolution as a function of temperature for $\text{Gd}_2(\text{MoO}_4)_3$ in the $Pba2$ and $C\bar{4}2_1$ phases. The calculated errors for the lattice parameters are 0.0004, 0.0004, and 0.0002 Å or smaller for the a , b , and c parameters, respectively. The extrapolated a and c parameters and the volume of the $C\bar{4}2_1$ phase are presented as stippled lines.

transition, the TECs are calculated between 23 and 108 °C for the $Pba2$ phase and between 201 and 276 °C for the $C\bar{4}2_1$ phase.

B. Strain development

The temperature-dependent spontaneous strain $\epsilon_a(T)$ along the a axis developing in the ferroic phase is

TABLE II. Linear (α_a , α_b , α_c) and volumetric (α_V) expansion coefficients of the $Pba2$ and $C\bar{4}2_1$ phases, between 23–108 °C and 201–276 °C, respectively.

Phase	$\alpha_a [\times 10^{-5} \text{ }^\circ\text{C}^{-1}]$	$\alpha_b [\times 10^{-5} \text{ }^\circ\text{C}^{-1}]$	$\alpha_c [\times 10^{-5} \text{ }^\circ\text{C}^{-1}]$	$\alpha_V [\times 10^{-5} \text{ }^\circ\text{C}^{-1}]$
$Pba2$	2.68	1.61	−0.924	3.36
$C\bar{4}2_1$	0.611	—	−0.029	1.15

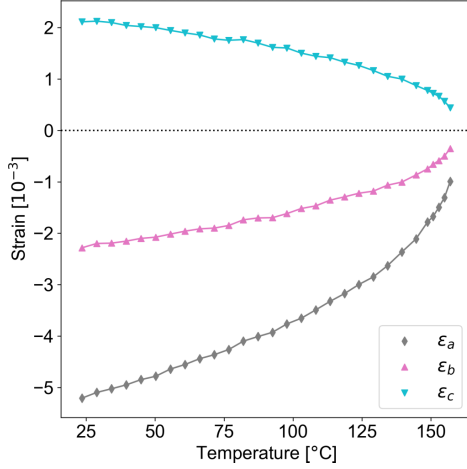


FIG. 4. Temperature evolution of the spontaneous strains along the a (ϵ_a), b (ϵ_b), and c axes (ϵ_c), respectively.

defined as [24]

$$\epsilon_a(T) = \frac{a_{Pba2}(T) - a_{C42_1}^{\text{ext}}(T)}{a_{C42_1}^{\text{ext}}(T)}, \quad (1)$$

where $a_{C42_1}^{\text{ext}}(T)$ is the extrapolated a lattice parameter of the tetragonal $C42_1$ phase, and $a_{Pba2}(T)$ is the a lattice parameter of the orthorhombic phase. The strain $\epsilon_b(T)$ along the b axis and $\epsilon_c(T)$ along the c axis are defined in an equivalent manner. The calculated strains $\epsilon_a(T)$, $\epsilon_b(T)$, and $\epsilon_c(T)$ are presented in Fig. 4. The strains $\epsilon_a(T)$ and $\epsilon_b(T)$ along the a and b axes are negative, indicating that the a and b axes are compressed in the ordered state, whereas $\epsilon_c(T)$ is positive, showing an expansion of the c axis in the $Pba2$ phase.

C. Relative displacement of atomic positions

The position of an atom in the basis of a unit cell is described by a vector $\vec{r} = (x\hat{a} + y\hat{b} + z\hat{c})$, where $0 < (x, y, z) \leq 1$ and \hat{a} , \hat{b} , and \hat{c} are unit vectors along the three crystallographic axes. The positions of the cations in the $Pba2$ phase with the largest displacement relative to the $C42_1$ phase are plotted as a function of temperature in Figs. 5(a) and 5(b). The correlation matrices from the Rietveld refinements demonstrate that none of the refined cation positions presented in Fig. 5 are significantly correlated (not shown). (A full description of all atom positions in the $Pba2$ and $C42_1$ phases at 23 and 201 °C is presented in the Supplemental Material [23]). The relative atomic displacements are defined as $\Delta\vec{r} = \vec{r} - \vec{r}'$, where \vec{r} is the position of the atom in the unit cell of the $C42_1$ phase, and \vec{r}' is the position of the atom in the $Pba2$ phase. The unit cell of $\text{Gd}_2(\text{MoO}_4)_3$ viewed along the a axis is illustrated in Fig. 5(c), showing the layered structure of the material. The cations which shift the most are located in layers 1 and 2,

TABLE III. Summary of the direction and the behavior of the cation displacements.

Layer	Cation	Direction	Behavior
1	Mo3	x	Nonlinear
1	Mo3	y	Linear
2	Gd2	x	Linear
2	Mo1	y	Nonlinear

which are shown projected along the c axis in Figs. 5(d) and 5(e), respectively.

Figures 5(a) and 5(b) reveal that the cation shifts follow one of two qualitatively different behaviors: The cations either shift linearly as T_c is approached, or the cation shifts display a discontinuity at the phase transition, following a nonlinear trend. The linear fits (full lines) are performed such that zero displacement is reached at T_c , and the stippled lines are fits made using an empirical formula based on a second-order Landau expression with $T_c = 432$ K. The goodness of fit (GOF) improves when using this empirical formula over a linear fit for the shift of Mo3 in the x direction and Mo1 in the y direction, indicating nonlinear behavior (the empirical Landau expression and calculated GOF values are presented in the Supplemental Material [23]). Interestingly, Mo3, which sits in layer 1 [Figs. 5(a) and 5(d)], follows a linear trend in the y direction and a nonlinear trend in the x direction. In layer 2, Gd2 shifts linearly in the x direction, whereas Mo1 follows nonlinear behavior in the y direction.

IV. DISCUSSION

A. Lattice parameters and strains

The discontinuity of the volume evolution at 159 °C (Fig. 3) observed in our powder samples demonstrates the first-order nature of the paraelectric-to-ferroelectric phase transition, consistent with the previous work on $\text{Gd}_2(\text{MoO}_4)_3$ single crystals by Kobayashi *et al.* [11]. We find that, at the level of the individual cations, this first-order phase transition manifests as a steplike change in the displacement of Mo3 in the x direction and Mo1 in the y direction [Table III, Figs. 5(a) and 5(b)].

Our calculations show that, qualitatively, the lattice strain evolution (ϵ_a , ϵ_b , and ϵ_c) in $\text{Gd}_2(\text{MoO}_4)_3$ single-phase powder (Fig. 4) and single crystals [11] exhibit similar behavior. Checking the values for all the strains at 50 and 150 °C gives a maximum deviation of $\sim 25\%$ for ϵ_c and a maximum deviation of $\sim 15\%$ for ϵ_a and ϵ_b between the data obtained on single-phase powder and single crystals. It is important to note, however, that our powder results are gained from Rietveld refinement, i.e., the whole diffractogram is considered in the determination of the lattice parameters and the calculated strain, whereas only specific diffraction peaks were considered to determine the lattice parameters from single crystals in the study by Kobayashi *et al.* [11].

B. Cation displacements

Rietveld refinement is utilized to study the displacement of cations from their positions in the high-temperature $C42_1$

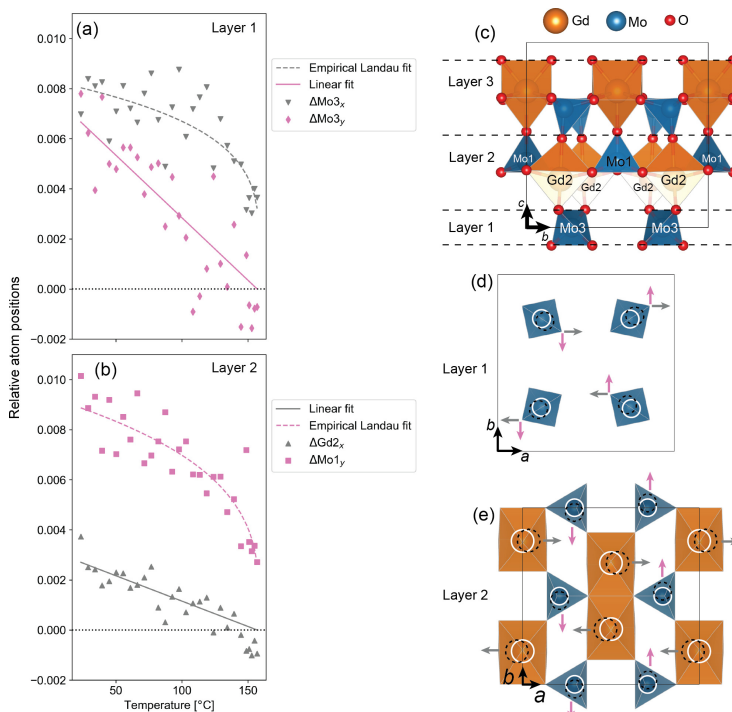


FIG. 5. Temperature evolution of the relative displacement of Mo1, Mo3, and Gd2 in the *Pba2* phase. (a) and (b) Relative atom positions as a function of temperature, determined from Rietveld refinement. (c)–(e) $C\bar{4}2_1$ phase of $Gd_2(MoO_4)_3$ (with atom designation referring to the *Pba2* phase). (c) $Gd_2(MoO_4)_3$ viewed as a three-layered structure when projected along the *a* axis, and (d) layer 1 and (e) layer 2 viewed along the *c* axis. The direction of the movement of the cation positions from the $C\bar{4}2_1$ phase to *Pba2* is indicated with white rings as the starting positions, and black dashed rings and arrows indicate the direction of the cation displacement. (The relative movement is exaggerated in the illustration to make the displacement clearer). The relative displacement of oxygen anions accompanying the displacement of cations is not shown for simplicity.

phase relative to their positions in the improper ferroelectric *Pba2* phase as a function of temperature (Fig. 5). Including the refinement of the oxygen positions (i.e., an additional 36 free parameters) does not significantly improve the result of the refinement, and it also leads to some correlations of ~ 100 for a few parameters. Thus, the oxygen atom positions are not refined in this paper and are fixed to the positions reported by Jeitschko [18].

1. Layer 1

In layer 1 in the $C\bar{4}2_1$ phase, the Mo3 tetrahedra are regular tetrahedra, meaning that all the distances between Mo3 and O atoms are the same ($Mo3-O9 = 1.7319 \text{ \AA}$). As the material is cooled down, the Mo3 shifts within the *xy* plane of the *Pba2* phase, shifting linearly with temperature in the *y* direction and nonlinearly along the *x* direction. This displacement leads to two tetrahedra positioned closer to the center of the unit

cell and two tetrahedra shifted toward the corners of the unit cell, as illustrated in Fig. 5(d). The Mo3 remains at $z = 0$ before and after the transition. At room temperature, the tetrahedra are no longer regular but distorted, with a 1.1% difference between the longest and shortest Mo-O distances, i.e., the Mo3 tetrahedra in layer 1 are shifted and slightly distorted upon transitioning into the improper ferroelectric phase.

Comparing the different magnitudes of the strains with the displacement of the Mo3, we see that the strain is largest along the *a* axis of the unit cell, i.e., along the same axis as the nonlinear displacement of the Mo3. At room temperature, however, the total magnitude of the relative shift of the Mo3 cation is ~ 0.008 in both directions. The special orientation of the Mo3 tetrahedra in layer 1 is such that an edge faces upward along the $+z$ direction (and likewise, an edge also faces downward along $-z$).

2. Layer 2

Layer 2 consists of both Mo1 tetrahedra and Gd2 polyhedra, where each Gd atom is bonded to seven oxygen atoms. For both Mo1 and Gd2, the shift along z is minimal after the phase transition. As demonstrated in Fig. 5(b), the major shifts of cations in this layer occur for Mo1 along the y axis and Gd2 along the x axis. Noteworthy for the polyhedra and tetrahedra in this layer is that they all have an apex pointing along the $+z$ direction. Furthermore, the tetrahedra are all corner sharing with the Gd2 polyhedra within layer 2 and share their apex oxygen with the apex oxygen, which points along the $-z$ direction of the Gd1 polyhedra of layer 3. The Gd2 polyhedra in layer 2 are corner sharing with Mo tetrahedra in all the layers, and in addition, two and two Gd2 polyhedra are edge sharing within layer 2.

At the phase transition, the Mo1 shows a steplike displacement along the y axis and follows a nonlinear displacement toward room temperature. The shift of the Mo1 cation leads to a rotation of the Mo1 tetrahedra. The tetrahedra at $y \sim 0$ rotate clockwise, and the tetrahedra at $y \sim 0.5$ rotate counterclockwise. In the $C4_21$ phase, the average distance Mo-O = 1.7495 Å, with a 3.6% deviation between the longest and shortest distance. In the *Pba2* phase, the average distance is 1.7597 Å, with a 4.2% difference between the longest and shortest bond length. The total shift of the relative position from the $C4_21$ phase to room temperature is ~ 0.009 , which is like the Mo3 relative shift in layer 1. The displacement of Gd2 is smaller than the other relative cation displacements reported here. However, it has a clear linear trend with temperature away from the high-temperature position. The average Gd-O distance in the $C4_21$ phase is 2.3535 Å, with a 5.6% difference between the shortest and longest distance. At room temperature, the average distance is 2.3550 Å, with a 10.1% difference. This clearly demonstrates that the Gd polyhedra in general are more distorted, and that they are more distorted by the phase transition than the Mo tetrahedra. This can be explained by the fact that the MoO_4^{2-} tetrahedra are much more rigid structures than the seven coordinated Gd polyhedra. The rigidity is proposed to be due to the more covalent character of the Mo-O bond relative to the Gd-O bond.

The cation displacement in layer 2 can be said to be opposite of the displacement in layer 1, meaning that the discontinuous (and largest) cation displacement in layer 2 happens along the y direction as compared with layer 1, where the discontinuous displacement happens along the x direction. In addition, this is opposite to the strain behavior, which is largest along the a axis.

3. Layer 3

The displacement of the cations in layer 3 due to the phase transitions is very small and, hence, their deviation from the high-temperature phase is not discussed in further detail. However, as the cations in layer 2 shift, so do the oxygen atoms which are connected to the cations in layers 1 and 3.

The latter leads to a rotation of the Mo tetrahedra in layer 3, such that the tetrahedra at $x \sim 0$ rotate counterclockwise, and the Mo tetrahedra at $x \sim 0.5$ rotate clockwise. The Gd polyhedra in layer 3 are also slightly more distorted in the *Pba2* phase than the $C4_21$ phase.

V. CONCLUSIONS

The phase transition of single-phase $Gd_2(MoO_4)_3$ synthesized via the solid-state method was studied by nonambient XRD. Lattice parameters, volume, and strain evolution were determined as a function of temperature. A discontinuous volume evolution at the phase transition was observed, reflecting a first-order phase transition, consistent with previous investigations performed on $Gd_2(MoO_4)_3$ single crystals [11,24]. Furthermore, a similar strain evolution was demonstrated. Rietveld refinement was performed to shed light on the evolution of the atomic displacements that occur at the improper ferroelectric phase transition by studying the individual cation displacements from the high-temperature positions. The Mo3 atoms in layer 1 were found to shift along the x and y directions. Further, they follow the same trend as the macroscopic strain, in the sense that the initial discontinuous and the largest shift occurred in the same direction as the largest strain. At room temperature, however, the total displacement was about equal in both the x and y directions. In layer 2, Mo1 was demonstrated to shift the most and nonlinearly along the y direction. Gd2, in layer 2, showed a clear linear displacement with temperature along the x direction, even though the total displacement was smaller than for the other cations. Thus, the cation movement in layer 2 can be said to have an opposite trend to the cation movement in layer 1 and the spontaneous strain. In this paper, we demonstrate that individual cations in $Gd_2(MoO_4)_3$ follow two qualitatively different behaviors upon transitioning into the improper ferroelectric phase. This insight may lead to a better understanding of the emergence of the polarization in $Gd_2(MoO_4)_3$ and improper ferroelectric materials in general.

The data that support the findings in this paper are available from the corresponding author upon reasonable request.

ACKNOWLEDGMENTS

Frida Paulsen Danmo is acknowledged for helping with the solid-state synthesis and Ola G. Grendal for fruitful discussions regarding Rietveld refinement. The Research Council of Norway is acknowledged for financial support through the Projects FASTS (No. 250403/F20) and BORNIT (No. 275139/F20).

T.G. and D.M. initiated the project. I.-E.N. and M.T. performed the XRD experiment and analysis with supervision from T.G. I.-E.N. synthesized the powder. I.-E.N. wrote the paper under supervision of T.G. and D.M., with contributions from all the authors.

[1] E. T. Keve, S. C. Abrahams, and J. L. Bernstein, Ferroelectric ferroelastic paramagnetic beta- $Gd_2(MoO_4)_3$ crystal structure of

the transition-metal molybdates and tungstates. VI, *J. Chem. Phys.* **54**, 3185 (1971).

- [2] T. Kimura, T. Goto, H. Shintani, K. Ishizaka, T. Arima, and Y. Tokura, Magnetic control of ferroelectric polarization, *Nature (London)* **426**, 55 (2003).
- [3] M. Matsubara, S. Manz, M. Mochizuki, T. Kubacka, A. Iyama, N. Aliouane, T. Kimura, S. L. Johnson, D. Meier, and M. Fiebig, Magnetolectric domain control in multiferroic TbMnO₃, *Science* **348**, 1112 (2015).
- [4] D. Meier, M. Maringer, T. Lottermoser, P. Becker, L. Bohatý, and M. Fiebig, Observation and Coupling of Domains in a Spin-Spiral Multiferroic, *Phys. Rev. Lett.* **102**, 107202 (2009).
- [5] N. Leo, A. Bergman, A. Cano, N. Poudel, B. Lorenz, M. Fiebig, and D. Meier, Polarization control at spin-driven ferroelectric domain walls, *Nat. Commun.* **6**, 6661 (2015).
- [6] T. Choi, Y. Horibe, H. T. Yi, Y. J. Choi, W. Wu, and S.-W. Cheong, Insulating interlocked ferroelectric and structural antiphase domain walls in multiferroic YMnO₃, *Nat. Mater.* **9**, 253 (2010).
- [7] T. Jungk, Á. Hoffmann, M. Fiebig, and E. Soergel, Electrostatic topology of ferroelectric domains in YMnO₃, *Appl. Phys. Lett.* **97**, 12904 (2010).
- [8] S. E. Cummins, Electrical, optical, and mechanical behavior of ferroelectric Gd₂(MoO₄)₃, *Ferroelectrics* **1**, 11 (1970).
- [9] J. D. Axe, B. Dorner, and G. Shirane, Mechanism of the Ferroelectric Phase Transformation in Rare-Earth Molybdates, *Phys. Rev. Lett.* **26**, 519 (1971).
- [10] A. Fousková, The specific heat of Gd₂(MoO₄)₃, *J. Phys. Soc. Jpn.* **27**, 1699 (1969).
- [11] J. Kobayashi, Y. Sato, and T. Nakamura, X-ray study on thermal expansion of ferroelectric Gd₂(MoO₄)₃, *Phys. Status Solidi* **14**, 259 (1972).
- [12] M. Fiebig, T. Lottermoser, D. Meier, and M. Trassin, The evolution of multiferroics, *Nat. Rev. Mater.* **1**, 16046 (2016).
- [13] J. R. Barkley and W. Jeitschko, Antiphase boundaries and their interactions with domain walls in ferroelastic-ferroelectric Gd₂(MoO₄)₃, *J. Appl. Phys.* **44**, 938 (1973).
- [14] A. W. Smith and G. Burns, Optical properties and switching in Gd₂(MoO₄)₃, *Phys. Lett. A* **28**, 501 (1969).
- [15] A. Kumada, Optical properties of gadolinium molybdate and their device applications, *Ferroelectrics* **3**, 115 (1972).
- [16] L. H. Brixner, P. E. Bierstedt, A. W. Sleight, and M. S. Licit, Precision parameters of some Ln₂(MoO₄)₃-type rare earth molybdates, *Mater. Res. Bull.* **6**, 545 (1971).
- [17] M. E. Lines and A. M. Glass, *Principles and Applications of Ferroelectrics and Related Materials* (Oxford University Press, Oxford, 1977).
- [18] W. Jeitschko, A comprehensive x-ray study of the ferroelectric-ferroelastic and paraelectric-paraelastic phases of Gd₂(MoO₄)₃, *Acta Cryst. B* **28**, 60 (1972).
- [19] K. Aizu, A. Kumada, H. Yumoto, and S. Ashida, Simultaneous ferroelectricity and ferroelasticity of Gd₂(MoO₄)₃, *J. Phys. Soc. Jpn.* **27**, 511 (1969).
- [20] H. J. Borchardt and P. E. Bierstedt, Gd₂(MoO₄)₃: A ferroelectric laser host, *Appl. Phys. Lett.* **8**, 50 (1966).
- [21] R. E. Newnham, H. A. McKinstry, C. W. Gregg, and W. R. Stitt, Lattice parameters of ferroelectric rare earth molybdates, *Phys. Status Solidi* **32**, K49 (1969).
- [22] M. C. G. Afonso, Preparation and characterization of rare earth molybdates: Structure-property relation, Ph.D. thesis, Universidad de La Laguna, 2015.
- [23] See Supplemental Material at <http://link.aps.org/supplemental/10.1103/PhysRevMaterials.6.034402> for details on the temperature calibration and the results of the Rietveld refinement of the structure at 23 and 201 °C. Additionally, the evolution from the tetragonal to the orthorhombic structure is shown, and a brief discussion of the GOF for the different fits presented in Fig. 5 is given.
- [24] E. K. Salje, *Phase Transitions in Ferroelastic and Co-Elastic Crystals* (Cambridge University Press, Cambridge, 1991).

Supplementary material: Observation of cation-specific critical behavior at the improper ferroelectric phase transition in $\text{Gd}_2(\text{MoO}_4)_3$

Inger-Emma Nylund, Maria Tsoutsouva, Tor Grande, Dennis Meier^a

Department of Materials Science and Engineering, NTNU Norwegian University of Science and Technology, NO-7491 Trondheim, Norway

Results from Rietveld refinement

Details on how the Rietveld refinement was performed is given in the main text. Figure 1 shows detailed diffraction patterns acquired at 23, 149, 169 and 276 °C, which demonstrate how the 220 peak of the tetragonal phase transforms to the 040 and 400 peak of the orthorhombic phase across the phase transition. Table I and Table II show the refined cation positions (Gd and Mo), and oxygen positions reported by Jeitschko [1] in the $Pba2$ and $C\bar{4}2_1$ phase, at 23 and 201 °C, respectively. Below is a short note on the transformation from the non-standard space group $C\bar{4}2_1$ to the standard space group $P\bar{4}2_1m$, used in the Rietveld refinement.

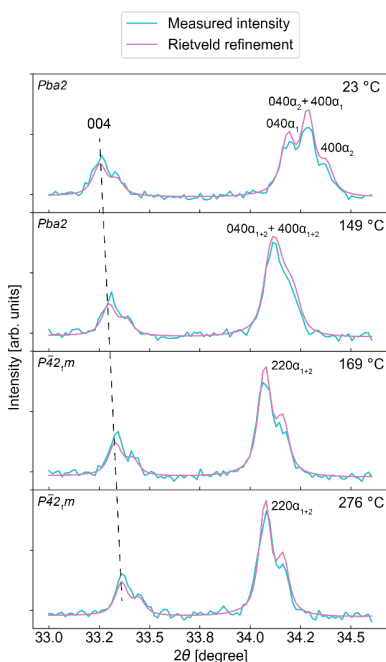


Figure 1. Detail from the Rietveld refinement at 23, 149, 169, and 276 °C. The transition from the orthorhombic $Pba2$ to the tetragonal $P\bar{4}2_1m$ is shown through the transition from two peaks (040 and 400) in the orthorhombic phase which transform to one peak (220) in the tetragonal phase.

^a Author to whom correspondence should be addressed: dennis.meier@ntnu.no

*Pba*2

$a = 10.3891 \text{ \AA}$

$b = 10.4196 \text{ \AA}$

$c = 10.7018 \text{ \AA}$

Table I. Atom positions in the *Pba*2 phase at 23 °C.

Atom	x	y	z
Gd(1)	0.1873	0.4975	0.7330
Gd(2)	0.4963	0.3131	0.2600
Mo(1)	0.2063	0.4899	0.3517
Mo(2)	0.0029	0.2070	0.6380
Mo(3)	0.2430	0.2422	0.0
O(1)	0.1921	0.4882	0.5186
O(2)	0.4801	0.3053	0.4825
O(3)	0.1287	0.0069	0.3112
O(4)	0.4940	0.1280	0.6899
O(5)	0.1579	0.1557	0.6815
O(6)	0.1571	0.3360	0.3074
O(7)	0.3840	0.3837	0.7191
O(8)	0.3848	0.1145	0.2941
O(9)	0.1255	0.1708	0.0937
O(10)	0.3174	0.1264	0.9074
O(11)	0.3545	0.3197	0.0984
O(12)	0.1704	0.3571	0.9024

$C\bar{4}2_1$

$a = 10.4555 \text{ \AA}$

$c = 10.6761 \text{ \AA}$

Table II. Atom positions in the non-standard $C\bar{4}2_1$ phase at 201 °C.

Atom	x	y	z
Gd(1)	0.1868	0.5	0.7368
Mo(1)	0.2065	0.5	0.3563
Mo(3)	0.25	0.25	0.0
O(1)	0.1952	0.5	0.5195
O(3)	0.1289	0.0	0.3109
O(5)	0.1389	0.1372	0.7005
O(9)	0.1377	0.1770	0.0955

Transformation from $C\bar{4}2_1$ to $P\bar{4}2_1m$

The notation for describing the GMO crystal structure used here is adopted from Jeitschko [1], both in terms of cation nomenclature and utilizing the non-standard space group $C\bar{4}2_1$ to describe the high-temperature phase, to facilitate direct comparison between the two phases.

Given that all the atom positions in the $C\bar{4}2_1$ phase is described by $r = x + y + z$, where $0 \leq x, y, z < 1$. Then, in the $P4_21m$ phase, the atom positions can be described by $r' = x' + y' + z'$, $0 \leq x', y', z' < 1$, where:

$$\begin{aligned}x' &= x + y, \\y' &= -x + y, \\z' &= z,\end{aligned}$$

and the unit cell center must be additionally shifted by $[0, \frac{1}{2}, 0]$.

Empirical Landau expression and GOF values for relative atom positions

The relative atom positions which follow a non-linear trend ($Mo3_x$ and $Mo1_y$) were fitted to the function given in Equation 1:

$$r = k \left| \frac{T - 432}{432} \right|^\beta. \quad (1)$$

r is the relative atom position, k is a constant scaling factor, T is the temperature, $T_c = 432$ K, and β is the critical exponent.

The GOF is given as:

$$GOF = \chi^2 = \sum_{i=1}^k \frac{(o_i - e_i)^2}{e_i}$$

o_i = observations

e_i = expected values, i.e., the fitted value

The two types of fits presented in the main text are constrained linear fits (forced through 0 at T_c) for $Mo3_y$ and $Gd2_x$, and a fit to the empirical Landau function (Eq. 1) for $Mo3_x$ and $Mo1_y$. The GOF of these presented fits were calculated (GOF1). In addition, the GOF values for a linear fit, with no constraints, for all the presented relative atom positions were calculated (GOF2). The GOF values are shown in Table III, and they demonstrate that the empirical Landau function describes the non-linear critical behavior better than a linear fit since GOF1 is lower than GOF2 for these atom positions.

Table III. GOF values for fits to the presented relative atom positions.

Cation position ("behavior")	GOF1 presented data	GOF2 linear fit	GOF1/observed maximum value	GOF2/observed maximum value
Mo3x ("Landau")	0.0047	0.0069	0.59	0.86
Mo3y ("Linear")	0.0561	0.1079	7.01	13.49
Gd2x ("Linear")	0.0371	-0.0041	12.36	-1.36
Mo1y ("Landau")	0.0046	0.0054	0.46	0.54

References

- [1] W. Jeitschko, *A Comprehensive X-Ray Study of the Ferroelectric-Ferroelastic and Paraelectric-Paraelastic Phases of Gd₂(MoO₄)₃*, Acta Crystallogr. Sect. B Struct. Crystallogr. Cryst. Chem. **28**, 60 (1972).

